Technische Universiteit Delft

Lubricated friction on pipeline pigs

Thesis

Bas van Zelderen

Lubricated friction on pipeline pigs

Thesis

by

Bas van Zelderen

to obtain the degree of Master of Science
at the Delft University of Technology,
to be defended publicly on Tuesday Februari 23, 2021 at 13:30 PM.

Student number:	4497708	
Thesis committee:	Dr. ir. B.W. van Oudheusden,	TU Delft, supervisor
	Prof. Dr. Ir. R.A.W.M. Henkes,	Shell, TU Delft, external examinator
	Dr. Ir. A.H. van Zuijlen,	TU Delft
	Dr. Ir. M.H.W. Hendrix,	Shell

An electronic version of this thesis is available at `http://repository.tudelft.nl/`.

Abstract

Pigs are devices that are transported from time to time through a pipeline, mainly to either clean the pipeline or to inspect the integrity of the pipeline wall. Conventional models for the friction between the pig and the pipe wall, as used in the oil and gas industry, are often criticized for their inaccuracies. To obtain a more accurate model, this thesis investigates the detailed physics behind the frictional forces.

The effect of the sliding conditions on the wall-normal force and on the friction force was investigated by conducting 1D lubricated sliding experiments for a rubber lip moving along a metal surface and by performing model simulations, including a parameter sensitivity study. The experiments were conducted for dry water, dodecane and castor oil under varying sliding velocities and loads. The loads were measured with a dual axis transducer and the lubrication film was observed during the experiments with a microscope set-up.

The experimental results consist of friction forces for various configurations, which show that the frictional behaviour depends strongly on the lubrication regime in which the rubber lip is operating. The friction coefficients for the boundary lubrication regime and the mixed lubrication regime were measured and compared with results from the model.

Among the tested fluids, castor oil showed a non-proportional decrease in friction force when the sliding velocity was increased. This decrease in friction force was interpreted as a transition from the boundary lubrication regime to the mixed lubrication regime. The other tested fluids remained in the boundary lubrication regime in the experimental runs. A validation study was performed by fitting the friction model to the experimental results. Only the dry friction coefficients are in good agreement with the model. Both the water and dodecane experiments show a slight increase for the friction coefficient with increasing lubrication factor and are in mediocre agreement with the friction model. The castor oil experiments are in the mixed lubrication regime of the Stribeck curve and are in reasonable agreement with the model. The results can be linked to the oil and gas industry as pigs can operate in different regimes of the Stribeck curve. Stalled pigs can be the result of transitions from the mixed lubrication regime to the boundary lubrication regime. This can happen when a pig is momentarily slowed down in the pipeline.

Recommendations for future experimental work are: performing experiments at higher sliding velocities, using an emulsion as lubricant and finding suitable methods to calibrate models that have a range of input parameters.

This work was carried out by the author at the Shell Technology Centre in Amsterdam. The supervision by the Shell staff and the support obtained in carrying out the experiments in the Shell lab are greatly acknowledged.

Preface

I would like to thank my supervisors Ruud Henkes and Bas van Oudheusden for giving me the opportunity to do my master thesis at the Shell Technology Centre Amsterdam. During the progress meetings they provided me with useful advice and guidance on conducting research and writing the report.

I would also like to thank Maurice Fransen, who was definitely the most friendly daily supervisor at STCA. He would always make time to help me get back on track when I faced setbacks or lost my motivation. Ruud and Maurice were both very supportive mentors in general.

Simultaneously during my time at STCA, my friend and fellow intern Cor Lerink also did his thesis there. When we faced the same challenges in our research and felt defeated, we would take a break and cheer each other up. These times were much appreciated and it made my work a little bit easier sometimes.

The support by Shell is greatly acknowledged. Thanks are due to Peter Veenstra, the flow assurance team, Harry Gussekloo and particularly Jochem Boer who provided me with practical advice and technical knowledge.

I would like to thank my family and friends for their continuous support. Most of all I would like to thank my girlfriend, Stefanie Captein, who has been incredibly supportive throughout this project.

Bas van Zelderen
Haarlem, February 2021

Contents

List of Figures ix

Nomenclature xiii

1 Introduction 1
1.1 Background . . . 2
1.2 Bypass pigging . . . 4
1.3 Literature review . . . 5
1.4 Research questions . . . 7
1.5 Outline . . . 7

2 Friction models 9
2.1 Frictional behaviour of bypass pigs . . . 10
2.1.1 Dry friction . . . 10
2.1.2 Lubricated friction . . . 11
2.2 Hydrodynamic lubrication . . . 12
2.2.1 Navier-Stokes equations . . . 12
2.2.2 Scaling laws . . . 14
2.2.3 Reynolds equation . . . 16
2.3 Mixed and boundary lubrication . . . 21
2.3.1 Contact mechanics . . . 21
2.3.2 The Greenwood-Williamson roughness model . . . 23
2.3.3 Shared load principle . . . 24
2.3.4 Moes film thickness . . . 24
2.3.5 Solution procedure . . . 25
2.3.6 Model results . . . 26
2.4 Wear . . . 30
2.5 Wall force modelling . . . 32
2.5.1 Mooney-Rivlin model . . . 32
2.5.2 Model results . . . 33

3 Experiments 37
3.1 Approach . . . 38
3.1.1 Experimental scaling . . . 38
3.1.2 Pigging conditions . . . 38
3.1.3 Experimental conditions . . . 39
3.1.4 From sealing disc to rubber lip . . . 39
3.2 Pig tribometer facility . . . 40
3.2.1 Experimental execution . . . 42
3.3 Experimental data . . . 44

4 Results 45
4.1 Experimental results . . . 46
4.1.1 General observations . . . 46
4.1.2 Friction and wall-normal force . . . 46
4.1.3 Friction coefficient vs thickness . . . 48
4.1.4 Model validation . . . 50
4.1.5 Link with pigging operations . . . 50
4.2 Visual observations . . . 51

5 Discussion **55**

6 Conclusions **57**

7 Recommendations **59**

Bibliography **61**

A Modelled rubber lip **63**

B Components in the experimental set-up **65**
B.1 Force measurement 65
B.1.1 Strain gauges 65
B.1.2 Elastic element 66
B.2 Optical system 69
B.2.1 The sensor 70
B.2.2 Objectives 71

C Additional results from the pig Tribometer **75**
C.1 Friction force 75
C.2 Wall force 76
C.3 Friction coefficient 78

List of Figures

1.1 Schematic of a bypass pig. 2
1.2 Four common pigs: cup pig, bidi pig, spherical pig and foam pig 3
1.3 Pig launcher illustrations. 3
1.4 The favorable features of bypass pigging. 4
1.5 Comparison in solids handling of a normal pig and a bypass pig. 5
1.6 Pig friction models. 5
1.7 Fundamental principles in recent pig friction literature. 6

2.1 The Stribeck curve provides the friction coefficient as a function of the lubrication coefficient and distinguishes several regimes. 11
2.2 Control volume of a thin fluid film. 13
2.3 Hydrodynamic lubrication between an inclined seal and a moving surface. 17
2.4 Pressure distribution underneath a rigid seal for various inclination ratios with water as lubricant. L = 500 N, U = 1 m/s. 19
2.5 Dimensionless load acting on a rigid seal as function of slope with water as lubricant. . 20
2.6 friction coefficient of a rigid seal for various inclination ratios with water as lubricant. L = 500 N, U = 1 m/s 21
2.7 Hydrodynamic lubrication between an inclined seal and a moving surface. 22
2.8 The Greenwood and Williamson Contact Model for the contact between a smooth rigid plane and rough elastic surface 23
2.9 Flow diagram of the solution procedure. 26
2.10 Stribeck curves with varying normal force F_n (5, 10 and 20 N). 27
2.11 Stribeck curves with varying the friction coefficient in the boundary lubrication regime μ_0. 28
2.12 Stribeck curves with varying statistical roughness parameters β and n. 29
2.13 Stribeck curves with varying statistical roughness parameters σ_s and n. 30
2.14 Worn sealing and guiding discs of a pig. 31
2.15 Two stress-strain curves measured by universal testing machines. 32
2.16 Experimentally obtained stress-strain data fitted with the two-parameter Mooney-Rivlin model and linear strain theory. 33
2.17 Mesh plot of the sealing disc confinement model for 2% oversize. 33
2.18 Stretch of a sealing disc during confinement in a pipeline. 34
2.19 Strain and wall force during the confinement of a modelled sealing disc into a pipeline with 1% oversize. 35
2.20 Peak values for the strain and wall force during sealing disc confinement as function of the oversize. 35
2.21 Final stable values for the strain and wall force during sealing disc confinement as function of the oversize. 36

3.1 Simplifying step from a sealing disc to a rubber lip. 40
3.2 Close-up of the force measurement system of the pig tribometer and the sliding motion of the translation table. 41
3.3 Close-up of glass resevoir used to inhibit the lubricants. 42
3.4 Close-up of the full pig tribometer experimental setup. 42
3.5 Dry friction during a run with a 6mm thick lip for velocities between 10 and 80 mm/s. . 44
3.6 Snapshot of an experiment with castor oil and red dye as lubricant. 44

4.1 Comparison of friction force for dry, water, dodecane and castor oil with an 8 mm thick lip at 60 mm/s. 46

4.2 Comparison of wall-normal force for dry, water, dodecane and castor oil with an 8 mm thick lip at 60 mm/s. 46
4.3 Standard deviation of the dodecane friction force trajectory as function of sliding velocity for different thicknesses. 47
4.4 Error bar of the dry friction coefficients as function of the sliding velocity for different thicknesses of the rubber contact. 48
4.5 Error bar of the friction coefficients of water as function of the sliding velocity for different thicknesses of the rubber contact. 48
4.6 Error bar of the friction coefficients of dodecane as function of the sliding velocity for different thicknesses of the rubber contact. 49
4.7 Error bar of the friction coefficients of castor oil as function of the sliding velocity for different thicknesses of the rubber contact. 49
4.8 Stribeck curve fitted with the friction experiments for the investigated fluids with a rubber contact thickness of 6 mm. 50
4.9 Rubber contact during the experimental run with castor oil at a sliding distance of 0 mm. 51
4.10 Rubber contact during the experimental run with castor oil at a sliding distance of 35 mm, showing the first vortex development just in front of the rubber. 52
4.11 Rubber contact during the experimental run with castor oil at a sliding distance of 51 mm. 52
4.12 Rubber contact during the experimental run with castor oil at a sliding distance of 69 mm. 52
4.13 Rubber contact during the experimental run with castor oil at a sliding distance of 98 mm. 53
4.14 Rubber contact during the experimental run with castor oil after the sliding motion has stopped. 53

A.1 Deformation of a clamped rubber lip with a wall and friction force imposed on it. 63
A.2 2D Deformation of a clamped rubber lip sliding across a steel surface. 64

B.1 The elongation of conductive wires in a strain gauge lead to an increase in the electrical resistance. 65
B.2 The general Wheatstone bridge increases the sensitivity of the difference in resistance on any of the four arms. 66
B.3 In a full Wheatstone bridge configurations strains are measured by unbalancing the bridge with opposing pairs. 66
B.4 Several designs of elastic elements for producing force transducers 67
B.5 Parallel leaf spring flexure in a deflected state 68
B.6 Flexure construction that decouples movement in the x,y and z direction. 68
B.7 The transducer designed to measure the wall and friction force of the lubricated rubber sample. 69
B.8 Optical pathways of a camera system. 70
B.9 A pixel depicted as a well with several important properties that define its sensitivity. . 71
B.10 Comparison between an image shot with sensors that have a relatively low and high dynamic range. 71
B.11 A lens with a low numerical aperture could lead to an unresolved image due to wide Airy discs, while a lens with a high numerical aperture can resolve more details due to thin Airy discs. 72
B.12 The optical set-up will use an infinity corrected microscope system to frame the lubrication layer between the rubber sample and the glass plate. 73

C.1 Castor oil. 75
C.2 Castor oil. 75
C.3 Castor oil. 76
C.4 Castor oil. 76
C.5 Castor oil. 76
C.6 Castor oil. 77
C.7 Castor oil. 77
C.8 Castor oil. 77
C.9 Comparison of the friction coefficient trajectory as function of sliding distance for dry friction with a 6mm thick rubber lip. 78

C.10 Castor oil. 78
C.11 Castor oil. 79

Nomenclature

Roman Symbols	**Dimension**	**Description**
a	[m^2]	Asperity contact surface.
A_r	[-]	Total area of asperity contact.
C_1	[MPa]	First Mooney-Rivlin parameter.
C_2	[MPa]	Second Mooney-Rivlin parameter.
C_i	[-]	Integration constant.
C_w	[mm]	Chamfer width.
d	[m]	Distance between the average height of asperities on both surfaces.
D_o	[m]	Outer diameter of sealing disc.
D_i	[m]	Inner diameter of sealing disc.
E	[Pa]	Elasticity modulus.
E'	[Pa]	Reduced elasticity modulus.
h	[m]	Fluid film height.
h_m	[m]	Fluid film height by the Moes formulation.
h_j	[m]	Fluid film height by the Johnson correction.
$\tilde{h}$	[-]	Dimensionless fluid film height.
$\boldsymbol{f}$	[N]	External forces.
F	[N]	Force resultant.
F_{a}	[N]	Asperity contact force.
F_{fric}	[N]	Friction force.
F_{n}	[N]	Force normal to the surface.
F_{p}	[N]	Force exerted on the sealing discs by a pressure difference.
F_{wall}	[N]	Wall force, normal to the pipeline wall.
g	[m/s^2]	Gravitational acceleration.
h	[m]	Fluid film thickness.
h_{w}	[m]	Local wear depth.
H	[Pa]	Material hardness.
I_r	[-]	Index of optical refraction.
k	[-]	Wear coefficient.
K	[-]	Probability that debris will form.
l_0	[m]	Undeformed length.
l'	[m]	Deformed length.
L	[N/m]	Load along the y-axis.
$\tilde{L}$	[-]	Dimensionless load.
M_{w}	[Nm]	Moment induced by the wall force.
M_{f}	[Nm]	Moment induced by the friction force.
$M_{\Delta\mathrm{P}}$	[Nm]	Moment induced by the differential pressure.
n	[-]	Number of asperities that make contact.
N	[-]	Total number of asperities.
OS	[%]	Sealing disc oversize.
p	[Pa]	Pressure.
$\tilde{p}$	[-]	Dimensionless pressure (used in the momentum equation).
P_a	[Pa]	Asperity pressure.
P_f	[Pa]	Fluid pressure.
P_t	[Pa]	Total pressure.
P_0	[Pa]	Characteristic pressure.
$\mathcal{P}$	[-]	Probability of contact between asperities
Δp	[Pa]	Pressure difference.

q_x	[m^2/s]	Volumetric flowrate in the x-direction per meter with.
$\tilde{q}_x$	[-]	Dimensionless constant proportional to the volumetric flow rate.
Q	[N]	Shear force.
r	[m]	Radial direction.
r_R	[m]	Optical Rayleigh resolution.
r_c	[m]	Contact radius.
R'	[m]	Reduced radius.
s	[m]	Sliding distance.
t	[s]	Time.
Th	[mm]	Thickness of the sealing disc.
$\tilde{t}$	[-]	Dimensionless time.
u,v,w	[m/s]	Local fluid velocities along the Cartesian axes.
$\boldsymbol{u}$	[m/s]	Fluid velocity vector along the Cartesian axes.
$\tilde{u}$,$\tilde{v}$,$\tilde{w}$	[-]	Dimensionless velocities along the Cartesian axes.
u_d	[m]	Elastic deformation of the surface.
V	[m^2]	Wear volume per sliding distance $2r_\mathrm{c}$.
U_0,V_0,W_0	[m/s]	Characteristic velocities along the Cartesian axes.
W_d	[m^3]	Volume of wear debris.
x,y,z	[m]	Axes in the Cartesian coordinate system.
$\tilde{x}$,$\tilde{y}$,$\tilde{z}$	[-]	Dimensionless lengths along the Cartesian axes.
X_0,Y_0,Z_0	[m]	Characteristic lengths of the control volume.

Greek Symbols	**Dimension**	**Description**
α	[-]	Viscosity-pressure coefficient of Barus.
α_d	[deg]	Chamfer angle.
β	[-]	Curvature of asperity.
γ	[-]	Ratio between height h and outlet height h_2.
ε	[-]	Mechanical strain.
η	[Pa·s]	Dynamic fluid viscosity.
κ	[MPa]	Bulk modulus.
λ	[-]	Lubrication coefficient.
μ	[-]	Coulomb friction coefficient.
ν	[-]	Poisson's ratio.
ρ	[m^3/kg]	Fluid density.
σ	[Pa]	Mechanical stress.
σ_s	[-]	Standard deviation of the asperity peak height.
σ_θ	[Pa]	Compressive hoop stress.
σ_rc	[Pa]	Compressive radial stress.
σ_rt	[Pa]	Tensile radial stress.
τ_w	[Pa]	Shear wall stress.
ϕ	[rad]	Deformation angle.
Φ_G	[-]	Gaussian probability distribution.

Subscripts

Symbol	**Description**
1	Inlet.
2	Outlet.
a	Asperity.
f	Fluid.
fric	Friction.
n	Normal to the surface.
opt	Optimum value.

Acronyms

Symbol	**Dimension**
FEA	Finite Element Analysis.
GF	Gauge Factor.
LHS	Left Hand Side.
NA	Numerical Aperture.
OPEX	Operating Expenditure.
QE	Quantum Efficiency.
RHS	Right Hand Side.

1

Introduction

This chapter explains what pigs are and how they are applied in pipelines. Common problems when designing and operating pigs will be addressed. The aim of this chapter is to gain insight in the basic forces that occur during pigging operations. First, A brief background of this device will be presented. Second, the purpose of pigging and the types will be explained. Third, the benefits and characteristics of bypass pigs will be investigated. Finally, some research topics on the physics of bypass pigs are reviewed and the research objectives for this thesis project will be formulated.

1.1. Background

Oil and gas companies extract hydrocarbons from many reservoirs around the world. Pipelines are a cost effective way to transport large quantities of these fluids from one place to another, while having a limited environmental impact. A continuous flow of these fluids must be ensured to meet the demand. The cost efficiency of pipelines depends upon three factors [25]:

- Continuous throughput
- Keeping corrosion to a minimum
- Keeping pumping or compressor costs to a minimum

A restricted throughput of pipelines leads to significant losses in revenue [24]. Corrosion, sediment and chemical deposition could restrict the throughput in pipelines that transport hydrocarbons. Deposition inside the pipeline contributes to an increase in the pressure drop along the pipeline. When the accumulation of debris increases, also the pumping costs increase. A proper maintenance of the pipeline prevents the occurrence of these inefficiencies and has a significant influence on the operational expenditure (OPEX) of the pipeline. Besides restricting the flow of fluids, the same problems can also compromise the integrity of the pipeline. Incidents due to leaks in the transport of hydrocarbons can have a serious impact on safety and the environment. For oil and gas companies, these incidents also result in reputation damage in addition to the production loss and repair costs.

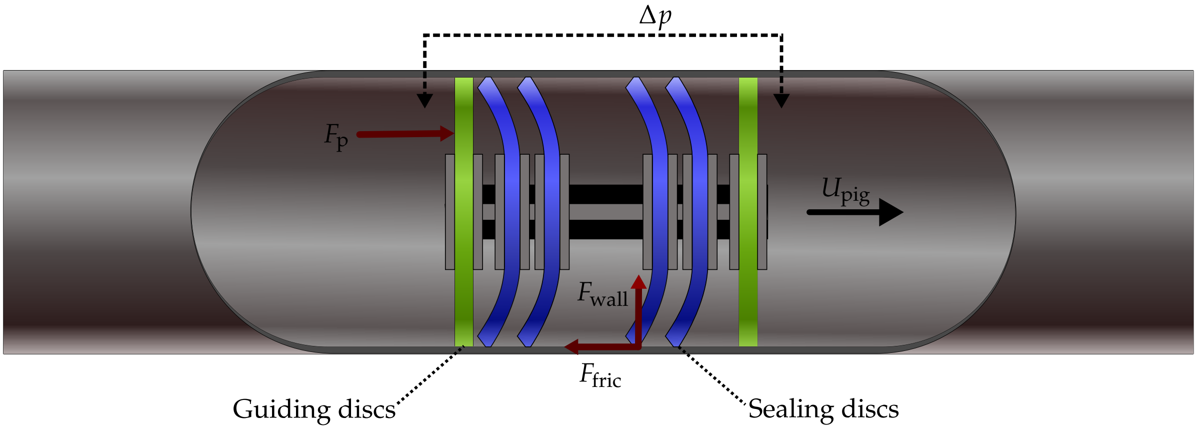

Figure 1.1: Schematic of a bypass pig.

A pipeline inspection gauge (pig) is a device that can aid to the cost-effective maintenance to preserve the integrity of the pipeline and prevent restricted throughput. As depicted in Figure 1.1, the driving force F_p, generated by the pressure difference ΔP between the front side and the backside of the pig, provides the necessary thrust to move the pig through the pipe. In the opposite direction, the friction force F_{fric} between the sealing disc of the pig and the pipeline wall slows down the pig. The sealing discs on the pig are confined in the pipeline to maintain the pressure difference and to clean the inner pipeline wall. The resultant of the friction and driving force determines the actual net force on the pig.

Pigs can be classified into three categories that describe their purpose:

- **Cleaning/Maintenance pigs:** used to clean the pipeline to ensure continuous throughput, operational efficiency and to make the line suitable for intelligent pigging. Reasons for utilizing these pigs are:
  - Corrosion management;
  - Removal of solids and liquids;
  - Separation between products (batching).

- **Intelligent inspection pig:** used to inspect pipelines, gather information on the condition of the line and assess the location and severity of any defects (cracks, pits, etc).

- **Gel pigs:** when two cleaning/maintenance pigs are sealed together by a liquid gel, gel pigs are created. They can optimize debris or water removal in specific situations.

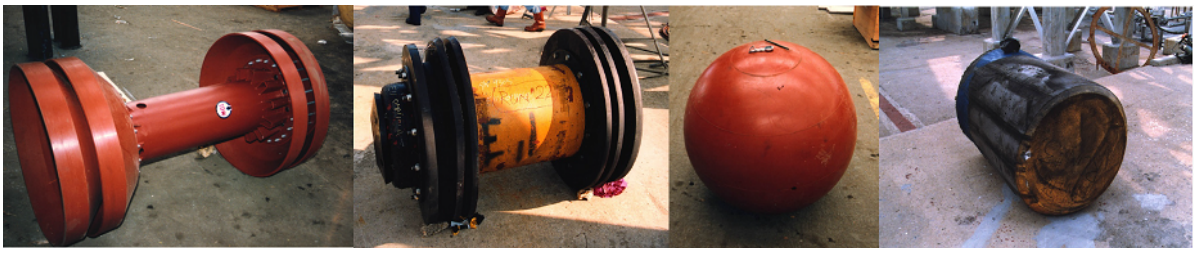

Figure 1.2: Four common pig types: cup pig, bidi pig, spherical pig and foam pig [15].

Some commonly used cleaning pigs are the foam pig, the spherical pig, the cup pig and the bi-directional (bidi) pig, that are shown in Figure 1.2. The foam pig, the spherical pig and the cup pig are less effective than the bidi pig, but useful when there is not enough liquid handling capacity at the receiving station for the formed liquid slug or when the risk of pig stalling is too high. For more detailed information about different pig types and their applications the reader is referred to the fourth edition of Tiratsoo's book on *Pipeline pigging and integrity technology* [29].

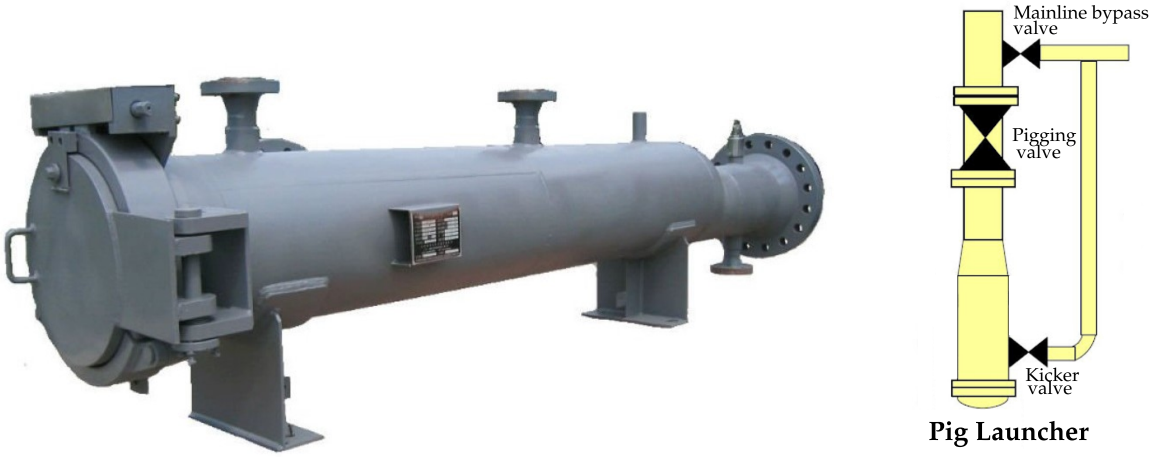

(a) [A pig launcher with a kicker and by-pass valve.

(b) Schematic of a pig launcher installation.

Figure 1.3: Pig launcher illustrations.

Pigs are inserted into a pipeline through the use of pig launchers at the upstream end of the pipeline section (see Figure 1.3a) and extracted from it with the help of a pig receiver at the downstream end. The launcher and the receiver redirect the flow to ensure that no production interruptions occur when the pigs are ready to be launched or received. Figure 1.3b shows a schematic set-up of a pig launcher. The pigging, kicker and mainline bypass valve control the flow through the barrel and establish a pressure build-up behind the pig. When the pig is launched, the flow can be directed along the mainline bypass valve again.

1.2. Bypass pigging

Typical pigging velocities range between 0.2 m/s and 6 m/s for liquid removal and between 0.2 m/s and 3 m/s for debris removal [27]. Higher pig velocities could damage the pig or the pipeline. Pigs running at lower velocities have an increased risk of stalling and experience excessive wear [15]. The velocity of a pig is determined by the (mixture) velocity of the production fluids, which means that the production rates will have to be reduced for pigs that require lower velocities. These restrictions in production lead to higher rates of deferment, which is undesired in the oil and gas business. As shown in figure 1.4a, bypass pigs do not pose restrictions on the mixture velocity in pipelines since the valves allow fluids to bypass the pig and avoid production deferment. Bypass pigs run within the desired pigging velocity range and produce hydrocarbons at normal production rates.

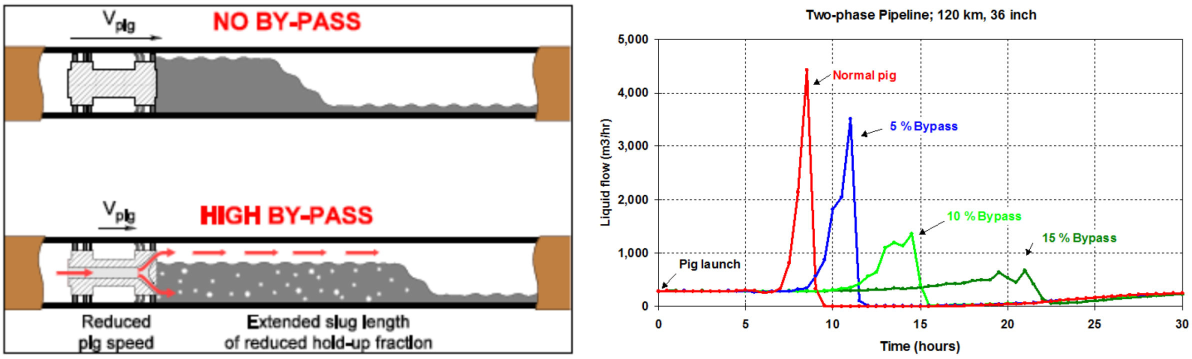

(a) Comparison between the slug generated by a conventional pig and a bypass pig [22].

(b) Liquid outflow rate as function of time for various bypass ratios [22].

Figure 1.4: The favorable features of bypass pigging.

Another point of consideration is the liquid slug that is produced by the pig. In a multiphase flow pipeline, liquids and solids travel slower than gas. A standard pig travels with the local mixture velocity. This means that liquids and solids in front of the pig are collected to form a liquid slug or a wax plug, respectively. When the slug is large enough, a slug catcher must be installed at the receiving station to temporary store liquid surges. This ensures an uninterrupted supply of gas to the downstream plant [15]. The size of a slug catcher is directly related to the maximum liquid volume it should temporarily store and is often adjusted to the expected accumulated liquid between pigging intervals. A larger size of a slug catcher will also give higher construction costs which should be kept low, while still ensuring continuous production. A bypass pig can significantly reduce the liquid outflow rate of the generated slug as illustrated in Figure 1.4a. The gas that is pressurized through the bypass pig increases the void fraction in the slug in front of the pig and extends its length, which brings down the peak liquid volume at slug arrival [15, 22]. Figure 1.4b shows a typical liquid outflow rate at the end of a pipeline as function of time. The liquid outflow rate remains at its steady state until the pigged slug arrives at the outlet of the pipeline. Bypass pigs can considerably reduce the slug catcher size with related cost savings of tens to hundreds of millions USD [25]. Depending on the liquid processing capacity of the receiving station, slug catchers may not even be required anymore at high bypass ratios.

Bypass pigs are also useful in pigging waxy pipelines. As shown in Figure 1.5a, a conventional pig collects all wax in the pipeline and generates a solid body of wax, which is then pushed through the pipeline. This wax plug causes friction that could lead to a stuck pig. Bypass pigs still collect all wax with the same efficiency, but the bypassing flow prevents the solid wax plug to be formed: it transports the wax as a slurry instead [22]. An impression of this slurry is given in Figure 1.5b.

The downside of using higher bypass ratios is the increased stalling risk. A stuck pig causes production losses and removal costs, which can be significant. On the other hand, stuck bypass pigs still allow the production flow to continue to a certain extent, while stalled conventional pigs will fully obstruct the flow. It is clear that the bypass ratio is an important decision criterion in a pigging operation and has risks assiciated with it. To minimize these risks, bypass pigs can be equipped with automated

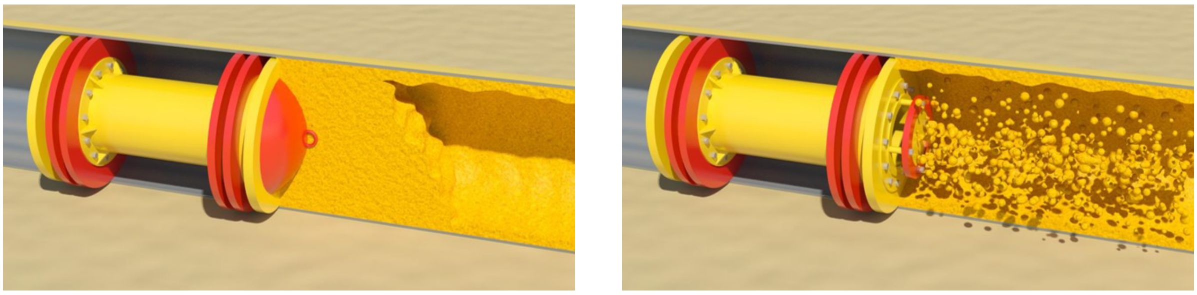

(a) A solid wax plug is generated and pushed through the pipeline.

(b) The bypassing flow through the pig causes the collected wax to be transported as a slurry .

Figure 1.5: Comparison in solids handling of a normal pig and a bypass pig.

velocity control. Instead of a fixed bypass area these cruise control bypass pigs have valves that adjust the bypassing flow to match the desired pigging velocity. For example, when the pig would suddenly measure a deceleration as a result of a higher wall friction or a change in the inclination of the pipeline, the bypass ratio would be decreased to create more thrust and increase the velocity. The other way around, a reduction in wall friction or an acceleration of the pig, would increase the bypass ratio to lower the velocity.

Many research papers have been published to aid to the design of pigs and increase the efficiency. The frictional force between the pipeline and the pig is the research topic that will be the focus of this study. Until today, no sophisticated models exist to predict the friction of pigs during operations. The industry standard is still based on relatively simple models compared to more advanced tribological models that are available for ball bearing designs. While this relates to steel contacts, the same principles could be applied to seals. An important distinction will be made between dry and lubricated friction on sealing discs. Pigs can come across dry parts in gas pipelines, but are often lubricated with condensate in gas-condensate systems, which reduces both the friction and wear on these devices.

The aim of this thesis is to investigate the dependencies of the friction forces on bypass pigs and assess available friction models for their application in predicting the friction forces. An experimental set-up was built to investigate the effects of load, sliding velocity and lubricant on the sealing disc friction. Validation of the experimental results with the outcomes from the friction models will determine whether the selected models are accurate enough to predict the friction force.

1.3. Literature review

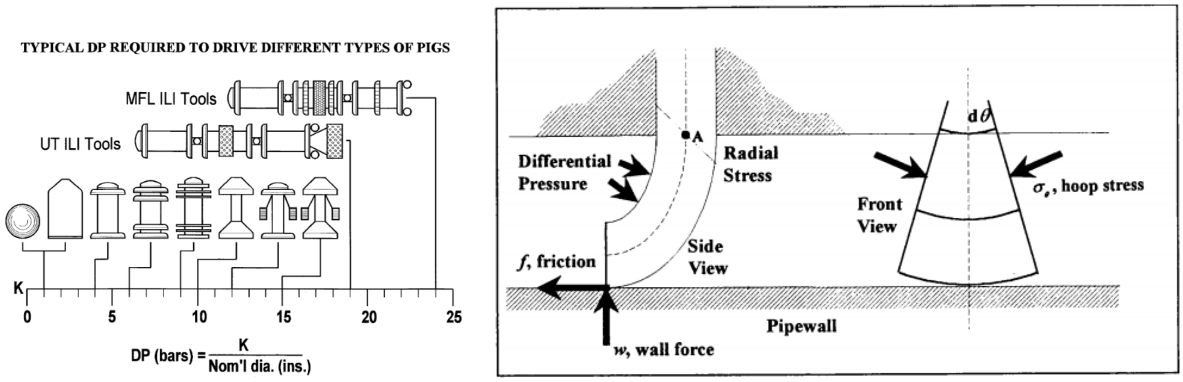

(a) Cordell's model [8]

(b) O'Donoghue's wall force prediction model [25].

Figure 1.6: Pig friction models.

Only a few models are available to predict the friction force on the sealing discs of pigs. One of the oldest models that is still being used is Cordell's model [8]. Figure 1.6a shows the differential pressure necessary to overcome the friction force acting on a specific type of pig with a specific nominal diameter. The factor K is designed to capture the frictional properties of a specific type of pig and to maintain a pigging velocity between 1 to 5 m/s [29]. The model also suggests that the pressure drop is inversely related to the nominal diameter. This suggests that Cordell keeps the friction force per unit circumference constant. The fact that this model is still used as an engineering tool in the industry indicates the need for more knowledge on the pig friction behaviour.

O'Donoghue proposes a more sophisticated method to predict the friction on pigs [25]. As shown in Figure 1.6b, this model uses a detailed force balance to determine both the friction and wall force on a axisymmetric sealing disc moving through a pipeline. O'Donoghue suggests to use an axisymmetric approach in modelling the sealing disc [25]. Assuming that this is valid, the contact can be considered as any other (flat) sliding surface. Coulomb made an important contribution to this type of sliding friction by defining the ratio between the friction force and the wall force as the Coulomb friction coefficient. Coulomb also assumed that the kinetic friction is independent of the sliding velocity. However, this is only valid if the contact between two surfaces is not lubricated.

Pigs often operate in a wide range of physical conditions, which leads to a variety of friction values depending on the regime of lubrication they are in [10]. The Stribeck curve (see Figure 1.7a) is a method to map the variation in the friction behaviour over a range of sliding velocities. Three regimes can be distinguished: boundary lubrication, mixed lubrication and hydrodynamic lubrication. Hersey further developed the Stribeck curve by tribological experiments and related the friction coefficient to the so-called lubrication coefficient [25]. This lubrication coefficient is the sliding speed multiplied by the lubricant viscosity and divided by the load on the contact surfaces. An important difference between Coulomb friction (dry) and lubricated friction is the recognition of surface roughness. This introduces partial contact states in which a fraction of the load is carried by the asperities on the surfaces and the remaining load by the hydrodynamic pressure in the lubricant.

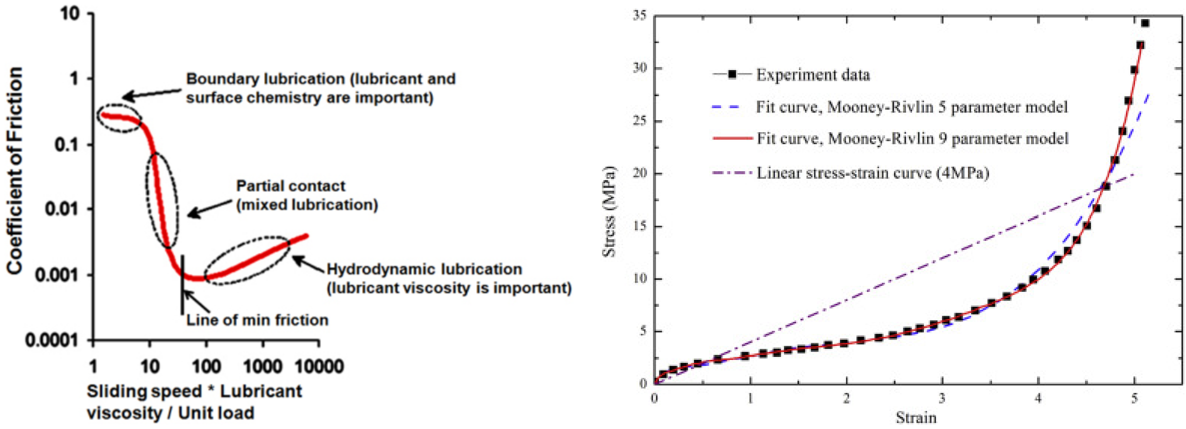

(a) Stribeck Curve with denoted lubrication regimes [8].

(b) Zhu's comparison between linear and nonlinear stress-strain curve fitting [35].

Figure 1.7: Fundamental principles in recent pig friction literature.

O'Donoghue used the Inverse Hydrodynamic Lubrication (IHL) model to determine which regime a simulated pig was operating in [25]. He validated this model with a 10" pig run in a 130 m long pipeline in a test facility. Another 260 m flow loop was used for wear trials. Concluding remarks stated that the wall force is computed successfully, but the lubrication fluid pressure lacks continuity and does not conserve continuity of flow in the seal [25].

Zhu et al. published a study in which a hyperelastic Mooney-Rivlin model was used to investigate the effect of oversize, thickness, chamfer and clamping ratio on the imposed wall force [35]. Furthermore, the deflection of the sealing disc is investigated under varying differential pressures. Figure

1.7b shows a comparison of material stress strain data fitted with the linear model and the nonlinear Mooney-Rivlin model. It is clear that the complex stress strain behaviour is not linear and can be fitted more accurately by a nonlinear model. Their modelling results are validated with a pig pull experiment in a pipeline segment. The simulation results gave good agreement with relative errors of approximately 10%.

A new attempt to model the friction forces on pigs was done by Den Heijer, who built a static pig pull experiment [9]. That experiment was focused on determining the ratio between the static friction force and the wall force for different sealing disc oversizes. The set-up consists of a flexible hull that surrounds the sealing disc and transducers that measure two pulling forces: one that tightens the hull and one connected to the centre of the sealing disc to pull the sealing disc through. These results are validated with a Finite-Element Method (FEM) analysis, which showed reasonable agreement.

Graafland et al.[14] continued the work of Den Heijer and Hendrix [9] by enhancing the accuracy of the static pig pull and using a new setup called the dynamic pig pull. The static pig pull set-up of Den Heijer and Hendrix seemed to have measured internal forces due to improper guidance of the flexible hull around the sealing disc. Roller bearings have been implemented in the design to reduce the friction that occurs in tightening the flexible hull. Results from the static pig pull have improved in relation to the FEM results after the modification. The dynamic pig pull was designed to investigate the dynamic friction force on the sealing discs by pulling these through a pipeline segment. The sealing disc is attached to a transducer that measures the pulling force needed to overcome the friction at a certain pulling velocity and disc oversize. The results of the dynamic pig pull are linked to those from the static pig pull to obtain an average friction force for the dry and lubricated cases.

The work carried out by Graafland was focused on both dry and lubricated friction. Nonetheless, there is still a need to make a further investigation with respect to the pigging velocity and sealing disc design. Research that maps the effects of these parameters on friction force would add some more parameters to the current pig friction models in the industry. In the ideal case several Stribeck curves can eventually be drawn with corresponding experimental data and simulation results. This could serve as a more sophisticated rule of thumb.

1.4. Research questions

Main research question:

> *How does the lubricated friction force acting on a pipeline pig depend on the sealing disc design and the operating conditions?*

Subquestions:

- How does the friction force depend on the operating conditions of a pig?
- What is the relation between the velocity of the pig and the friction coefficient?
- How is the friction force acting on a pig related to the viscosity of the production fluids?
- How does the design of the sealing disc affect the frictional behaviour of the pig?

1.5. Outline

To answer these questions a series of models were assessed in the literature study that give insight in the encountered phenomena. Chapter 2 determines what model is suitable to predict the friction coefficients and to describe the physics behind pigging operations. The same chapter also describes simulations of a nonlinear FEM model that was used to determine the wall forces on the sealing disc. The experimental set-up is described in Chapter 3. This chapter provides properties of the newly built facility and the methodology behind the experiments. The results of the research are presented in Chapter 4 and validated with the presented friction model. A discussion of the results is given in Chapter 5, followed by the conclusions and recommendations in Chapter 6.

2

Friction models

The aim of this chapter is to investigate the physics behind lubricated friction and to find a suitable model that can be used to validate the friction forces obtained by experiments. The first section of this chapter will give an introduction on the basic friction physics. The second section will explain hydrodynamic lubrication and how this phenomenon plays a role in the friction forces that act on a pig. This is done by using the Navier-Stokes equations and by considering the scaling laws that indicate the relative importance of the involved forces. In the next section the mixed lubrication regime will be explained by adding contact mechanics to hydrodynamic lubrication theory. Some closure relations are then shown that will be used to build a model that can predict the friction for a wide operating envelope of the pig. A section about boundary lubrication will cover wear. The last section of this chapter will explain the used Mooney-Rivlin model and how it relates to linear FEM models.

2.1. Frictional behaviour of bypass pigs

To illustrate the importance of friction modelling, the analogy can be made with hydroplaning of cars on wet roads. When the velocity of the car is high enough, the tyres start floating on wet parts on the surface and the traction is reduced. Wet parts on the road should therefore be avoided. Oil puddles would be even worse and should thus also be avoided. The lubricated contact between a pig seal and the inner pipeline wall can also be considered as a tire on a wet road surface. This chapter will show that higher sliding velocities will increase the separation between the contact surfaces through hydrodynamic pressure in the lubricant.

The friction forces that act on a bypass pig depend on several factors:

- Surface roughness,
- Velocity,
- Presence and type of lubricant,
- Oversize of the sealing disc,
- Sealing disc material,
- Differential pressure.

During pigging operations the surface roughness of the inner pipeline wall affects the frictional behaviour of the pig. An increase in roughness leads to higher friction forces and wear on the sealing discs. The velocity of the pig affects the type of contact between the seal and the wall. Just as in the hydroplaning example, a higher velocity will increase the chance of floating on the lubricant and it will reduce the friction. The wall force on the sealing discs has a direction perpendicular to the pipeline wall and depends on the oversize of the disc. Larger oversizes and seal materials with a higher elastic modulus lead to tighter confined pigs. The differential pressure is distributed over the sealing discs and affects the friction force with its vertical force component.

Generally, two types of friction act on a bypass pig: dry friction and lubricated friction. In dry friction there is no lubricant present between the contacting surfaces, whilst with lubricated friction a lubricant is involved. In the context of pigging operations, dry friction could occur in dry gas pipelines or in sections of gas-condensate pipelines where the contact between the seal and the pipeline is not lubricated by any condensate. In both gas and oil pipelines there are sections where the sealing disc can be fully lubricated by hydrocarbons (or with water that is co-produced with the hydrocarbons).A distinction can be made between lighter and heavier hydrocarbons. A light hydrocarbon liquid like condensate will have a different effect on the friction force than heavier hydrocarbons and waxes due their viscosity. Condensates and water will be the main lubricants studied in this report.

2.1.1. Dry friction

The simplest model of dry friction is Coulomb friction, which assumes that the frictional force is equal or less than the product of the normal force on a surface and a friction coefficient. Note that the friction force corresponds to a certain threshold that needs to be overcome to bring the object into motion. If the driving force is smaller or equal to the friction force, the object will not come into motion. Coulomb friction is described by

$$F_{\text{fric}} \leq \mu F_{\text{n}}, \tag{2.1}$$

in which F_{fric} is the friction force, μ is the Coulomb friction coefficient and F_{n} is the normal force perpendicular to the surface. Friction coefficients found in the literature vary from 0.23 to 1.30 for sealing discs made of polyurethane rubber [11, 21, 25, 28, 34]. This variety shows that the friction coefficient is a complex parameter to predict and needs to be defined for a specific application. This stresses the need for a model that can predict friction coefficients over a larger spectrum of operating conditions.

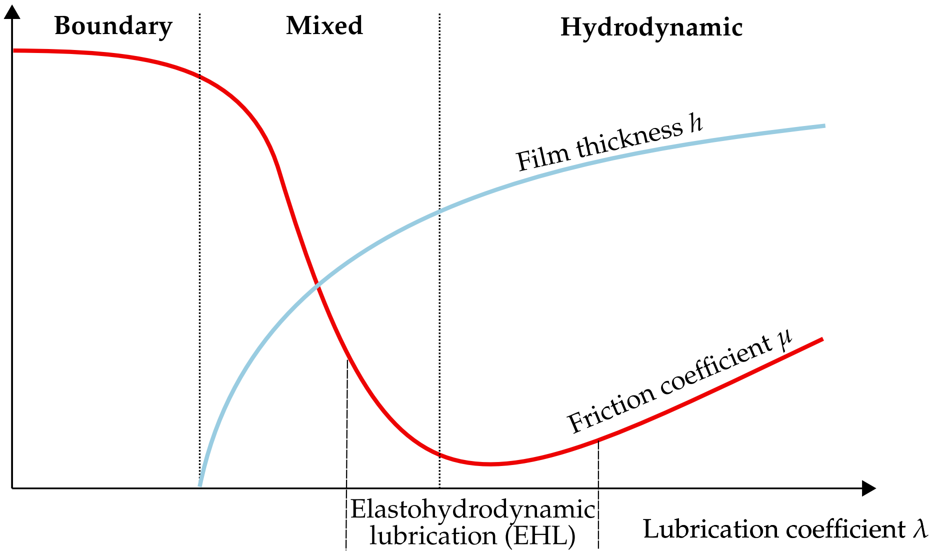

Figure 2.1: The Stribeck curve provides the friction coefficient as a function of the lubrication coefficient and distinguishes several regimes.

2.1.2. Lubricated friction

In gas-condensate pipelines both condensate and water can act as a lubricant. This leads to a reduction of the frictional forces compared to dry friction. The presence of a lubricating film between the sealing disc and the pipeline wall also introduce extra factors that affect the friction coefficient. The Stribeck curve, shown in Figure 2.1, describes the friction coefficient between sliding contacts as a function of a lubrication coefficient:

$$\lambda = \frac{U_0 \eta}{L}, \tag{2.2}$$

where U_0, η and L are the sliding velocity, lubricant viscosity and load, respectively. During lubricated sliding motion, the pressure between the contacting surfaces can be split into hydraulic pressure and asperity pressure. When the lubrication coefficient decreases, the highest asperities on the surface carry larger fractions of the load. The Stribeck curve can be divided into three regimes:

- **Boundary lubrication:** describes a state in which the surfaces are in close contact and the friction coefficient is high and constant [10]. Asperities in the surfaces are fully sealed by the contact and the highest asperities carry approximately 90% of the load. In this regime the friction force is not very sensitive to variations in operating conditions such as load and velocity. When the lubricating film starts to develop between the two surfaces, the friction coefficient drops and the mixed lubrication regime is entered.

- **Mixed lubrication:** asperities make contact between the sliding surfaces, but there is stil a significant film between the surfaces that contributes to the pressure. This regime is highly sensitive to variations in load and velocity. As the lubrication coefficient rises even more, by either increasing the velocity or decreasing the load, the minimum of the Stribeck curve is passed and the hydrodynamic lubrication regime is reached.

- **Hydrodynamic lubrication:** the lubrication layer is thick enough to keep the roughness elements and asperities separated. Friction in this regime is dominated by fluid forces. The friction values in this regime are determined by hydrodynamic pressures and shear strains acting on the fluid. The forces in this regime can be calculated by considering two surfaces that are fully separated by a fluid and by using the Reynolds equation to determine the pressure distribution.

- **Elastohydrodynamic lubrication:** is an overlapping regime between hydrodynamic lubrication and mixed lubrication, in which significant elastic deformations of the contacting surfaces occur due to high fluid pressures. This also alters the shape and thickness of the lubrication film between the contact surfaces. Recognition of elastichydrodynamic deformations between the contacting surfaces in lubrication models leads to completely different pressure distributions and friction mechanisms.

The first three regimes are the original regimes of classical hydrodynamic lubrication theory for rigid objects [33]. Elastohydrodynamic lubrication (EHL) relates the hydrodynamic pressure between asperities to elastic surface deformation.

2.2. Hydrodynamic lubrication

Hydrodynamic lubrication is the regime in which two curved or flat surfaces are fully separated by a lubricant, such that even the highest asperities cannot make physical contact with each other. This regime is highly favourable for pigging since it reduces both friction and wear in comparison with the other lubrication regimes.

The main purpose of this section is to gain insight in the basic physics of hydrodynamic lubrication. By starting from the Navier-Stokes equations a derivation of classical lubrication theory, applicable to Newtonian fluids, is given. Next, practical relations are derived with corresponding optimum values. Then some extensions to the classical theory found in the literature are reviewed.

2.2.1. Navier-Stokes equations

The Navier-Stokes equations describe the motion and forces of viscous fluids. They model the fluids as continuous volumes instead of discrete particles. Furthermore, a solution to these equations only exist when the fluid parameters are at least weakly differentiable. Since the Navier-Stokes equations are very time consuming to solve on a computer, assumptions suitable for the considered problem are introduced to simplify the equations. As chapter 1.1 pointed out, the fluids between the sealing disc of a pig and the pipe wall can both be gas or liquid. Since gas-condensate pipelines are the scope of this report, the fluid will assumed to be incompressible liquid. Furthermore, the considered liquid is assumed to be Newtonian.

Assumptions

1. **Continuum mechanics:** the fluid is described by continuous mass rather than discrete particles.
2. **Differentiability:** all fluid parameters in the model are at least weakly differentiable.
3. **Newtonian fluid:** The viscous stresses follow Newton's constitutive relation.
4. **Incompressibility assumption:** the density of the fluid is constant.

After imposing these assumptions and simplifying the original equations, the conservation of mass becomes:

$$\nabla \cdot \boldsymbol{u} = 0. \tag{2.3}$$

Here $\boldsymbol{u}$ denotes the velocity vector along the Cartesian axes:

$$\boldsymbol{u} = \begin{pmatrix} u \\ v \\ w \end{pmatrix}. \tag{2.4}$$

Similarly conservation of momentum becomes:

$$\rho \left(\frac{\partial \boldsymbol{u}}{\partial t} + \boldsymbol{u} \cdot \nabla \boldsymbol{u} \right) = -\nabla p + \eta \nabla^2 \boldsymbol{u} + \boldsymbol{f}. \tag{2.5}$$

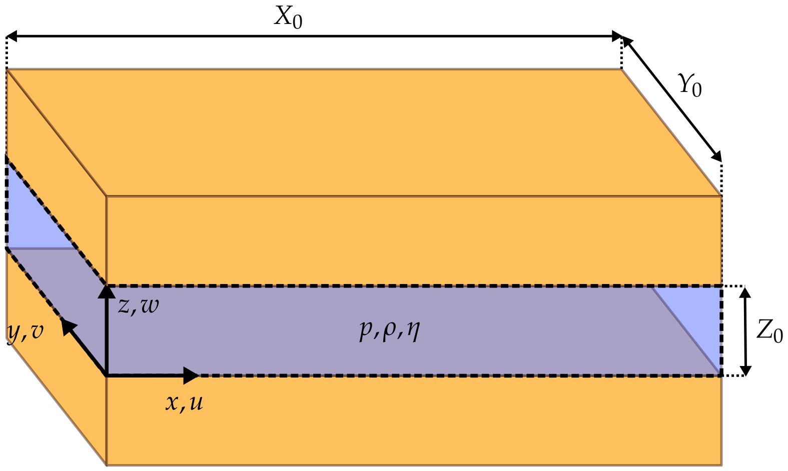

Figure 2.2: Control volume of a thin fluid film.

Here ρ denotes the fluid density, p the pressure, η the dynamic viscosity and $\boldsymbol{f}$ the vector of external forces. The external force in hydrodynamic lubrication can be magnetic or gravitational. Magnetic influences are outside the scope of this report. Only gravitational forces are considered:

$$\boldsymbol{f} = \begin{pmatrix} 0 \\ 0 \\ -\rho g \end{pmatrix}, \tag{2.6}$$

in which g is the gravitational acceleration. For fluids that are confined between the sealing disc and the pipe wall, the characteristic lengths of the fluid X_0 and Y_0 are considerably larger than the characteristic film thickness (see Figure 2.2). Therefore, some terms in the momentum equation will become negligible.

Assumption

5. **Thin film:** The characteristic height Z_0 between the two moving surfaces is significantly smaller than the characteristic length X_0 and width Y_0.

To see which terms can be neglected, the momentum equation is rewritten in dimensionless quantities. Consider the x-component of the momentum equation:

$$\rho(u_t + uu_x + vu_y + wu_z) = -p_x + \eta(u_{xx} + u_{yy} + u_{zz}). \tag{2.7}$$

Note that the subscripts in this equation are in the Langrangian notation for the partial differentials with respect to time and space. This makes the appearance of the equation concise and clear. The following dimensionless quantities are introduced:

$$\tilde{x} = \frac{x}{X_0}, \quad \tilde{y} = \frac{y}{Y_0}, \quad \tilde{z} = \frac{z}{Z_0}, \quad \tilde{u} = \frac{u}{U_0}, \quad \tilde{v} = \frac{v}{V_0}, \quad \tilde{w} = \frac{w}{W_0}, \quad \tilde{p} = \frac{pZ_0^2}{\eta U_0 X_0}, \quad \tilde{t} = \frac{tU_0}{X_0}, \tag{2.8}$$

where X_0, Y_0 and Z_0 are the characteristic lengths of the control volume in the x, y and z direction, respectively, shown in Figure 2.2. U_0, V_0 and W_0 are the characteristic velocities in the x, y and z direction, respectively. Substitution of the obtained dimensionless quantities results into:

$$\rho\left(\frac{U_0^2}{X_0}\tilde{u}_{\tilde{t}} + \frac{U_0^2}{X_0}\tilde{u}\tilde{u}_{\tilde{x}} + \frac{U_0V_0}{Y_0}\tilde{v}\tilde{u}_{\tilde{y}} + \frac{U_0W_0}{Z_0}\tilde{w}\tilde{u}_{\tilde{z}}\right) = -\frac{\eta U_0}{Z_0^2}\tilde{p}_{\tilde{x}} + \eta\left(\frac{U_0}{X_0^2}\tilde{u}_{\tilde{x}\tilde{x}} + \frac{U_0}{Y_0^2}\tilde{u}_{\tilde{y}\tilde{y}} + \frac{U_0}{Z_0^2}\tilde{u}_{\tilde{z}\tilde{z}}\right). \tag{2.9}$$

Multiplying this with X_0^2/U_0 and after some algebraic manipulation, the Reynolds number appears in front of the inertial terms:

$$\frac{\rho U_0 X_0}{\eta}\left(\tilde{u}_{\tilde{t}} + \tilde{u}\tilde{u}_{\tilde{x}} + \frac{X_0 V_0}{Y_0 U_0}\tilde{v}\tilde{u}_{\tilde{y}} + \frac{X_0 W_0}{Z_0 U_0}\tilde{w}\tilde{u}_{\tilde{z}}\right) = -\frac{X_0^2}{Z_0^2}\tilde{p}_{\tilde{x}} + \tilde{u}_{\tilde{x}\tilde{x}} + \frac{X_0^2}{Y_0^2}\tilde{u}_{\tilde{y}\tilde{y}} + \frac{X_0^2}{Z_0^2}\tilde{u}_{\tilde{z}\tilde{z}}. \tag{2.10}$$

A similar equation is found for the momentum equation in the y-direction. However, in the z direction the gravitational term shows up and this equation is therefore slightly different:

$$\begin{aligned}\rho\left(\frac{W_0 U_0}{X_0}\tilde{w}_{\tilde{t}} + \frac{W_0 U_0}{X_0}\tilde{u}\tilde{w}_{\tilde{x}} + \frac{W_0 V_0}{Y_0}\tilde{v}\tilde{w}_{\tilde{y}} + \frac{W_0^2}{Z_0}\tilde{w}\tilde{w}_{\tilde{z}}\right) = \ldots \\ -\frac{\eta U_0 X_0}{Z_0^3}\tilde{p}_{\tilde{z}} + \eta\left(\frac{W_0}{X_0^2}\tilde{w}_{\tilde{x}\tilde{x}} + \frac{W_0}{Y_0^2}\tilde{w}_{\tilde{y}\tilde{y}} + \frac{W_0}{Z_0^2}\tilde{w}_{\tilde{z}\tilde{z}}\right) - \rho g.\end{aligned} \tag{2.11}$$

Multiplying this with $\rho X_0^3/\eta^2$ and rewriting the equation will turn the gravitational term into the Galilei number:

$$\begin{aligned}\frac{\rho^2 W_0^2 X_0^2}{\eta^2}\left(\frac{U_0}{W_0}\tilde{w}_{\tilde{t}} + \frac{U_0}{W_0}\tilde{u}\tilde{w}_{\tilde{x}} + \frac{X_0 V_0}{Y_0 W_0}\tilde{v}\tilde{w}_{\tilde{y}} + \frac{X_0}{Z_0}\tilde{w}\tilde{w}_{\tilde{z}}\right) = \ldots \\ -\frac{\rho U_0 X_0^4}{\eta Z_0^3}\tilde{p}_{\tilde{z}} + \frac{\rho W_0 X_0}{\eta}\left(\tilde{w}_{\tilde{x}\tilde{x}} + \frac{X_0^2}{Y_0^2}\tilde{w}_{\tilde{y}\tilde{y}} + \frac{X_0^2}{Z_0^2}\tilde{w}_{\tilde{z}\tilde{z}}\right) - \frac{\rho^2 g X_0^3}{\eta^2}.\end{aligned} \tag{2.12}$$

2.2.2. Scaling laws

To see which terms are dominant in thin film lubrication, scaling laws can be used. These laws indicate the relative importance of forces that act on the fluid related problems. To provide proper quantities to calculate these scaling laws, the lubrication of the sealing discs will be considered. Note that while the fluid is assumed to be Newtonian, the used viscosity corresponds to a condensate.

For the base case a pig will be considered that travels with 2 m/s in a pipeline with condensate as production fluid and an overpressure of 200 kPa. The sealing disc is assumed have a thickness of 15 mm. These particular values are extracted from [11, 15, 25, 27].

$$\begin{aligned} X_0 &= 1.5\cdot 10^2\,\text{m}, & Z_0 &= 1\cdot 10^{-5}\,\text{m}, & U_0 &= 2\,\text{m/s}, & \rho &= 600\,\text{kg/m}^3, \\ \eta &= 7\cdot 10^{-4}\,\text{Pa}\cdot\text{s}, & p_0 &= 2\cdot 10^5\,\text{Pa}, & g &= 9.81\,\text{m/s}^2. \end{aligned}$$

Reynolds number

Note the Reynolds number in front of the inertia terms in Equation 2.10. This dimensionless quantity indicates the importance of inertial forces in relation to viscous forces in fluids. In the x direction this is:

$$\text{Re}_\text{x} = \frac{\text{Inertia force}}{\text{Viscous force}} = \frac{\rho U_0 X_0}{\eta}. \tag{2.13}$$

When assuming $X_0 \ll Z_0$ the viscous term $\partial^2 u/\partial z^2$ becomes dominant in equation 2.10. The relation between the inertial and viscous forces is therefore described by a modified Reynolds number in lubrication theory. This number is different for the three Cartesian directions and becomes:

$$\text{Re}_\text{x} = \frac{\rho U_0 Z_0^2}{\eta X_0}, \qquad \text{Re}_\text{y} = \frac{\rho V_0 Z_0^2}{\eta Y_0}, \qquad \text{Re}_\text{z} = \frac{\rho W_0 Z_0}{\eta}. \tag{2.14}$$

The Reynolds number characteristic for the base case is approximately:

$$Re_x \cong 1\cdot 10^{-2}.$$

This Reynolds number is considerably smaller than unity, which means that the viscous forces in lubricated sliding are considerably larger than the inertial forces. The latter forces can therefore be neglected in a first approximation of obtaining the frictional forces.

Assumption

6. Negligible inertia: inertial forces can be neglected since the viscous forces are much larger.

Galilei number

Note the Galilei number next to the viscous forces in Equation 2.12. This number gives the ratio of gravitational and viscous forces:

$$\mathrm{Ga} = \frac{\text{Gravity force}}{\text{Viscous force}} = \frac{\rho^2 g X_0^3}{\eta^2}. \tag{2.15}$$

Calculating this ratio for the base case parameters gives approximately:

$$\mathrm{Ga} \cong 7 \cdot 10^{-3}.$$

This indicates that the viscous forces are much larger than the gravity forces and the latter can therefore be neglected. Because the Galilei number is smaller than the Reynolds number it can also be concluded that the inertia forces are larger than the gravitational forces.

Assumption

7. Negligible gravity: gravitational forces can be neglected since the viscous forces are much larger.

Euler number

The relative importance of the pressure to the inertia term can be judged from the value of the Euler number:

$$\mathrm{Eu} = \frac{\text{Pressure force}}{\text{Inertia force}} = \frac{p_o}{\rho U_0^2} \tag{2.16}$$

The ratio between the pressure p_0 and the viscous forces can be obtained when the Euler number is multiplied by the Reynolds number:

$$\mathrm{Eu} \cdot \mathrm{Re} = \frac{\text{Pressure force}}{\text{Inertia force}} \frac{\text{Inertia force}}{\text{Viscous force}} = \frac{\text{Pressure force}}{\text{Viscous force}} = \frac{p Z_0^2}{\mu U_0 X_0} \tag{2.17}$$

Note that this number is also used in Equations 2.10 and 2.12 to create a dimensionless pressure. Using the parameters of the base case yields:

$$\mathrm{Eu} \cdot \mathrm{Re} = 1. \tag{2.18}$$

Based on the used parameters in the base scenario, the pressure forces are of the same order as the viscous forces and these are therefore equally important in the calculation of the total friction force.

2.2.3. Reynolds equation

The Reynolds equation is a partial differential equation that describes the pressure distribution and local fluid velocity in a thin fluid layer. As seen in the previous subsection, the ratios calculated from characteristic values showed that the forces arising from inertia and gravity are negligible compared to viscous forces and pressure forces. The derived x-component of the dimensionless momentum equation (Section 2.2.1) is showed again here for clarity:

$$\frac{\rho U_0 X_0}{\eta}\left(\tilde{u}_{\tilde{t}} + \tilde{u}\tilde{u}_{\tilde{x}} + \frac{X_0 V_0}{Y_0 U_0}\tilde{v}\tilde{u}_{\tilde{y}} + \frac{X_0 W_0}{Z_0 U_0}\tilde{w}\tilde{u}_{\tilde{z}}\right) = -\frac{X_0^2}{Z_0^2}\tilde{p}_{\tilde{x}} + \tilde{u}_{\tilde{x}\tilde{x}} + \frac{X_0^2}{Y_0^2}\tilde{u}_{\tilde{y}\tilde{y}} + \frac{X_0^2}{Z_0^2}\tilde{u}_{\tilde{z}\tilde{z}}.$$

From the scaling laws in Subsection 2.2.2, it was shown that the Reynolds number is sufficiently small to neglect the inertia terms on the left hand side (LHS). The thin film assumption, where $Z_0 \ll X_0$ and $Z_0 \ll Y_0$, leads to a dominant term X_0^2/Z_0^2 in the x-component of the momentum equation. This leaves the pressure gradient and a viscous term:

$$\frac{\partial \tilde{p}}{\partial \tilde{x}} = \eta \frac{\partial^2 \tilde{u}}{\partial \tilde{z}^2}. \tag{2.19}$$

Note that the Leibniz differential notation is used again since this equation does not contain as many differential terms as the momentum equations.

A similar approach is used for the momentum equation in y-direction, which leads to a dominant term Y_0^2/Z_0^2 and gives:

$$\frac{\partial \tilde{p}}{\partial \tilde{y}} = \eta \frac{\partial^2 \tilde{v}}{\partial \tilde{z}^2}. \tag{2.20}$$

The dimensionless form of the momentum equation in the z-direction (Equation 2.12) shows a dominant term in front of the pressure gradient. All other terms are smaller and this gives:

$$\frac{\partial \tilde{p}}{\partial \tilde{z}} = 0. \tag{2.21}$$

This expression states that the pressure does not vary over the height of the lubrication layer.

Assumption

8. Constant pressure across the film: The pressure does not vary in the z-direction.

Note that in the remainder of this report the terms of these equations are no longer dimensionless.

Simplified case: inclined 1D rigid seal

To gain insight in the impact of hydrodynamic lubrication, the circular sealing disc will be considered as a 1D rigid seal with an inclination.

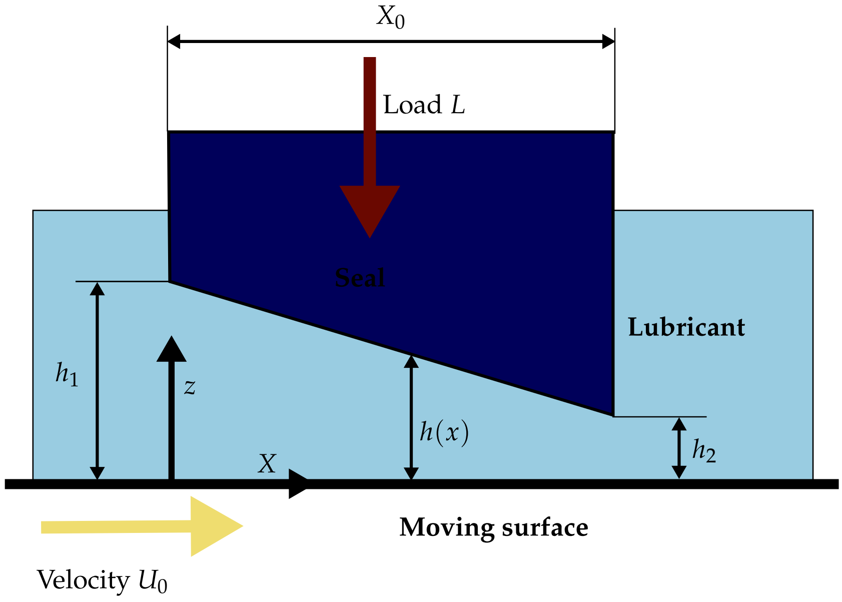

Figure 2.3: Hydrodynamic lubrication between an inclined seal and a moving surface.

In this subsection a governing equation for a 1D parallel seal will be discussed. For the complete derivation of the Reynolds equation and an explanation of all terms, the reader is referred to [13]. The 1D seal configuration assumes that the seal is of infinite width, which means that leakage at the sides is neglected. Smoothness and rigidity prohibit the sliding surfaces from deformations and partial contact. This also guarantees an analytically solvable relation. Figure 2.3 provides a schematic of a surface that slides underneath a static seal block with velocity U_0, which corresponds to the pigging application. The film thickness $h(x)$ has a linear taper along the x-direction. A load L acts on the seal and is supported by the hydrodynamic pressure field $p(x)$ in the tapered film.

Assumptions

9. Smooth surface: roughness effects of the surface on the fluid flow are neglected.

10. Rigidity: no deformations in the sliding contact surfaces.

11. No side leakage: a seal of infinite width with no leakage at the sides.

The derivation will continue with Equation 2.19. Integrating twice gives the local fluid velocity in the x-direction:

$$u = \frac{1}{2\eta} z^2 \frac{\partial p}{\partial x} + C_1 z + C_2 \tag{2.22}$$

A no-slip condition at the surface assures that the flow has the same velocity there as the (moving) walls. The vertical motion of the seal surface $\mathrm{d}h/\mathrm{d}t$ is assumed constant, which means that the load on the seal is steady and the gap height is time-independent. This gives the following boundary conditions to the problem:

$$u(z=0) = U_0, \tag{2.23}$$
$$u(z=h) = 0, \tag{2.24}$$
$$w(z=h) = 0, \tag{2.25}$$
$$w(z=0) = 0. \tag{2.26}$$

Assumptions

12. No slip condition: the flow does not slip at wall boundaries.

13. Steady load: the gap height Z_0 is time-independent.

Substituting the first two boundary conditions in Equation 2.22 gives:

$$u(x,z) = \frac{1}{2\eta}\frac{\partial p}{\partial x}(z^2 - hz) + U_0\left(1 - \frac{z}{h}\right). \tag{2.27}$$

Mass conservation by applying Equation 2.3 gives:

$$\frac{\partial w}{\partial z} = -\frac{\partial}{\partial x}\left[\frac{1}{2\eta}\frac{\partial p}{\partial x}(z^2 - hz) + U_0\left(1 - \frac{z}{h}\right)\right]. \tag{2.28}$$

Integration from $z = 0$ to $z = h$ and using Equation 2.25 and 2.26 leads to the 1D Reynolds equation:

$$0 = \frac{\partial}{\partial x}\left(\frac{h^3}{12\eta}\frac{\partial p}{\partial x} - \frac{U_0}{2}h\right). \tag{2.29}$$

Solution procedure

Define the following dimensionless quantities:

$$\tilde{x} = \frac{x}{X_0}, \qquad \tilde{p} = \frac{ph_2^2}{6\eta U_0 X_0}, \qquad \tilde{h} = \frac{h}{h_2}, \qquad \gamma = \frac{h_1}{h_2}. \tag{2.30}$$

With h_1 and h_2 defined as the film thickness at the inlet and outlet of the seal, respectively. Substituting these quantities in Equation 2.29 leads to:

$$\frac{\mathrm{d}}{\mathrm{d}X}\left(\tilde{h}^3\frac{\mathrm{d}\tilde{p}}{\mathrm{d}\tilde{x}} - \tilde{h}\right) = 0. \tag{2.31}$$

This is essentially a dimensionless form of the mass conservation. Integration of the dimensional expression would give the volumetric flow rate on the right hand side (RHS). The dimensionless derivation renders a dimensionless constant $\tilde{q}_x$ that is proportional to the volumetric flow rate q_x:

$$\left(\tilde{h}^3\frac{\mathrm{d}\tilde{p}}{\mathrm{d}\tilde{x}} - \tilde{h}\right) = -\tilde{q}_x = \frac{2q_x}{h_2 U_0}. \tag{2.32}$$

To solve this equation, the relative pressure p is assumed to be zero at the inlet and outlet of the seal, which gives the boundary conditions:

$$\tilde{p}(\tilde{x} = 0) = 0, \tag{2.33}$$

$$\tilde{p}(\tilde{x} = 1) = 0. \tag{2.34}$$

After integration of Equation 2.32 and application of the boundary conditions, the dimensionless pressure distribution can be obtained:

$$\tilde{p}(\tilde{x},\gamma) = \frac{\gamma}{1-\gamma^2}\left(\frac{1}{\tilde{h}(\tilde{x},\gamma)^2} - \frac{1}{\gamma^2}\right) - \frac{1}{1-\gamma}\left(\frac{1}{\tilde{h}(\tilde{x},\gamma)} - \frac{1}{\gamma}\right). \tag{2.35}$$

The dimensionfull pressure distribution can now be determined by substituting equation 2.35 and 2.36. A series of pressure distributions are shown for film ratios γ from 1.001 to 4 in Figure **??**. Shown is the relation between the dimensionfull pressure and the downward slope γ of the seal. For this configuration water is used as lubricant and the following physical parameters.

$$\eta = 0.001\, Pa \cdot s, \qquad U = 1\, m/s, \qquad X_0 = 0.04\, mm, \qquad L = 500N. \tag{2.36}$$

The required outlet height h_2 that corresponds to a load of 500 N is calculated by using Equation 2.37. An almost flat seal corresponds to the parabolic shaped pressure distribution that is nearly symmetrical. Increasing the slope shifts the peak of the graph to the right and increases the maximum pressure. The zero slope case is not shown, because the Reynolds equation then reduces to the Couette flow equation. This type of flow has no overpressure between surfaces since the outflow and inflow characteristic lengths Z_0 are the same.

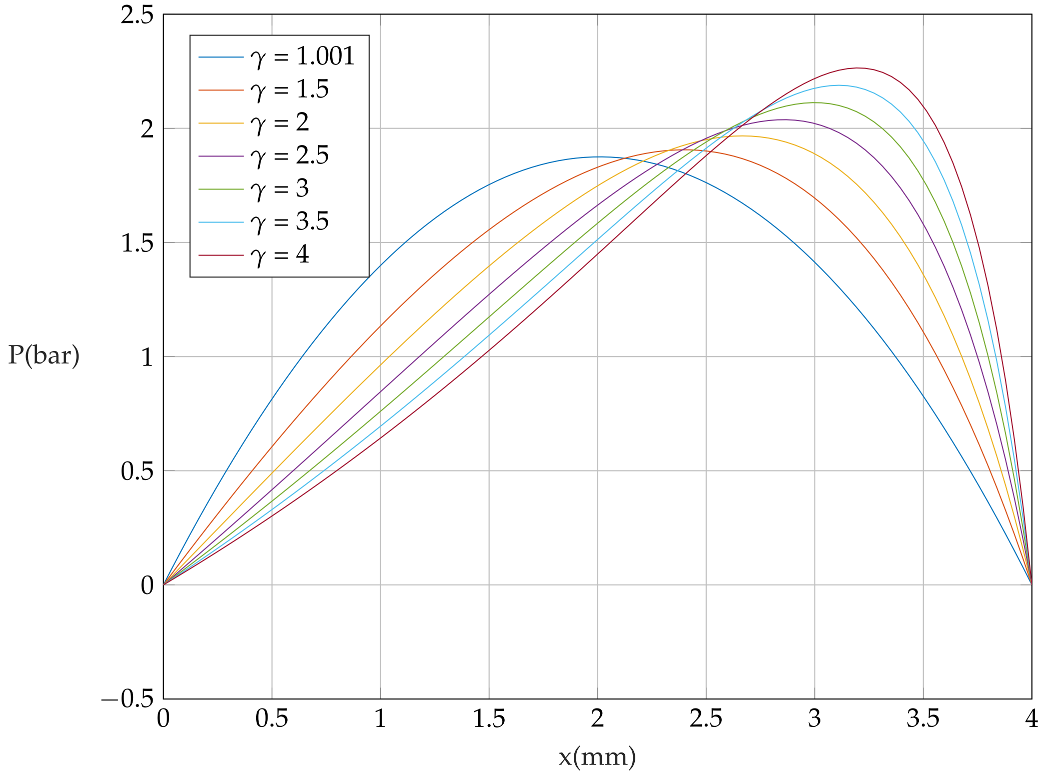

Figure 2.4: Pressure distribution underneath a rigid seal for various inclination ratios with water as lubricant. L = 500 N, U = 1 m/s.

Integration of the pressure field over length X_0 gives the load on the seal:

$$L = \int_0^{X_0} p(x)\mathrm{d}x = \frac{6\eta U_0 X_0^2}{h_2^2}\tilde{L}(\gamma), \tag{2.37}$$

with

$$\tilde{L}(\gamma) = \int_0^1 \tilde{p}(\tilde{x})\mathrm{d}\tilde{x} = \frac{1}{(1-\gamma)^2}\left(\ln(\gamma) + 2\frac{1-\gamma}{1+\gamma}\right). \tag{2.38}$$

The dimensionless load $\tilde{L}(\gamma)$ is shown as function of the downward slope in Figure 2.5 and can be interpreted as load capacity. This figure shows that there exists an optimum load bearing angle for the rigid seal. As expected, the load capacity becomes 0 when the slope γ becomes 0. Then, a maximum is reached close to a slope of 2, and further increasing the slope decreases the load capacity.

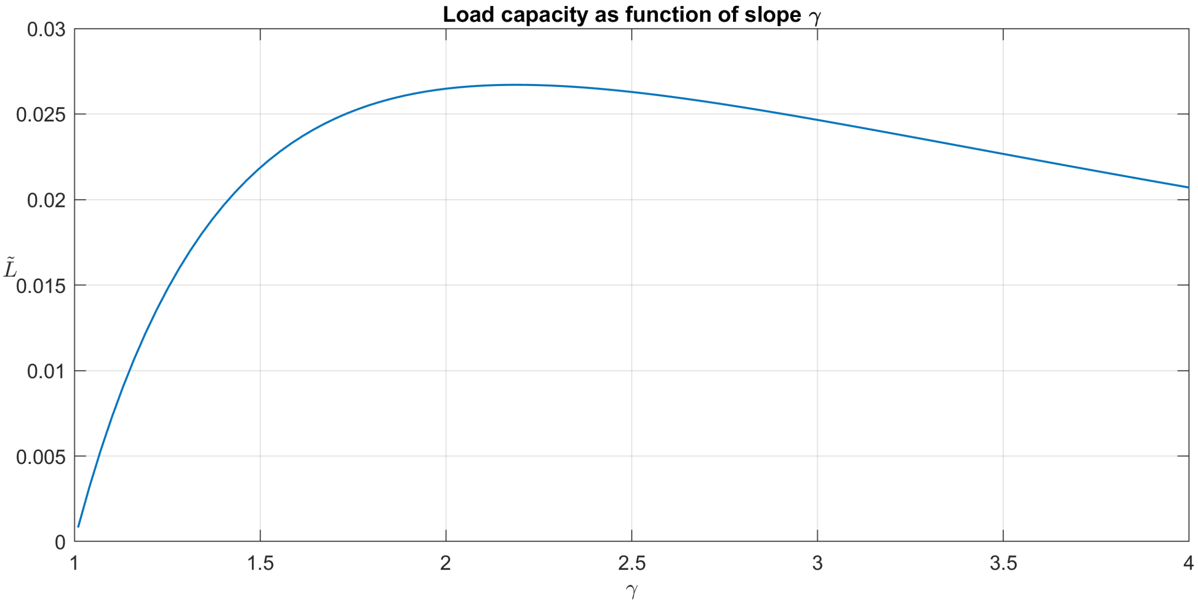

Figure 2.5: Dimensionless load acting on a rigid seal as function of slope with water as lubricant.

By differentiating the dimensionless load $\tilde{L}(\gamma)$ an optimum slope γ_{opt} can be found that maximizes the load capacity:

$$\frac{\mathrm{d}}{\mathrm{d}\gamma}\tilde{L}(\gamma) = 0 \qquad \rightarrow \qquad \gamma_{\text{opt}} = 2.2. \tag{2.39}$$

The friction force, caused by the fluids that are pushed into the gap between the seal and the moving surface, is equal to:

$$F_{\text{fric}} = \int_0^{X_0} \tau_{\text{w}}(x)\mathrm{d}x \cdot Y_0, \tag{2.40}$$

where τ_{w} is the shear stress at the moving surface ($z = 0$).

$$\tau_{\text{w}}(x) = \eta \left[\frac{\mathrm{d}u}{\mathrm{d}z}\right]_{z=0} = -\frac{1}{2}h\frac{\mathrm{d}p}{\mathrm{d}x} - \eta\frac{U_0}{h} \tag{2.41}$$

Substitution of the pressure field and integration over length X_0 gives the friction force:

$$F_{\text{fric}} = -\frac{\eta U_0 X_0 Y_0}{h_2}\left(\frac{6}{1+\gamma} + \frac{4\ln(\gamma)}{1-\gamma}\right). \tag{2.42}$$

Note that the minus sign in the equation indicates that the force acts in the opposite direction of the velocity U_0. The coefficient of friction is defined as:

$$\mu = \frac{F_{\text{fric}}}{LY_0}. \tag{2.43}$$

This also explains the origin of the lubrication coefficient λ introduced in Section 2.1.2. In case of full hydrodynamic lubrication the friction coefficient μ has a linear relation with the lubrication coefficient:

$$\mu \sim \frac{\eta U}{L} = \lambda. \tag{2.44}$$

The relation between the friction coefficient and the film ratio γ is illustrated in Figure 2.6

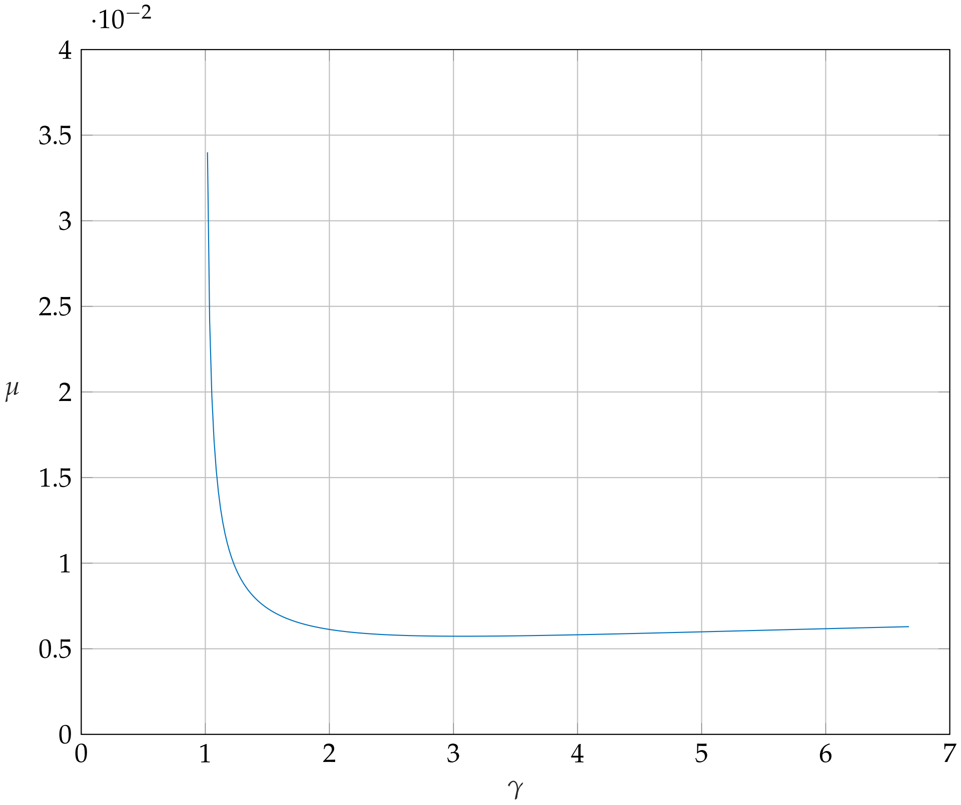

Figure 2.6: friction coefficient of a rigid seal for various inclination ratios with water as lubricant. L = 500 N, U = 1 m/s

Note that this derivation is a simplification of the actual problem. Material deformation and roughness effects have not been taken into account while they have a significant effect on the friction values [13]. The Reynolds equation is a useful equation, but it is not complete enough to predict the friction under all conditions. The aim of the next section is to find a model that closes the relation for the friction between surfaces that are not fully separated by a fluid film, but also make solid-solid contact.

2.3. Mixed and boundary lubrication

Both the mixed and boundary lubrication regime (see Figure 2.1) describe a lubricated contact in which surface roughness significantly affects the frictional behaviour of the contact. As suggested by the term "mixed", two types of interfacial stresses are present: solid-liquid and solid-solid interaction. In Section 2.2 the surfaces were assumed to be rigid and smooth. In reality, nearly all contacting surfaces possess a certain roughness and deform when enough pressure is applied [12]. The theoretical boundary between the hydrodynamic lubrication and mixed lubrication regime is represented by the roughness asperities that start to make contact. The consequence is that two surfaces can be partly separated by a fluid film and partly contacted by the highest asperities. The length scales of the asperities extend from centimeters to atomic lengths and are therefore complex to model. While hydrodynamic lubrication effects are still considerable, the friction coefficient rises and surface wear is present. The Greenwood-Williams theory models a rough surface as many micro-scale hemispheres or hemicylinders next to each other. This creates a roughness pattern that is simple to be adjusted. The first step in building this model is to define the dry contact mechanics of these hemispheres and hemicylinders.

2.3.1. Contact mechanics

A first attempt to model the contact mechanics between curved objects was done by Hertz, who developed a theory that predicts a nonlinear increase in the contact area with a linear increase in the squeezing force. Theoretically, the contact between two rigid spheres is a point and for two parallel rigid cylinders it is a line. With any load on these objects the pressure and stresses would be infinite. In reality a small contact area is created between the (curved) surfaces due to elastic deformation, which limits the stresses to a finite value. Almost all contact models approximate these stresses by applying Hertz contact theory[19]. The derivation of the Hertz contact theory is relatively complex and the reader is referred to [18] for an elaborate explanation of the theory, but since it is applied here it is necessary to describe this approach briefly. Hertz contact theory uses the following assumptions [18]:

Assumptions

14.Half-space approximation: surfaces are infinitely large half-spaces.

15. Parabolic pressure distribution: the pressure distribution in the contact is parabolic.

16. Classical theory of elasticity: small strains and homogeneous material.

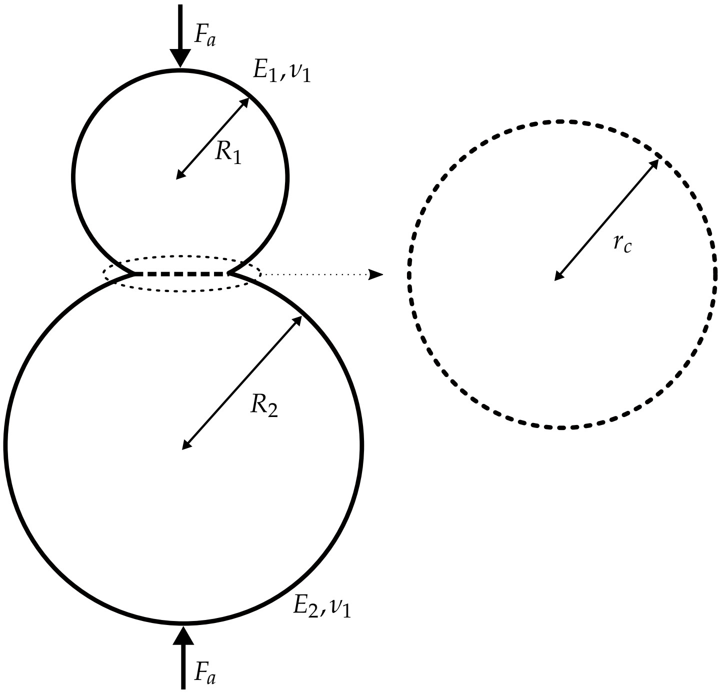

Figure 2.7: Hydrodynamic lubrication between an inclined seal and a moving surface.

Illustrated in Figure 2.7 is the case of two spheres in contact. The Hertzian contact radius of axi-symmetric spheres is:

$$r_\mathrm{c} = \sqrt[3]{\frac{3F_\mathrm{a}R'}{4E'}}. \tag{2.45}$$

where F_a is the contact force. The reduced radius R' and the reduced elasticity modulus E' are given by the following relations:

$$\frac{1}{R'} = \frac{2}{R_1} + \frac{2}{R_2} \qquad \text{and} \qquad \frac{2}{E'} = \frac{1-\nu_1^2}{E_1} + \frac{1-\nu_2^2}{E_2} \qquad . \tag{2.46}$$

With $R_{1,2}$, $E_{1,2}$ and $\nu_{1,2}$ as the axis specific asperity radii, elastic moduli and Poisson's ratios, respectively. The mean and maximum pressure are given by:

$$p_\mathrm{mean} = \frac{F_\mathrm{a}}{\pi r_c^2} \qquad \text{and} \qquad p_\mathrm{max} = \frac{2F_a}{\pi r_c^2} \qquad . \tag{2.47}$$

The pressure distribution over the Hertzian contact radius can then be calculated as a parabolic shape. Furthermore, the elastic deformation as a function of the pressure distribution is:

$$u_{\mathrm{d}}(x,y)=\frac{2\pi}{E'}\int\int\frac{p(x',y')}{\sqrt{(x-x')^2+(y-y')^2}}\mathrm{d}x'\mathrm{d}y' \tag{2.48}$$

Determining the deformation between contacting spheres can be useful in calculating the actual contact surface between rough contacts. The next step is to use this model for many hemispheres that are placed in a grid.

2.3.2. The Greenwood-Williamson roughness model

The simplest model of a rough surface consists of an array of hemispheres with equal curvature and radius. When squeezed against a flat surface or identical surface, the Hertz contact theory predicts the contact surface as a function of the load.

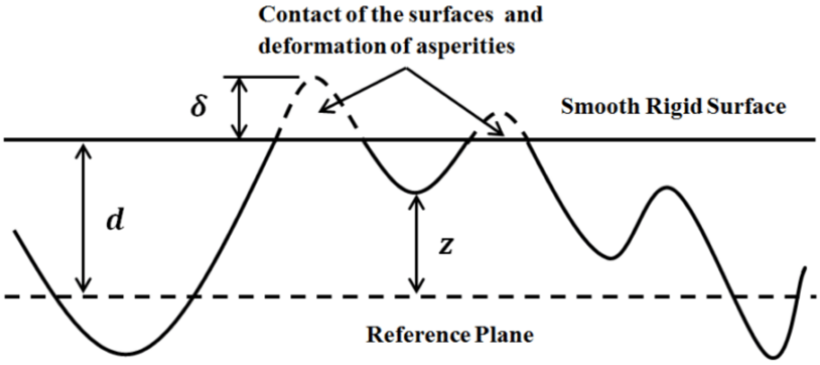

Figure 2.8: The Greenwood and Williamson Contact Model for the contact between a smooth rigid plane and rough elastic surface [30].

Shown in Figure 2.8 is a more sophisticated multi-asperity contact model, developed by Greenwood and Williamson [12], in which a rough surface is represented by a set of independent asperities with spherical tips of constant radius. For each asperity Hertz contact theory is applicable and thus the vertical deformation $u_{\mathrm{d}}(x,y)$ can be determined. The main assumption in Greenwood and Williamson's theory is that asperity heights are randomly varied with a certain probability distribution. Following the theory, a Gaussian distribution is chosen, which is formulated as:

$$\Phi_{\mathrm{G}}(z)=\frac{1}{\sigma_s\sqrt{2\pi}}e^{-z^2/(2\sigma_s^2)}. \tag{2.49}$$

Where σ_s is the standard deviation of the asperity peak height.

Assumptions

17.Randomly varied asperity heights: The asperity heights are randomly varied with a probability density function.

The distance d between two surfaces is generally taken as the spacing between the average height of the asperities on both sides. The probability of contact between asperities then becomes:

$$\mathcal{P}(z\geq d)=\int_d^\infty \Phi_{\mathrm{G}}(z)\mathrm{d}z. \tag{2.50}$$

Subsequently, the number of asperities N should be statistically large enough to calculate the expected number n of asperities that make contacts:

$$n = N\mathcal{P}(z \geq d) = N\int_d^\infty \Phi_\mathrm{G}(z)\mathrm{d}z \tag{2.51}$$

According to Hertz contact theory, the area of contact a for the asperity with height z and curvature β equals

$$a = \pi\beta\delta = \pi\beta(z-d). \tag{2.52}$$

The total predicted area of contact is:

$$A_r = aN\mathcal{P}(z \geq d) = \pi\beta N\int_d^\infty (z-d)\Phi(z)\mathrm{d}z. \tag{2.53}$$

Greenwood and Williamson then derived the total load as [12]:

$$F_\mathrm{a} = \frac{2}{3}\sqrt{\beta}NE'\int_d^\infty (z-d)^{3/2}\Phi(z)\mathrm{d}z. \tag{2.54}$$

Where F_c is the asperity contact force. The remaining unknown is the film thickness between both surfaces. Since the surfaces are parallel during contact in the mixed lubrication regime, the film thickness can not be predicted by the Reynolds equation. The total load is carried by both the fluid and the asperities that are in contact. This relation can be defined by the shared load principle.

2.3.3. Shared load principle

Johnson's shared load model defines the normal force on the contact as the combined contact force and fluid generated force [18]:

$$F_n = F_c + F_h \tag{2.55}$$

Based on equation 2.55, two coefficients can be defined:

$$\Gamma_1 = \frac{F_n}{F_h}, \qquad \Gamma_2 = \frac{F_n}{F_c} \tag{2.56}$$

which are mutually dependent through:

$$\Gamma_1 + \Gamma_2 = 1. \tag{2.57}$$

At the first step of the simulation procedure a guess must be given for the Γ_1 variable. The simulations have been generally been stable with $\Gamma_1 = 20$ as starting point.

2.3.4. Moes film thickness

To simplify the film thickness prediction in the mixed lubrication regime, Moes [23] derived a function fit in which three main dimensionless numbers were used. The first is the dimensionless film thickness H:

$$H = \frac{h}{R}\left(\frac{\eta U}{E'R}\right)^{-\frac{1}{2}}, \tag{2.58}$$

the second one is the dimensionless load number M:

$$M = \frac{F_n}{BE'R}\left(\frac{\eta U}{E'R}\right)^{-\frac{1}{2}}, \tag{2.59}$$

and the third one is the dimensionless lubricant number:

$$L = \alpha E'\left(\frac{\eta U}{E'R}\right)^{\frac{1}{4}}. \tag{2.60}$$

and R$'$ is the reduced radius, η the lubricant viscosity, F_n the normal force and α the Barus viscosity-pressure coefficient of the lubricant. The function fit derived by Moes is formulated as:

$$H_C = \left[\Gamma_1^s \left(H_{RI}^{\frac{7}{3}} + \Gamma_1^{-\frac{14}{15}} H_{EI}^{\frac{7}{3}}\right)^{\frac{3}{7}s} + \left(H_{RP}^{-\frac{7}{2}} + H_{EP}^{-\frac{7}{2}}\right)^{-\frac{2}{7}s}\right]^{-s}, \tag{2.61}$$

with auxiliary variable s:

$$s = \frac{1}{5}\left(7 + 8e^{-2\frac{H_{EI}}{H_{RI}}\Gamma_1^{-\frac{2}{5}}}\right). \tag{2.62}$$

This formulation uses expressions for film thicknesses in four distinctive regimes: Rigid-Isoviscous (RI), Rigid-Piezoviscous (RP), Elasto-Isoviscous (EI) and Elasto-Piezoviscous (EP). The definition of theses parameters reads:

$$H_{RI} = 3M^{-1} \tag{2.63}$$

$$H_{RP} = 1.287L^{\frac{2}{3}} \tag{2.64}$$

$$H_{EI} = 2.621M^{-\frac{1}{5}} \tag{2.65}$$

$$H_{EP} = 1.311M^{-\frac{1}{8}}L^{\frac{3}{4}} \tag{2.66}$$

The metric film thickness is obtained by rewriting the dimensionless film thickness from Equation 2.61 with Equation 2.58:

$$h_m = H_C R\left(\frac{\eta U}{E'R}\right)^{\frac{1}{2}} \tag{2.67}$$

This formulation of the film thickness is a replacement for the hydrodynamic component of the Reynolds equation. The fluid flow between both surfaces is parallel in the mixed lubrication regime, which will cancel the pressure term in the Reynolds equation and lead to a fluid film thickness of zero. In reality the film thickness is also related to the surface roughness and the load. The Moes formulation is therefore used to generate a film thickness that relates to the roughness. When the film thickness is determined for a particular case, the Reynolds equation will then be used to determine the hydrodynamic shear stress on the surfaces.

In some special cases it can happen that the film thickness definition by Moes turns negative. For stability reasons Johnson's definition of the film thickness h_j is used [18]. The film thickness is defined as the average fluid volume between the two rough surfaces divided by the nominal contact area:

$$h_j = \int_{-\infty}^{h_m} (h_m - s)\Phi(s)\,\mathrm{d}s. \tag{2.68}$$

Here s is a dummy variable. The lower bound $-\infty$ is typically taken as $-8\sigma_s$ in simulations.

2.3.5. Solution procedure

In order to calculate the coefficient of friction for a mixed lubricated contact, the part of the load carried by the fluid and the asperities must be determined. Figure 2.9 shows the steps taken in the solution procedure. The main purpose of this scheme is to obtain the right Γ_1 and Γ_2. The first guess of Γ_1 is used to calculate the film thickness and force carried by the asperities. This force is then compared to the contact force given by Γ_2:

$$F_c = \frac{F_n}{\Gamma_2}. \tag{2.69}$$

If the forces are not equal a minimization algorithm will provide a new guess for Γ_1 to minimize $|F_a - F_c|$. When the difference between F_a and F_c is small enough the shear stress exerted by the lubricant can be determined. The Reynolds equation solution derived in Section 2.29 gave expressions for the pressure and shear stress between the surfaces. For parallel surfaces, the slope γ becomes 1 and the pressure goes to zero in the Reynolds equation:

$$\tilde{p}(\tilde{x},\gamma) = \frac{\gamma}{1-\gamma^2}\left(\frac{1}{\tilde{h}(\tilde{x},\gamma)^2} - \frac{1}{\gamma^2}\right) - \frac{1}{1-\gamma}\left(\frac{1}{\tilde{h}(\tilde{x},\gamma)} - \frac{1}{\gamma}\right), \tilde{p}(\tilde{x},0) = 0 \tag{2.70}$$

Note that $\tilde{h} = h/h_2 = 1$ for all $\tilde{x}$ when the contact surfaces are parallel. The absence of pressure generation causes the expression for shear stress in equation 2.41 to lose its pressure term:

$$\tau_\mathrm{w}(x) = -\eta\frac{U_0}{h} \tag{2.71}$$

This simple expression is shear stress in Couette flow problems. The friction coefficient can then be calculated by:

$$\mu = \frac{F_f}{F_n} = \frac{\mu_0 * F_C + \tau_w A_h}{F_n}. \tag{2.72}$$

Note that A_h can be calculated using Equation 2.53 and:

$$A_h = A_n - A_r \tag{2.73}$$

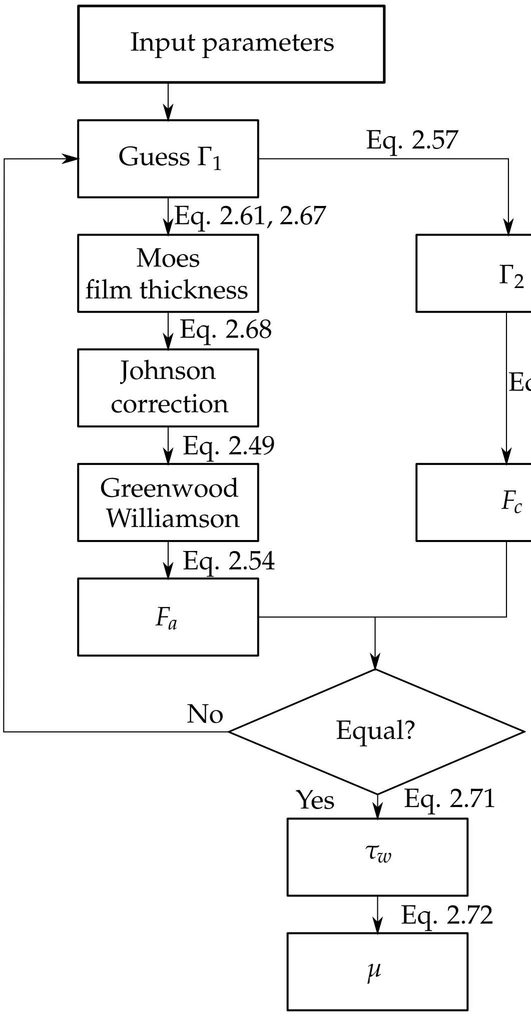
Input parameters
Guess Γ_1
Eq. 2.57
Eq. 2.61, 2.67
Moes film thickness
Γ_2
Eq. 2.68
Johnson correction
Eq. 2.69
Eq. 2.49
Greenwood Williamson
F_c
Eq. 2.54
F_a
No
Equal?
Yes
Eq. 2.71
τ_w
Eq. 2.72
μ

Figure 2.9: Flow diagram of the solution procedure.

2.3.6. Model results

The results in this section are generated Stribeck curves and a sensitivity analysis of some of the input variables. An example of typical input parameters that relate to the experimental conditions is included in the following table:

Property	Value	Unit	Description
n	$1 \cdot 10^9$	m^{-2}	Asperities per square meter
β	$1 \cdot 10^{-}4$	m	Asperity radius
σ_s	$2.5 \cdot 10^{-}6$	m	Standard deviation of the asperity height
B	0.02	m	Contact length
E'	$2.6 \cdot 10^6$	GPa	Reduced elasticity modulus
η	$1 \cdot 10^{-}3$	Pa·s	Viscosity
α	$2 \cdot 10^{-}8$	Pa^{-1}	Barus viscosity pressure coefficient
μ_0	1.2	-	Friction in Boundary Lubrication regime
F_N	10	N	Normal force

Figure 2.10 shows a Stribeck curve as function of the lubrication coefficient for three normal forces. The three main lubrication regimes are clearly visible. The boundary lubrication regime, in which the load is solely carried by the asperities, ranges from 10^{-8} to 10^{-6}. The mixed lubrication regime, in which the load is both carried by asperity and fluid pressure, ranges from 10^{-6} to $2 \cdot 10^{-5}$ for the 20 N load case and to $4 \cdot 10^{-5}$ for the 5 N load case. The hydrodynamic lubrication regime, in which the load is carried by the fluid, then continues the curve in an approximately linear relation with the lubrication coefficient.

As clearly visible in Figure 2.10, both the mixed lubrication regime and the hydrodynamic lubrication regime are heavily influenced by the wall normal force. With increasing wall normal force, the friction coefficient transitions to the mixed lubrication regime at a lower lubrication coefficient and reaches a lower minimum friction coefficient. Also, the curve continues in a linear way in the hydrodynamic lubrication regime at a lower friction coefficient.

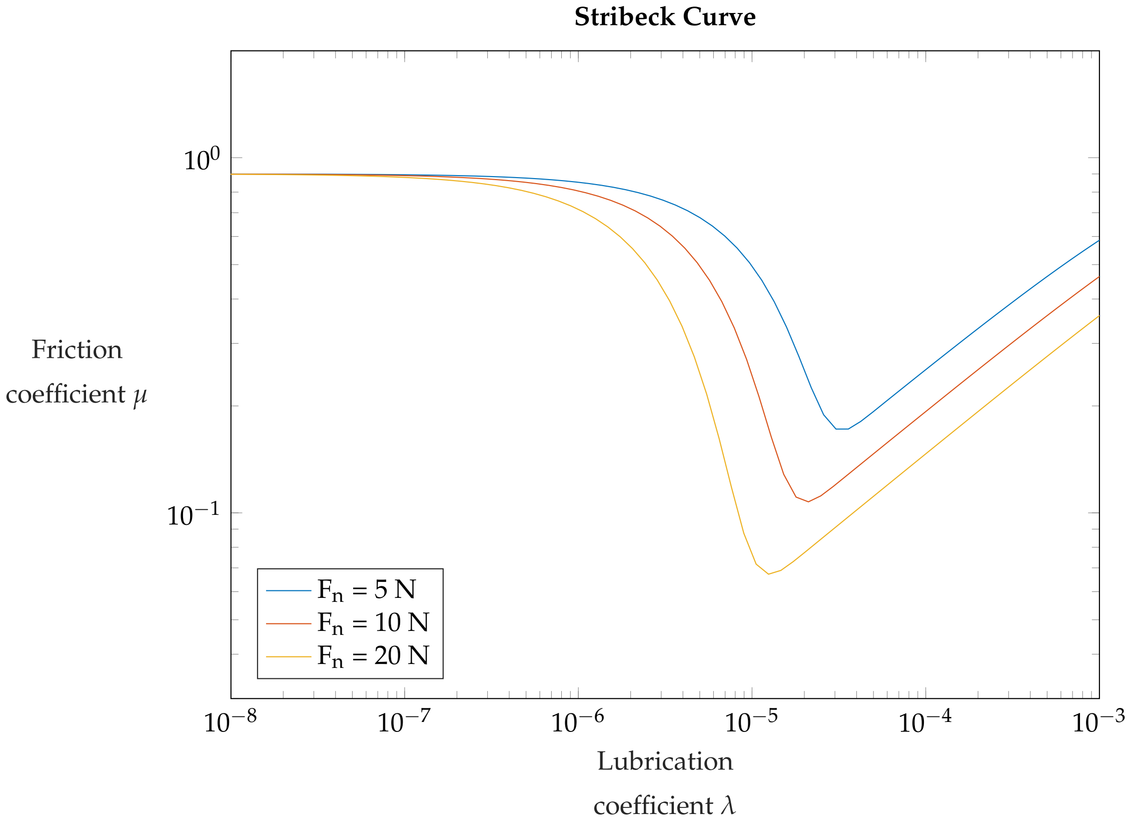

Figure 2.10: Stribeck curves with varying normal force F_n (5, 10 and 20 N).

Figure 2.11 shows the effect of varying the friction coefficient in the boundary lubrication regime on the Stribeck curve. This variation has a strong influence on the curve in the mixed lubrication regime, which has a lower friction coefficient when the friction coefficient in the boundary layer is decreased. The hydrodynamic lubrication regime is then shared between all three friction curves from the start.

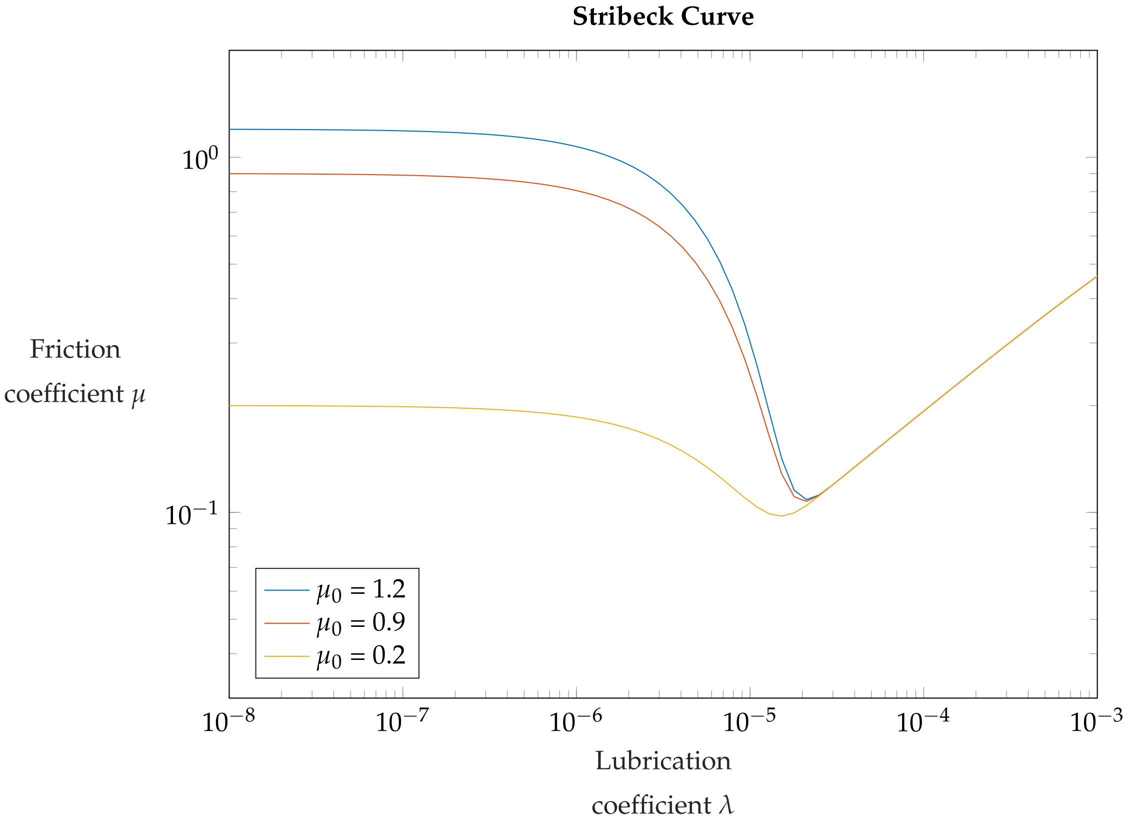

Figure 2.11: Stribeck curves with varying the friction coefficient in the boundary lubrication regime μ_0.

Figure 2.12 shows the effect of varying the statistical roughness parameters β and n on the Stribeck curve. The parameters $n\beta\sigma_s$ influence the roughness of the contact surface, while the product is held constant. decreasing the asperity radius and increasing the amount of asperities per square meter leads to a delay of transition to the mixed lubrication regime. A lower asperity radius and more asperities per square meter will lead to a smoother surface which will extend the boundary lubrication regime. The strongest shift of the curve is in the mixed lubrication regime, where the transition to the hydrodynamic lubrication regime is delayed with decreasing asperity radius.

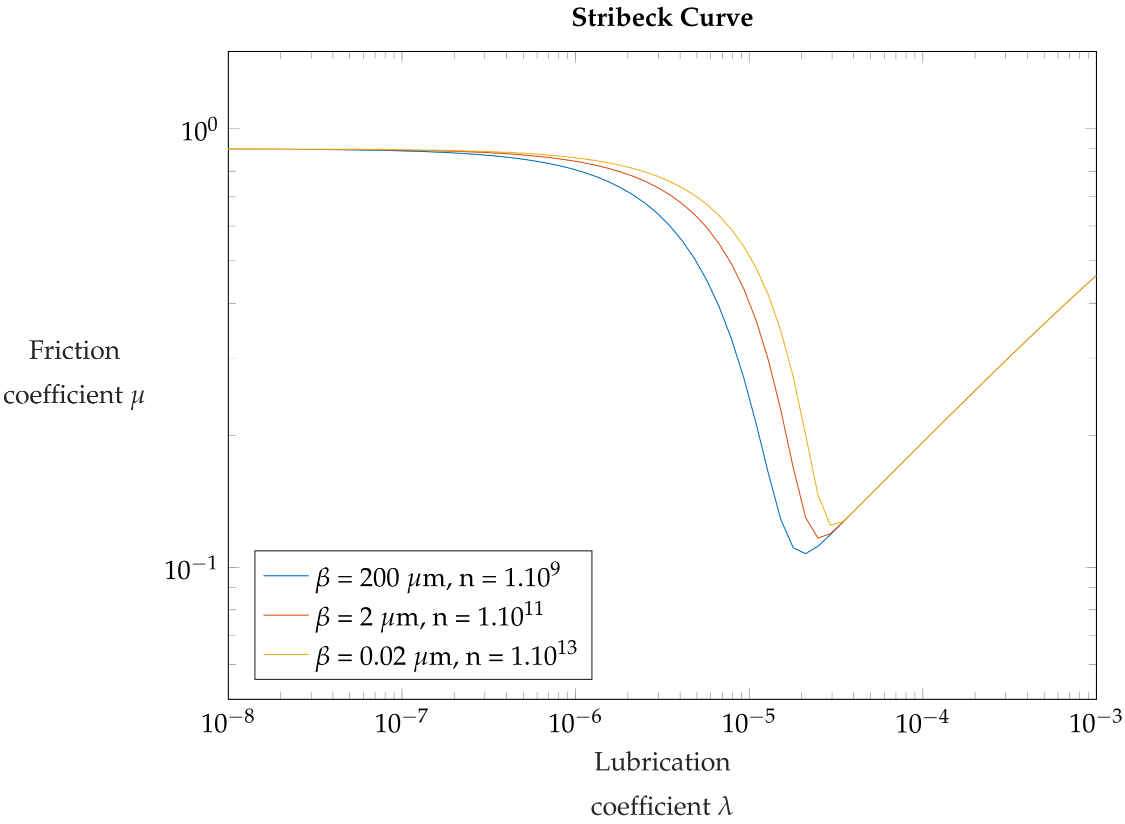

Figure 2.12: Stribeck curves with varying statistical roughness parameters β and n.

Figure 2.13 shows the effect of varying the statistical roughness parameters σ_s and n on the Stribeck curve. Decreasing the standard deviation of the asperity height and increasing the amount of asperities per square meter proportionally, leads to an early transition from the boundary lubrication regime to the mixed lubrication regime. Also, the friction coefficient dives to a lower minimum with an early transition to the hydrodynamic lubrication regime. The three curves then assemble consecutively into the same linear curve.

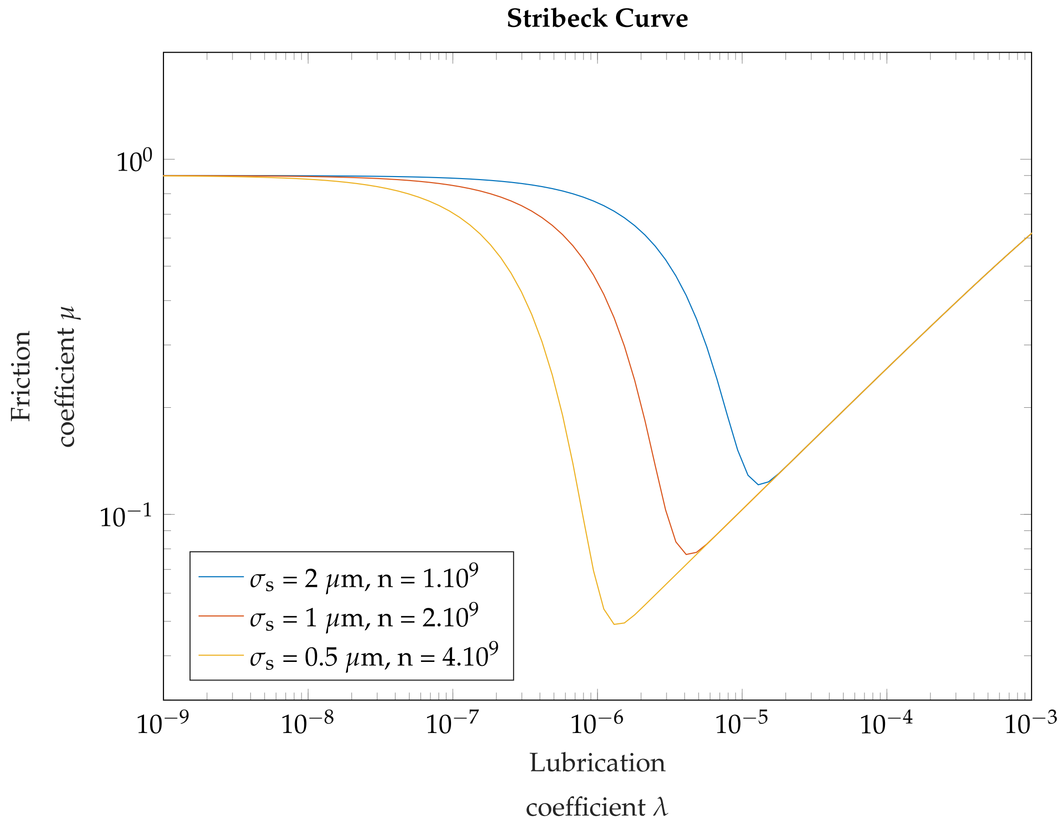

Figure 2.13: Stribeck curves with varying statistical roughness parameters σ_s and n.

2.4. Wear

Wear is the damage or removal of solid material. While wear also occurs during mixed lubrication, it is more apparent in the boundary lubrication regime. The gap between the contacting surfaces has become very small in this regime, which could result in excessive wear. On the contrary, a pig that is fitted too loosely will also wear due to nose dive [32]. Sealing discs are made of poly-urethane, which is a good material for securing tight seals due to its high visco-elasticity, but prone to plastic deformation and wear (see Figure 2.14). As the sealing discs wear during a pig run, the seals will eventually fail to prevent leakage and both the pressure difference across the pig and the efficiency will drop. This particularly occurs when pigs travel over longer distances.

Zhang *et al.* [32] carried out an experimental study on sliding PU samples against steel pipeline materials. The modes of wear that occur during the experiment were investigated by using a microscope and FEM. Observations confirmed that abrasion was the primary wear mode next to corrosion and surface fatigue. This resulted in layered patterns on the surface of the rubber sample. After long term cyclic stress, fatigue damage flattens out the patterns again. At the same time abrasion continues to impair the material by creating grooves. Modelling this behaviour could aid in the future design of pigs and prevent the sealing discs from failing.

Many models have been developed for mechanical wear. Huq and Celis[16] derived 182 equations for different types of wear. While these equations give results that agree nicely with the specific cases they are designed for, no unified fundamental wear theory is established so far. The extensive empirical list of models that can be found in the literature falls outside the scope of this report. A simple approach to modelling wear will be pursued: the Archard model. This model is designed for adhesive wear and assumes spherical asperities deform plastically during contact. Just as with Hertzian mechanics the contact area is circular and equals πr_c^2, with r_c as the radius of the circle. Assumed is that the mean contact pressure is equal to the hardness H of the softer material:

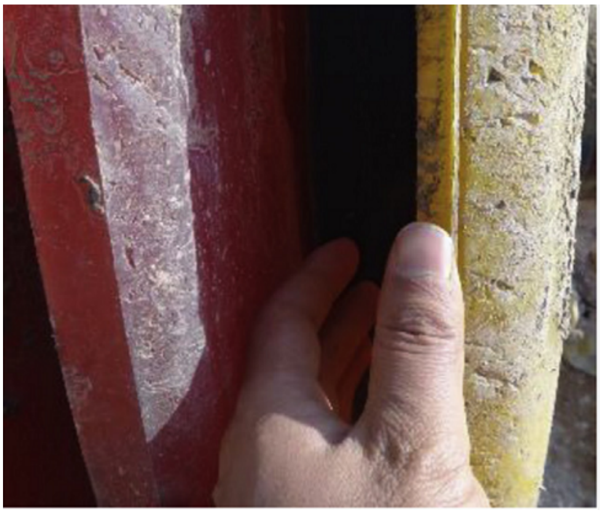

Figure 2.14: Worn sealing and guiding discs of a pig [32].

$$H = \frac{F_c}{\pi r_c^2}. \tag{2.74}$$

With F_c as the contact force. After sliding a distance of $2r_c$ there is a probability of K that debris will form. If debris is formed, the shape is assumed to be hemispherical with radius r. Then the volume of the debris particle equals $\frac{2}{3}\pi r_c^3$. The wear volume per sliding width $2r_c$ becomes:

$$V = \frac{\frac{2}{3}K\pi r_c^3}{2r_c} = \frac{1}{3}K\pi r_c^2. \tag{2.75}$$

As $\pi r_c^2 = F_c/H$ and introducing $k = K/3$, the Archard equation becomes:

$$W_d = \frac{kF_c s}{H}. \tag{2.76}$$

In which W_d is the total volume of wear debris that is produced, k is the wear coefficient and s is the sliding distance. The quantity k is frequently used to compare the wear resistance of different materials [31]. The value of the wear coefficient should be estimated experimentally. Although the Archard equation was developed for adhesion wear, it is also commonly used for abrasion and other types of wear.

Applying the Archard equation on a local scale in friction models can provide insight in the evolution of surface roughness as a result of wear. Dividing the volume of debris W with the surface A gives the local wear depth:

$$\frac{W}{A} = h_w = \frac{kPs}{H}. \tag{2.77}$$

With P as the local contact pressure. By differentiating the wear depth in time the equation takes the following form:

$$\frac{\partial h}{\partial t} = \frac{kpU_0}{H}. \tag{2.78}$$

Here U is the sliding velocity of the contacting surfaces. This equation can be implemented in a friction model to track the development of grooves in sliding surfaces.

2.5. Wall force modelling

It was shown in the previous sections that the friction force is strongly related to the force normal to the wall. Unfortunately, this force is not simple to derive from the sealing disc dimensions. This section will explain the hyperelastic model that was chosen to determine the wall-normal force. This model was used in an axi-symmetric configuration to simulate the confinement in a pipeline, but also in a 2D configuration to investigate the deformation on a rectangular rubber lip.

2.5.1. Mooney-Rivlin model

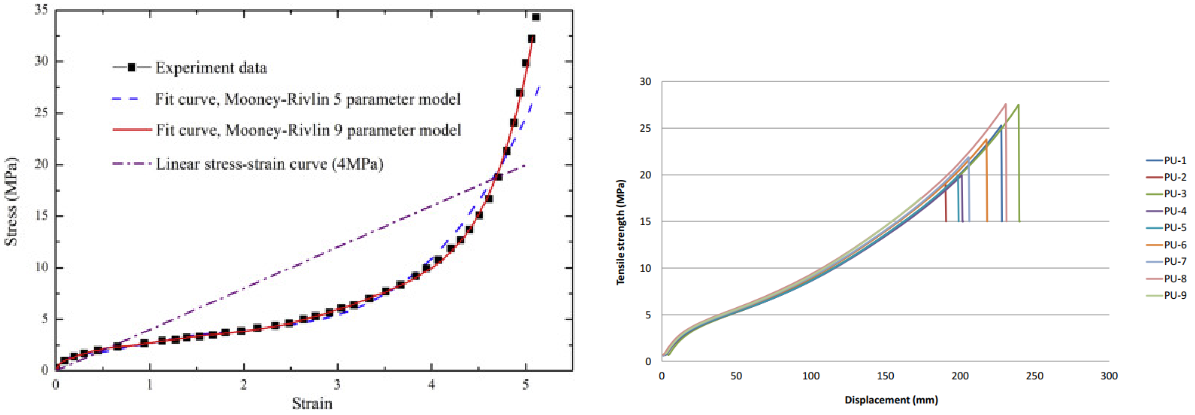

(a) Stress-strain curves by Zhu *et al.* fitted with linear theory and hyperelastic Mooney-Rivlin models [35].

(b) Stress-strain curves measured by Den Heijer for 9 dog bones cut from sealing discs[9].

Figure 2.15: Two stress-strain curves measured by universal testing machines.

In the studies conducted by Graafland [11] and Den Heijer [9] an analytical model and a linear finite element method (FEM) model were used to investigate the wall force. While their results showed a good level of agreement with the experimental data, the accuracy might improve by using nonlinear models. Zhu *et al.* [35] investigated the use of a hyperelastic 5-parameter and 9-parameter Mooney-Rivlin (MR) model. They measured the stress-strain curves of poly-urethane pig seals with a universal testing machine and fitted them to the models (see Figure 2.15a). Their analysis showed that the stress-strain curve of poly-urethane was not linear. This also corresponds to the results that Den Heijer obtained from tensile stress tests on poly-urethane dog bones shown in Figure 2.15b. Note that the shape of the curve, in the range of 0 to 50% strain, has the shape of a second-order root function. This means that the stress-strain curve can also be fitted with a two-parameter MR model if used for strains less than 50%. The two-parameter MR model will therefore be investigated in the present study as a fit for the stress-strain data measured by Graafland [11].

The Mooney-Rivlin class of models expresses the mechanical strain energy as a sum of invariants I_1,I_2 and I_3 of the Cauchy stress tensor:

$$W = \sum_i \sum_j C_{ij}(I_1-3)^i(I_2-3)^j + D(J-1)^2 \tag{2.79}$$

where C_{ij} and D are constants that are determined by curve fitting experimental tests. The first few terms of the series are:

$$W = C_{10}(I_1-3) + C_{01}(I_2-3) + C_{11}(I_1-3)(I_2-3) + C_{20}(I_1-3)^2 + \cdots + D(J-1)^2, \tag{2.80}$$

which is the five-parameter model. The two-parameter model only uses C_{10} and C_{01}. The relationship between the uniaxial stress σ and resulting extension of a MR material is:

$$\sigma(\lambda) = 2\left(C_{10} + \frac{C_{01}}{\lambda}\right)\left(\lambda - \frac{1}{\lambda}\right), \tag{2.81}$$

in which λ_i is the relative elongation:

$$\lambda_i = \frac{L_0 + \Delta L_i}{L_0}. \tag{2.82}$$

The coefficients are then determined by minimizing the total squared error:

$$e = \sum_{i=1}^{N} (\sigma(\lambda_i) - \sigma_i)^2. \tag{2.83}$$

Here σ_i is the experimentally determined stress.

Figure 2.16a shows the stress-strain data obtained from a sealing disc sample in the universal testing machine. These data are fitted with the two-parameter MR model and linear strain theory.

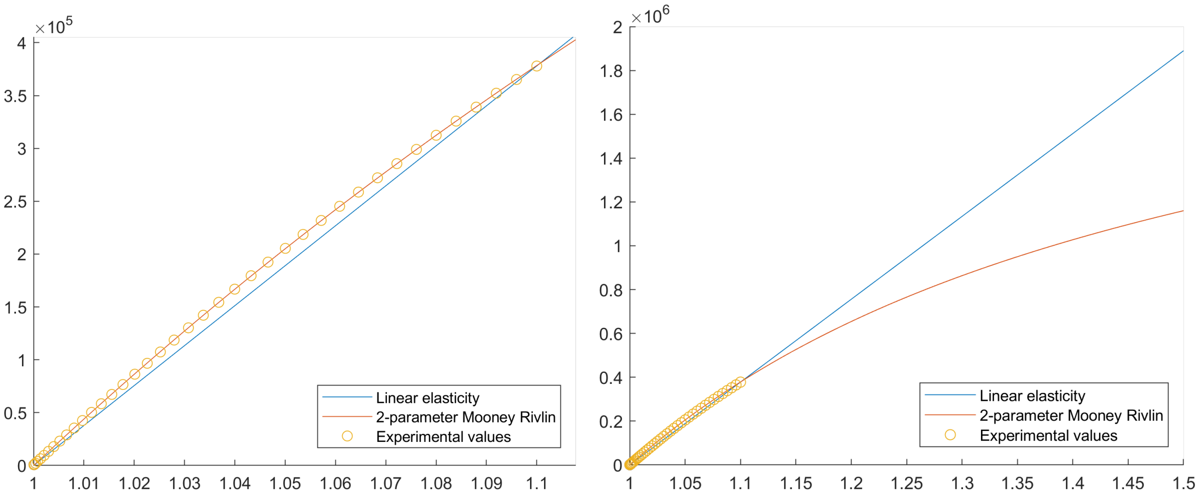

(a) Experimental range curve fit.

(b) Stress-strain curves model comparison for larger strains.

Figure 2.16: Experimentally obtained stress-strain data fitted with the two-parameter Mooney-Rivlin model and linear strain theory.

In figure 2.16a, it seems that the linear elasticity model almost coincides with the two-parameter MR model. However, the slight arc in the experimentally obtained data predicts the curve for larger strains shown in Figure 2.16b. Since sealing disc deformation can lead to strains up to 20% [9], the two-parameter MR model will be used in the FEM implementation.

2.5.2. Model results

Implementation of the two-parameter MR model was done in COMSOL Multiphysics. A geometric model with axi-symmetric properties resulted the highest robustness of the simulation and was therefore the best option. As shown in Figure 2.17, a rubber disc was confined in a circular steel clamp. This approach simulates the bolted clamp in the most realistic way. The rubber disc is held in the cavity

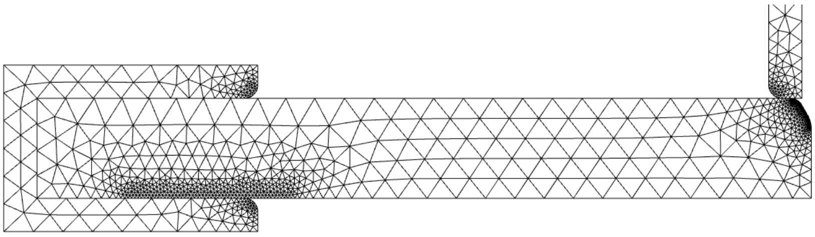

Figure 2.17: Mesh plot of the sealing disc confinement model for 2% oversize.

of the clamp purely by contact mechanics. No roller or fixed boundary conditions were used in this model. The third element is the pipeline wall which is slowly sliding downward, while the steel clamp is held static. Notice that the mesh density is not uniform. High stresses occur in the lower clamped region of the rubber disc that suffice a higher mesh density for a fully converged solution. Also, the high mesh density in the contact region was necessary to maintain continuity. This region deforms rapidly during the simulation, which can cause the simulation to fail when too few contact nodes are available. Table 2.1 shows the configuration parameters that were used in the model.

Parameter	Value	Unit	Description
D_o	0.32	m	Outer diameter of the rubber disc without oversize
D_i	0.10	m	Inner diameter of the rubber disc without oversize
Th	15	mm	Thickness of the rubber disc
C_w	4	mm	Chamfer width
α_d	45	deg	Chamfer angle
κ	9	MPa	Bulk modulus of the rubber material
C_1	0.8314	MPa	First Mooney-Rivlin parameter
C_2	1.765	MPa	Second Mooney-Rivlin Parameter
OS	1-4	%	Sealing disc oversizes

Table 2.1: Configuration parameters used in the COMSOL simulation of sealing disc confinement.

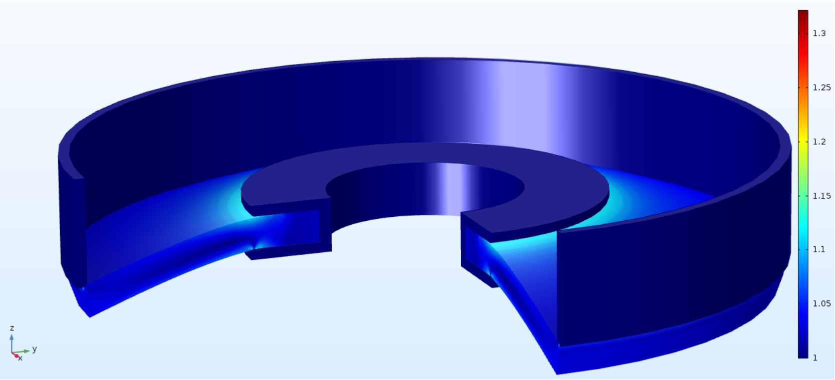

Figure 2.18: Stretch of a sealing disc during confinement in a pipeline.

Figure 2.18 shows the peak stretch during the sealing disc confinement simulation. Intuitively it may be expected that the highest strains occur when the sealing disc is fully confined in the pipeline. However, before the confinement the rubber is solely in forced contact in the axial direction. This causes the rubber to reach a peak stretch of 1.35. This translates to an elongation of the poly-urethane of 35%. This confirms the assumption that the elongation will remain under 50%, but exceeds the 20% predicted in the literature [9].

Figure 2.19a shows the strain during the confinement of the modelled sealing disc into a pipeline. The figure compares the behaviour between the deployment of linear elements, nonlinear MR elements and guided nonlinear MR elements. The MR elements can couple the strains and forces of the sealing disc during confinement, until a certain moment when they fail. This behaviour only occurs at higher oversizes, after a large spike in the strain density. This spike is shown for all three simulation methods once the sliding distance is approximately 28 mm. This is just before complete confinement is reached and the sealing discs experience a decrease in axial force. For this particular phenomenon, a guided simulation was used to investigate full confinement of the sealing disc with MR elements. Guidance was added by pulling the sealing disc backwards and adding damping to the contact mechanics. The regular MR simulaion can still be used to investigate the confinement process until failure for the higher oversizes. The complete confined state is important to determine the strain and wall force when steady state is reached.

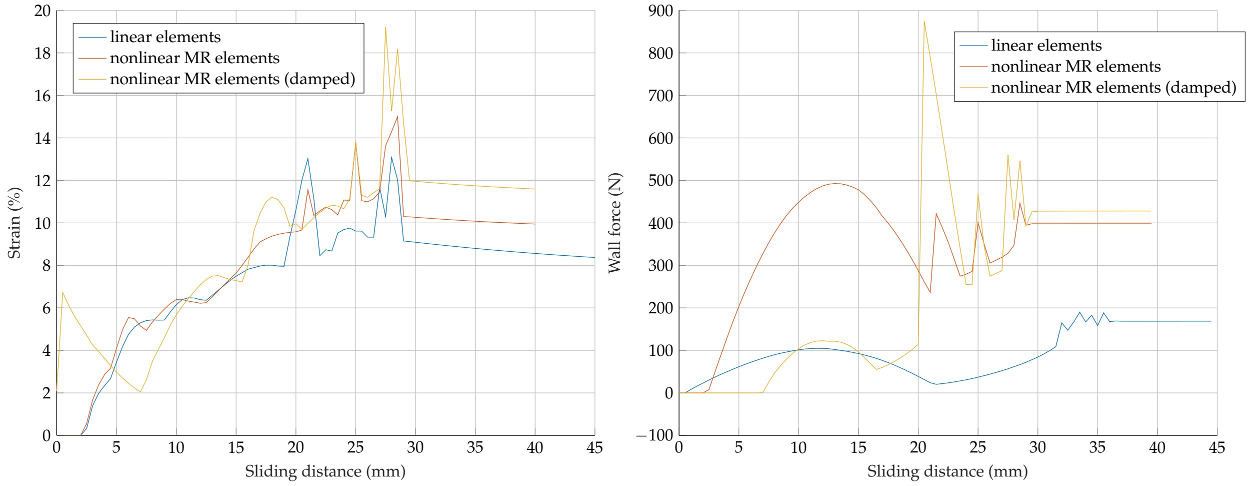

(a) Strain

(b) Wall force.

Figure 2.19: Strain and wall force during the confinement of a modelled sealing disc into a pipeline with 1% oversize.

Figure 2.19a shows the development of strain during the confinement simulation of the sealing disc. The strain of all three simulation methods end up at a different steady state value. The damped MR simulation has the highest end strain and the linear simulation ends in the lowest strain. Linearization of the strain density could be the source of this. Figure 2.19b shows the the difference in wall force buildup for an oversize of 1%. Note the difference in the first 20 mm of the linear and the MR simulation. Both simulations show a parabola shaped curve, but the peak of the MR simulation is much higher and steeper. The damped MR simulation shows the guidance over the first 7 mm where the sealing disc-pipeline contact is still not established. After that a similar parabola is drawn by the wall force, but much lower than the regular MR simulation. After that some high peaks occur in the MR and guided MR simulations. Looking between these peaks the wall force seems to follow a more smoothened transition to the steady state. Similar to the linear simulation but interupted.

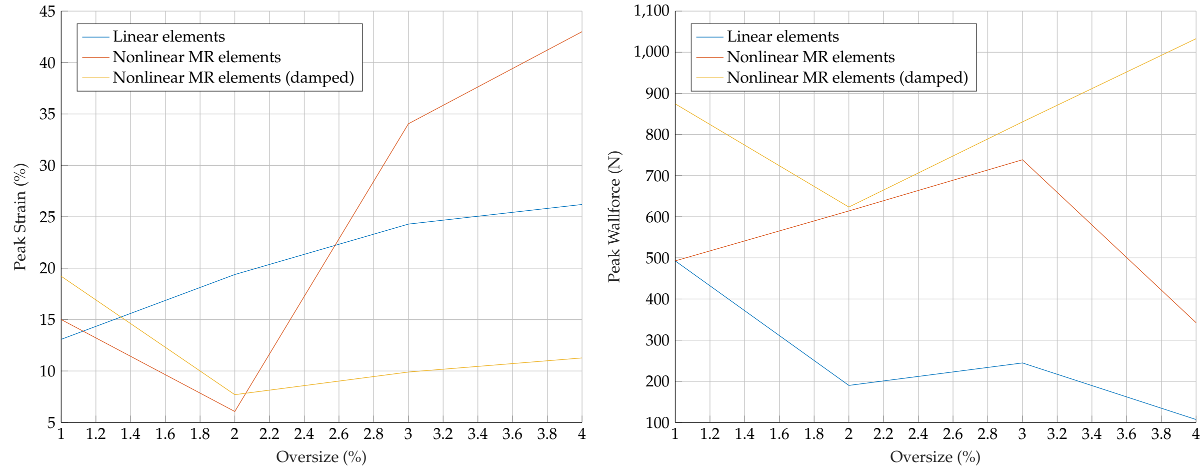

(a) Strain.

(b) Wall force.

Figure 2.20: Peak values for the strain and wall force during sealing disc confinement as function of the oversize.

Figure 2.20a shows the peak strain for oversizes between 1 and 4 percent. The peak strain shows an almost linear increase in strain as function of the oversize for the linear simulation. The MR and guided MR simulation show unexpected behaviour by having a higher peak strain for the 1% oversize sealing disc. This could be explained by a a slight difference in confinement in the pipeline. The 1% oversized disc started the simulation with contact between the inner edge of the pipeline wall and the upper edge of the sealing disc. This could increase the wall force through a slight buckling motion.

However, this was not observable in the confinement animation of the simulation. Figure 2.20b shows the peak wall force for oversizes between 1 and 4 percent. These curves show significant different patterns. The linear simulation has a negative relation with its peak strain. The relation between the MR strain and wall force is incoherent. The relation between strain and wall force of the guided MR simulation is postive and similar to the peak strain curve.

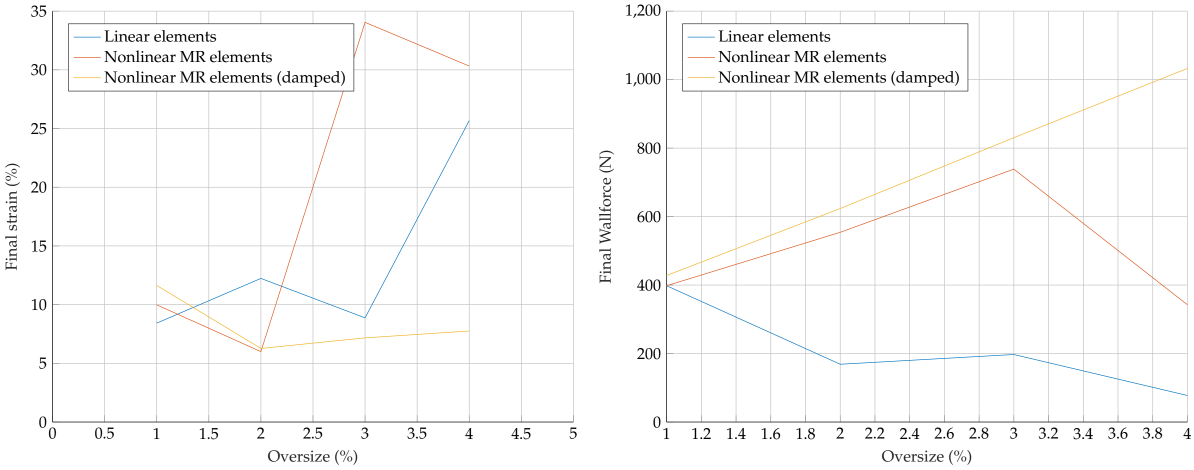

(a) Strain.

(b) Wall force.

Figure 2.21: Final stable values for the strain and wall force during sealing disc confinement as function of the oversize.

Figure 2.21a shows the final strain that is reached in the confinement simulation. Note that both the linear and MR simulations converged to extreme values and could not establish a steady state. The spike in strain, which is denoted in Figure 2.19a, causes instability at higher oversizes. This makes the results for the MR and linear simulations incoherent and inconsistent with literature. For this specific reason an extra damped MR simulation was performed. This damped MR simulation shows a more stable and linear increase in wall force as a function of the oversize (see Figure 2.21b).

3

Experiments

During this study a new experimental set-up was created to investigate the effects of lubrication on friction. This chapter elaborates on the new facility that was used to examine the micro channel flow characteristics between rubber-metal contacts.

First, the scaling approach from field operations to experiments will be explained. The Hersey number derived in Section 2.2 will be used to scale the operational conditions to experimental conditions and the limits of the lab equipment. The built facility and its components will then be reviewed. The consecutive sections will present the methodology behind the experiments and the processing of the obtained data.

3.1. Approach

3.1.1. Experimental scaling

By performing lab scale experiments it is possible to study lubrication with a focus on pigging applications. The effort and costs of a full-scale friction measurement during a pigging operation in the field make a good reason to avoid field trials. A possible solution to obtain information about the frictional mechanisms without the need of a kilometres long flow loop is experimental scaling. By choosing relevant dimensionless parameters the operational conditions can be scaled down to make the investigation of the pig friction simpler.

Section 2.1.2 showed that the friction force relies heavily on the lubrication regime that pigs operate in. These regimes can be depicted in a friction map to visualize the effects of the relevant parameters. The Hersey number indicates the degree of lubrication between sliding surfaces and is therefore also a measure for the friction itself. This makes the number suitable for downscaling the frictional behaviour of pigs in pipelines to lab experiments. The Hersey number is expressed by:

$$\lambda = \frac{\eta U}{L}. \tag{3.1}$$

Here η, U and L are the lubricant viscosity, velocity and load, respectively.

The next step is to establish a range for λ which corresponds to pig runs in the field. This range needs to be replicated in the experiments to emulate the same frictional behaviour. Each of the input parameters of the Hersey number will be shortly discussed to find the parameter range that occurs in common pigging scenarios.

3.1.2. Pigging conditions

There are four scenarios that could occur during a pig run or part of a pig run considering the lubricant viscosity:

- The pig is solely lubricated by dry natural gas. Using field data from the Marlin gas-condensate pipeline in Australia, the gas has a viscosity of 0.014 cP or $1.4 \cdot 10^{-5}$ Pa·s [15].
- The sealing discs of the pig are fully immersed with condensate. Using the same data from the Marlin field the viscosity of the gas-condensate is 0.12 cP or $1.2 \cdot 10^{-4}$ Pa·s [15].
- The pig is used to de-water the pipeline and is fully lubricated by it. The viscosity of water is then $1 \cdot 10^{-3}$ Pa·s
- Lubrication by an emulsion of water, condensate and waxy deposits which relates to high effective viscosities.

The characteristic velocity of a by-pass pig during a run generally varies between 1 and 5 m/s according to the current literature, but exceptions to this rule of thumb exist [15]. This general range is confirmed by field data that were obtained by pig runs on an 18 inch, 85 km gas-condensate pipeline [27]. The weight of the pig that was used and the diameter of the sealing discs are 77 kg and 447 mm, respectively. The field data that were obtained showed velocities between 1 and 4.5 m/s as the bypass ratio varied between 0 and 10 percent.

The load parameter in lubrication theory corresponds to the wall force F_{wall} on the sealing discs in pigging operations. While many operational conditions can be measured during a pig run, measuring this particular force remains difficult. To generate an expression based on the field data by Olaniyan and Larry [27], the friction force was translated to a wall force by using the friction coefficients found in the dynamic and static pig pull experiments conducted by Graafland [11]. The friction coefficients ranged between 0.68 and 0.83 for the runs with water as a lubricant. To determine the corresponding friction force in the obtained field data, Olaniyan and Larry performed a sensitivity study with the dynamic multiphase simulation tools OLGA and Ledaflow [27]. Both simulators provide the possibility to model a by-pass pig and a sensitivity study was performed on the input friction force values. A reasonable match was obtained between the model predictions and the field data when using an assumed friction force of 3567 N on all discs of the pig. Translating this to one sealing disc and dividing it with the friction force coefficient found by Graafland [11], provides an approximation of the average wall force of 950 N. This value was used as base case for scaling purposes.

3.1.3. Experimental conditions

To simulate the pigging operation, specific experimental conditions will be defined. Since the velocity and load are hard to replicate during an experiment, the viscosity will be a constant factor. Among the fluids encountered by pigs in pipelines, water and dry gas are simple to simulate. Note that condensate is not a safe medium to use in the experiment due to flammability and volatility. Also, it is not straightforward to obtain a matching proxy for the gas-condensate scenario. Liquids such as ether or acetone match the viscosity and surface tension properties, but are not desired due to their unsafe characteristics (flammability, volatility). The closest suitable proxy with a similar viscosity is dodecane. This fluid was therefore used to simulate the condensate scenario. The emulsion scenario is also complicated to reproduce. Emulsions vary heavily over time and are sensitive to ambient conditions. The task to generate consistency in emulsions is too complex and a high viscosity fluid was used instead. Castor oil has a high viscosity and good lubrication properties. This fluid was therefore used to simulate pigging operations in pipelines as a substitute for emulsions.

Summarizing the lubricants that will be used in the experiments:

- Air, with a viscosity of approximately 0.018 cP, which is close to the dry gas scenario.
- Water, which is a direct match to the de-water scenario.
- Dodecane, with a viscosity of 1.5 cP, which is the closest stable fluid to the condensate scenario.
- Castor oil, with a viscosity of 600 cP, is the substitute for highly viscous emulsions.

For a load of 950 N, sliding velocities ranging from 1 m/s to 5 m/s and the discussed viscosities, the Hersey number will be used to scale down to an experimental scale (see Equation 3.1). The ranges found for the four considered cases are:

- $\lambda = [1.9 \cdot 10^{-8}, 9.3 \cdot 10^{-8}]$ when lubricating with air.
- $\lambda = [1.0 \cdot 10^{-6}, 5.2 \cdot 10^{-6}]$ when lubricating with water.
- $\lambda = [1.6 \cdot 10^{-6}, 7.7 \cdot 10^{-6}]$ when lubricating with dodecane.
- $\lambda = [6.2 \cdot 10^{-4}, 3.1 \cdot 10^{-3}]$ when lubricating with Castor oil.

3.1.4. From sealing disc to rubber lip

Investigation of the frictional behaviour of sealing discs would require a considerable facility. A reduction of size was realised by going from a full sealing disc to a rubber lip that was sampled from the sealing disc (see Figure 3.1). This reduces experimental costs, complexity and increases contact transparency, which is necessary for optical investigation of the sliding contact.

The investigated wall-normal force of the sealing disc can be scaled to the rubber lip through the contact surface ratio. A sealing disc with a diameter of 314 mm and a chamfer of 4 mm at an angle of 30 degrees has a contact surface of:

$$A_{sealingdisc} = 4\pi \frac{314 + (314 - 2 * 4 * sin(30))}{2} = 4 \cdot 312\pi mm^2 \tag{3.2}$$

Using a rubber lip with a width of 20 mm and a chamfer of 1 mm, the force ratio becomes:

$$R_{force} = \frac{A_{rubberlip}}{A_{sealingdisc}} = \frac{20}{4 \cdot 312\pi} \approx 0.005 \tag{3.3}$$

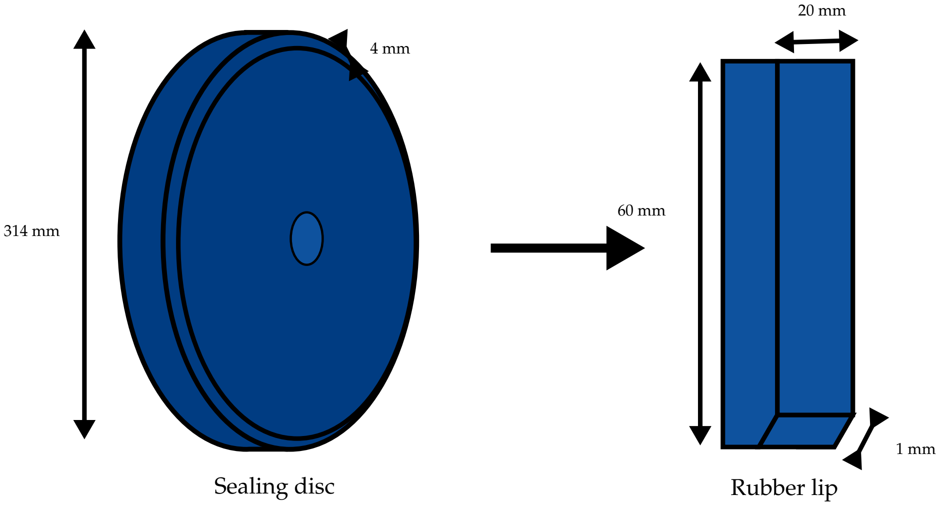

Figure 3.1: Simplifying step from a sealing disc to a rubber lip.

Multiplying this with the wall normal force of the sealing disc results in the new target force for the experiments with the rubber lip:

$$F_{rubberlip} = 950 * R_{force} = 4.75N \tag{3.4}$$

The load is given by the force divided by the width of the contact. By multiplying the calculated load on the rubber lip with the Hersey coefficient ranges in Equation 3.1.3 and dividing by the viscosities results in the required velocity range:

$$U = \frac{\lambda L}{\eta} \rightarrow [0.250, 1.25]\, m/s \tag{3.5}$$

While a target wall normal force was defined, the experiments were conducted with a parameter sweep of both the load L and velocity U. This was necessary to investigate the effect of the load on the frictional contact.

3.2. Pig tribometer facility

The pig tribometer was designed to measure the friction and wall normal force on the rubber contact that slides over a lubricated metal surface embedded in a glass reservoir (see Figure 3.2). In that figure, the glass reservoir in which the rubber contact is sliding over a metal surface is moved to the left during experiments. The measurement device is attached to a manual vertical slider to configurate the wall-normal force on the rubber contact. This vertical slider is fixed to an arm on the table.

To measure the forces on the rubber contact a custom force measurement system was built. Regular transducers operate in force ranges that are too high for this application. Forces can be measured when enough deformation is inflicted to an elastic element. The acting forces are translated to strains by strain gauges that are glued on the surface of the leaf springs. Since the acting forces are very small, leaf springs were used to created an elastic element. To prevent unwanted excitation of the strain gauges by secondary forces, the leaf springs are constructed as fixed double hinges.The double hinges restrain any force into translational movement in two directions: wall normal and tangential to the surface. In this way, force readings caused by misalignment of a few degrees or other external forces and moments are kept to a minimum.

The custom transducer has 16 strain gauges in total. For every double hinge, the inner leaf spring is equipped with 4 strain gauges in a full Wheatstone bridge circuit to improve sensitivity. The signals are read by a PMX data acquisition system from HBM with a PX455 measurment modules for full and half bridges. The four bridges were calibrated by attaching a 1kg weight to a string and redirecting the

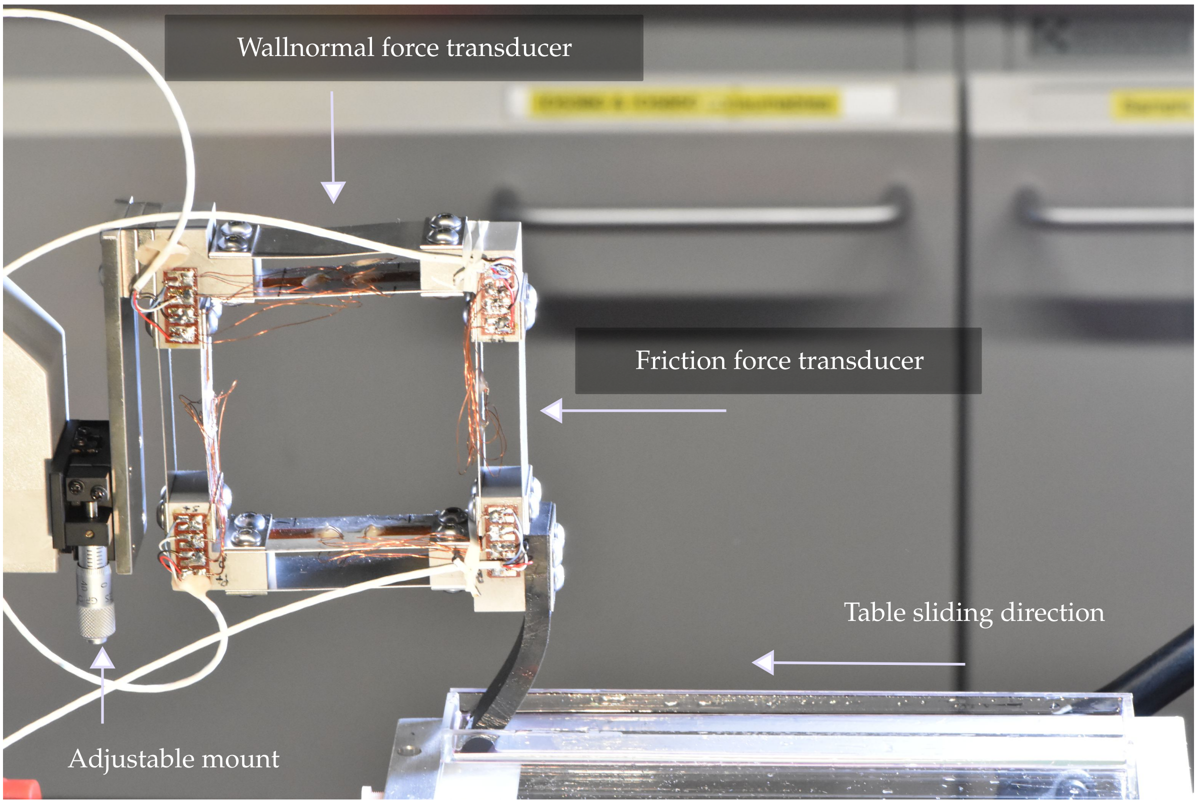

Figure 3.2: Close-up of the force measurement system of the pig tribometer and the sliding motion of the translation table.

force with a pulley. More specific information about the tranducer and the leaf spring system can be found in Appendix B.

Figure 3.3 shows a close-up of the glass reservoir that is used to contain lubricants. Note that a metal plate was embedded in the glass container to simulate the rubber to metal contact. The length of the glass container was 175 mm, but measurements were done over a sliding distance of 170 mm to prevent contact with the short edges. The inner width of the glass channel is 26 mm, which leaves 3 mm of space between both sides of the rubber contact and the glass enclosure. This was shown to be necessary to prevent physical contact with the sides and fluids flowing too high on the side glass. The sliding motion was established by mounting the glass enclosure to a cinematic slider. The specific model was a Kessler Crane Cinedrive, with a sliding velocity between 8.6 mm/s and 86 mm/s. This camera slider is driven by worm gears to assure smooth movement and minimal mechanical response. This option was not sufficient to reach the required 0.25 to 1 m/s velocity, but it was the best option available in the lab. More suitable sliders had building and shipping times that would exceed the duration of this study.

The full setup of the pig tribometer facility is shown in Figure 3.4. A Red Helium 8K camera was used to observe and record the lubricated contact underneath the rubber contact during the experiments. This is a large sensor camera with a high dynamic range to distinguish patterns in the flow of the lubrication. A 10x magnification microscope lens is attached to the camera to solely frame the rubber-metal contact and the layer of lubrication fluid. This corresponds to a recording frame of 1.5 by 3 mm. The disadvantage of a microscope lens was the light required to establish bright recordings. This was eventually manageable with two LED panels. The considerations for this specific set-up can be found in Appendix B.

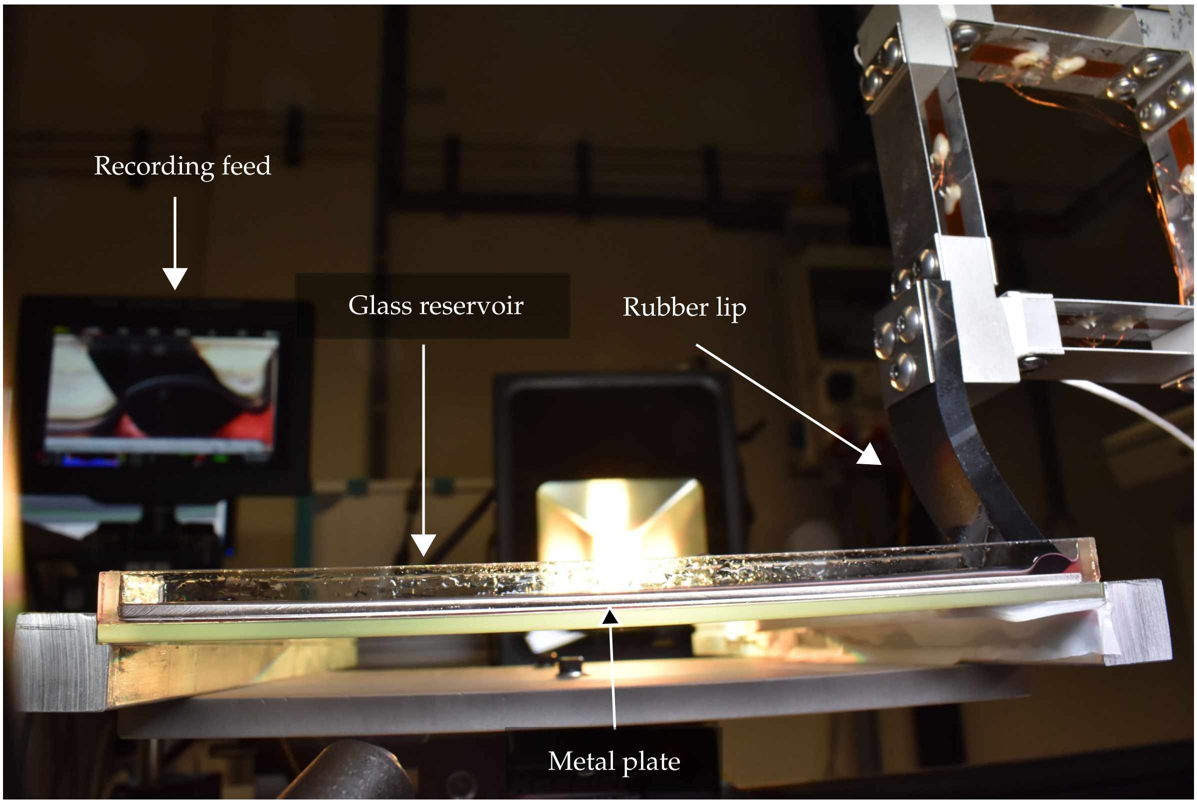
Recording feed
Glass reservoir
Rubber lip
Metal plate

Figure 3.3: Close-up of glass resevoir used to inhibit the lubricants.

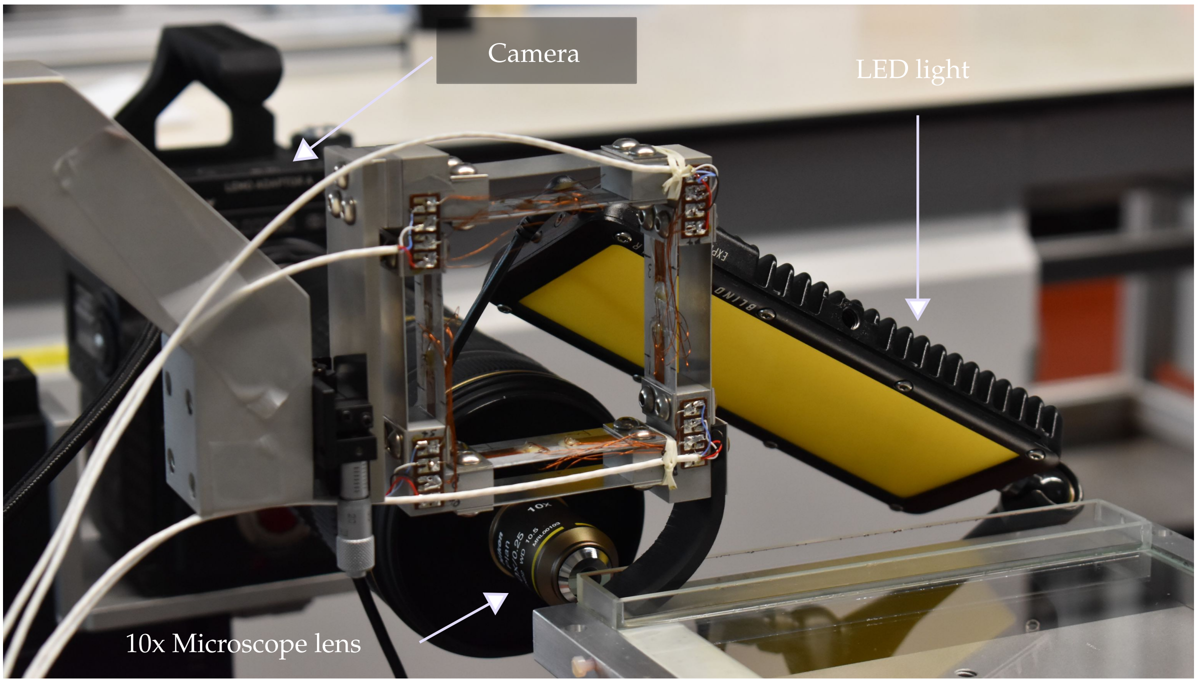
Camera
LED light
10x Microscope lens

Figure 3.4: Close-up of the full pig tribometer experimental setup.

3.2.1. Experimental execution

An experimental run consisted of one slide across the 170 mm long metal plate inside the glass enclosure. A velocity and thickness sweep was performed for air, water, dodecane and castor oil. The velocity sweep went from 10 mm/s to 80 mm/s in increments of 10 mm/s and the thickness sweep went from 6 mm to 10 mm in increments of 2 mm. The thickness variation corresponds to variations in wall-normal force. The experiments were performed four times for every configuration to investigate the standard deviation of the data points.

The camera was a convenient addition to the setup to check the degree of lubrication of the rubber lip in contact with the metal surface. When a new fluid was added to the enclosure, a few runs were conducted to check the fluid levels. Prior to a run the rubber lip was pulled backward to assure full contact of the small chamfer surface. At the end of every run, the measurement device could be lifted from the supporting pin in the adjustable mount to prevent damage during the sliding table's return. When the table returned back to the starting position, the measurement device could be lowered onto the pin and have the same vertical configuration. This also assured that the wall-normal forces would not be influenced by resetting the experiment. The runs with the dodecane required extra attention as this fluid has a low boiling point and evaporates quickly. This fluid had to be monitored more closely with the camera and replenished when necessary. Also the optical glue that was used to construct the glass enclosure eventually dissolved in the dodecane. Therefore, these runs were done at the very last phase in the experimental matrix.

3.3. Experimental data

This section will show what the acquired data look like. Figure 3.5 shows the friction forces as function of the displacement distance for an experimental run without lubricants. The friction force starts at a force that is acting on the lip in the horizontal direction. This is 0 N for the dry case but not necessarily all other experiments. The experimental runs have a clear settling distance, which takes approximately 80 mm. This is similar for the higher velocities, but can vary for other fluids. When the friction force has reached a stable value, the friction force is extracted by taking the mean of the remaining data points. Note that the experiment stops abruptly at 170 mm displacement with a friction force that has not decayed yet. The decay in force happens very slowly after the sliding movement has stopped. An important benchmark of the dry friction experiments is the independence of sliding velocity. This confirmed by Figure 3.5 since the three shown force measurements are almost constant.

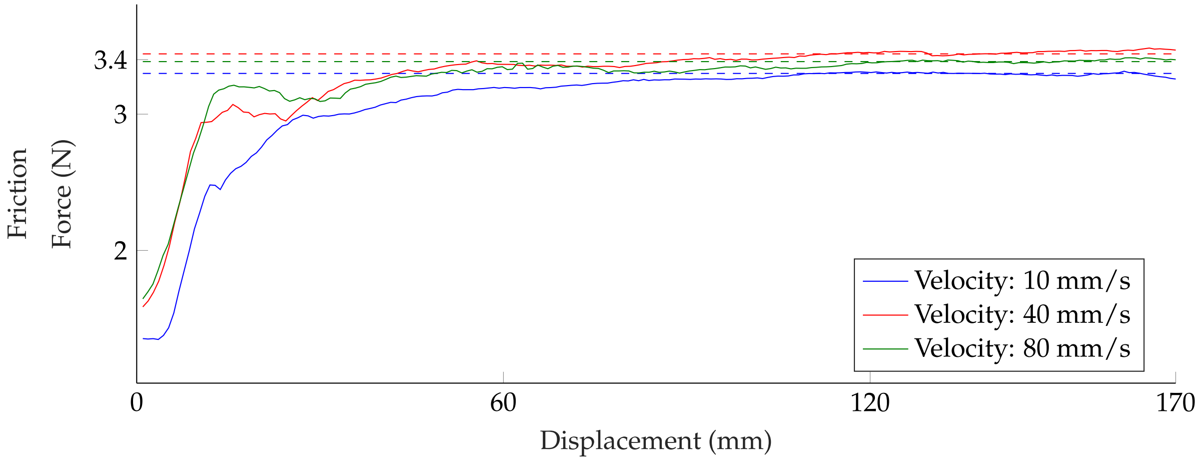

Figure 3.5: Dry friction during a run with a 6mm thick lip for velocities between 10 and 80 mm/s.

Figure 3.6 shows a snapshot of an experiment with castor oil. The lubricants in the experiments were mixed with red dye to improve the contrast of flow patterns in the recordings. The recordings were made at 120 fps in 4K format (4096 × 2160) and processed in the dedicated software for the RED. The 4K video format has a lot of information, which can only be partly transferred to lower resolutions. Sharper images were realised by using the sinc interpolation method in the down-sampling of the resolution.

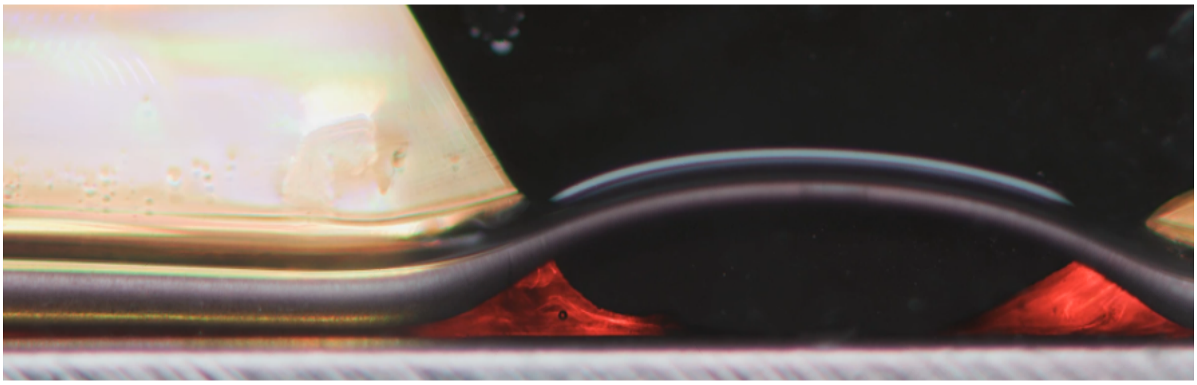

Figure 3.6: Snapshot of an experiment with castor oil and red dye as lubricant.

4

Results

The main focus of this chapter is on the results of the experiments and the models. A parameter study was performed on the facility described in the previous chapter. The first section explains the results from the experimental runs and the results are compared with the predictions from the friction model. The second section investigates the observations of optical phenomena that were registered with the camera.

4.1. Experimental results

4.1.1. General observations

The manual xy-sliders and a detachable mount for the rubber contacts allow for fast testing of a variety of configurations. A parameter sweep was performed to determine the effects of the changes in sliding conditions. Some of the observations that were made during the configuration changes between the runs will be explained in this section. The complexity in realigning the set-up made it difficult to repeat the experiments.

During the runs it was difficult to create a wall-normal force that is equal for similar configurations between the different fluids. Neutralizing this difference and pursuing equal wall-normal forces would mean the distance of the manual slider on the mount would be adjusted for every run. This also changes the angle of the lip with the sliding surface and removes the guarantee of full contact on the chamfer surface. Instead of making the wall-normal force a constant, the contact angle with the sliding surface was held constant. This is the equivalent of using a sealing disc with a fixed diameter.

4.1.2. Friction and wall-normal force

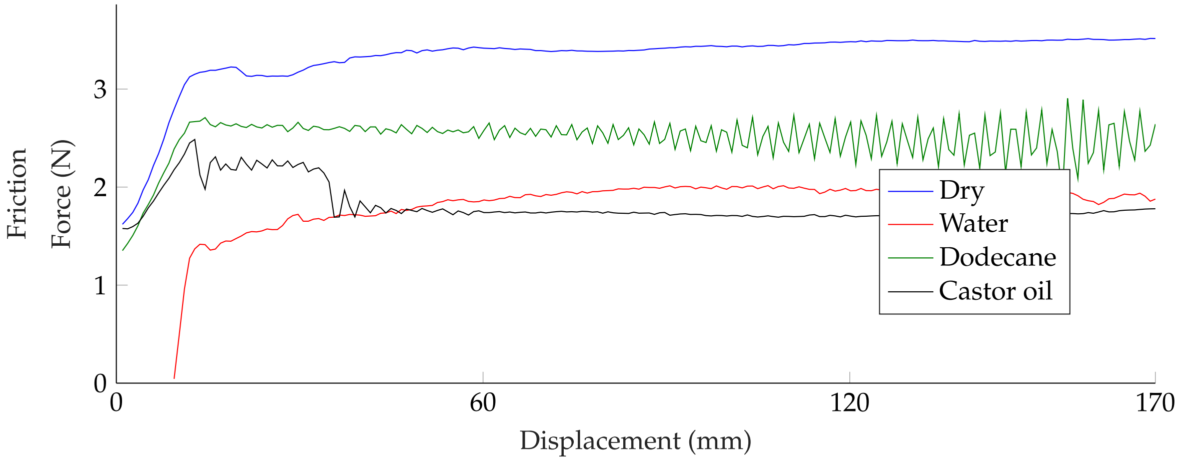

Figure 4.1: Comparison of friction force for dry, water, dodecane and castor oil with an 8 mm thick lip at 60 mm/s.

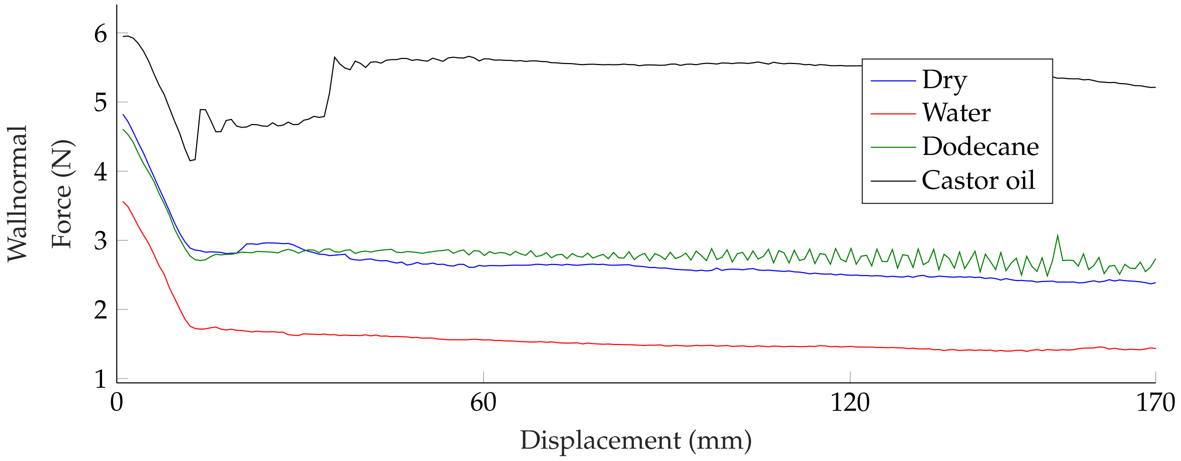

Figure 4.2: Comparison of wall-normal force for dry, water, dodecane and castor oil with an 8 mm thick lip at 60 mm/s.

Figure 4.1 and 4.2 show the comparison of the friction force and wall-normal force, respectively, for the dry, water, dodecane and castor oil scenario. The lip has a thickness of 8 mm and the runs were done at a sliding velocity of 60 mm/s. As shown, the forces differ significantly for the tested lubricants with an equal contact angle. Dry friction clearly reaches the highest value for the friction force compared to the other fluids and castor oil ends up lowest. This pattern is almost the opposite for what is found for the wall-normal force, except that water has the lowest wall-force. Castor oil has the highest wall-normal force in the same configuration and this indicates an inverse relation between the friction force and wall-normal force. The rubber lip is flexible and placed at an angle with the surface. Therefore a higher friction force will tilt the rubber and relieve the wall-normal force. The opposite happens for low friction sliding. The rubber lip will then experience less tilt and places itself in a more perpendicular orientation to the surface. Due to lower stiffness of the rubber lip compared to axi-symmetric bending on sealing discs, this effect is likely to be lower for pigs.

Notice that the dry and water lubricated runs have a similar behaviour in both friction and wall-normal force trajectory, but dodecane and castor oil follow different patterns. The castor oil trajectory first shows an increase in friction force that is similar to what occurs for the other fluid and then suddenly decreases into a steady state. During the first 40 mm of displacement the sliding velocity is still building up towards the configured sliding value. The change of behaviour during this part of the run indicates a strong dependence on the sliding velocity. This effect agrees with the literature but is not observed in the experiments with the other lubricants. The sudden turn in the ramp-up of the friction force is caused by transitioning from the boundary lubrication to the mixed lubrication regime. This will be shown later when a comparison is made with the friction model.

Dodecane is the only fluid that shows an increase in oscillation magnitude as a larger sliding distance is covered. It was verified by the camera recordings that these oscillations are the result of stick-slip behaviour between the rubber lip and the sliding surface. While there is a mechanical response of the measurement device, it is not simply caused by a natural frequency.

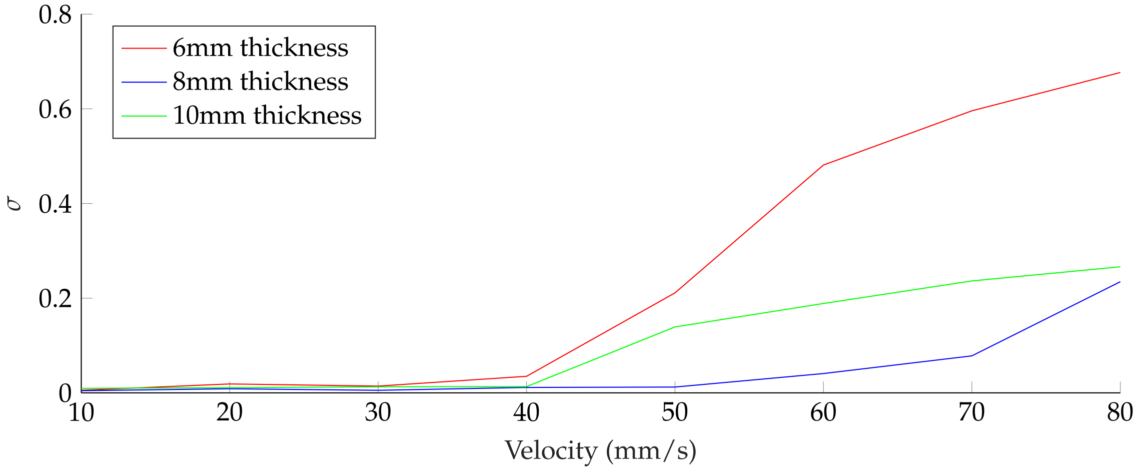

Figure 4.3: Standard deviation of the dodecane friction force trajectory as function of sliding velocity for different thicknesses.

Figure 4.3 shows the standard deviation of the friction coefficient trajectories for dodecane. This was sampled between a sliding displacement of 130 and 160 mm and indicates the magnitude of the oscillation. The graph shows that the stick-slip behaviour starts from a sliding velocity of 40 mm/s and increases proportionally to the sliding velocity. Notice that the experimental runs with a 6 mm thick rubber contact show significantly stronger stick slip behaviour and 8 mm has the weakest stick-slip behaviour. It is be expected that the 10 mm runs would have the lowest magnitude of the three, since the rigidity of that rubber contact is higher. A theory for this behaviour is that the mechanical response of the 8 mm rubber has better damping performance.

More comparisons for the friction force, wall-normal force and friction coefficient have been carried out and can be found in Appendix C.

4.1.3. Friction coefficient vs thickness

This section shows error bars of the friction coefficient as function of the sliding velocity. The three curves represent the thicknesses of the rubber contact, which are 6 mm, 8 mm and 10 mm. The width of the error bars is defined by one standard deviation.

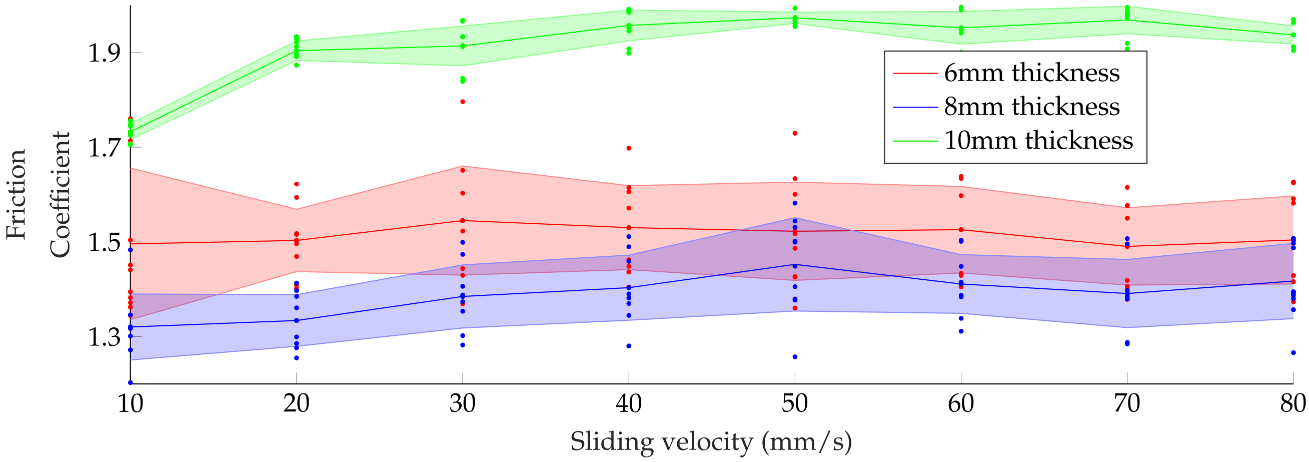

Figure 4.4: Error bar of the dry friction coefficients as function of the sliding velocity for different thicknesses of the rubber contact.

Figure 4.4 shows the error bar of the dry friction experiments. Notice that the thickness of the rubber contact has a significant effect on the friction coefficient of the dry experiments. The friction coefficient seems to be more sensitive to the sliding velocity in the 8 and 10 mm thickness cases. While the constant behaviour of the 6 mm run is expected, the 8 and 10 mm runs show an increase in friction coefficient from 10 to 50 mm/s. Notice that the average friction coefficient drops from 1.5 to 1.4 when changing the thickness from 6 to 8 mm and the friction coefficient increases to an average of 1.9 when the 10 mm rubber contact is used. A possible cause for this is that the friction force in the 10 mm experiments sometimes exceeded the strain limit of the strain gauges. Despite the number of reruns that had to be performed, the result could still be divergent due to nonlinear effects in the limit of the strain gauges. Another notable detail is the decrease in standard deviation for increasing rubber contact thickness. During the experiments the camera recordings showed a more solid contact between the rubber and the sliding surface for the 10 mm case in comparison with the 6 and 8 mm cases. This was generally true for all lubricants.

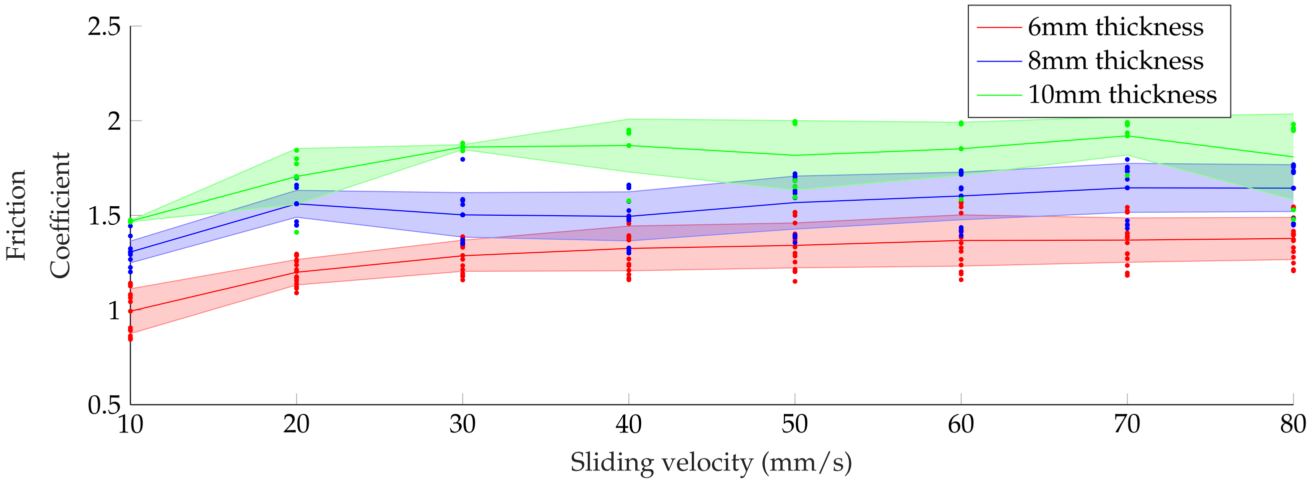

Figure 4.5: Error bar of the friction coefficients of water as function of the sliding velocity for different thicknesses of the rubber contact.

Figure 4.5 shows the error bar of the friction experiments that were conducted with water. This comparison also shows a slight increase in the friction coefficient in the step from 10 to 20 mm/s that is similar to the dry friction case. For the remaining velocities the friction stays approximately constant. Also, there is a positive relation between the friction coefficient and the thickness of the rubber contact.

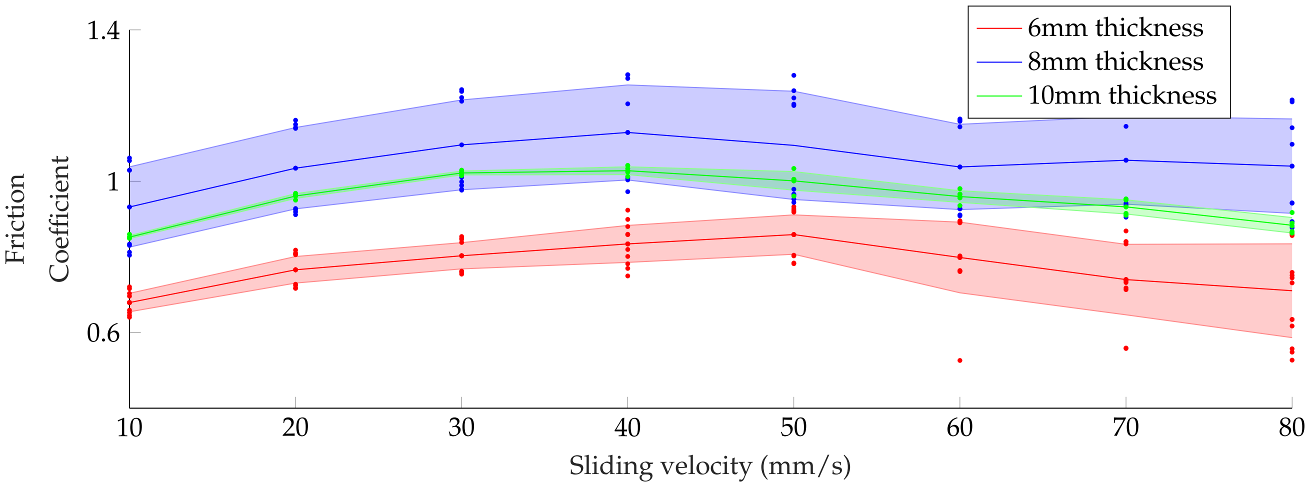

Figure 4.6: Error bar of the friction coefficients of dodecane as function of the sliding velocity for different thicknesses of the rubber contact.

Figure 4.6 shows the error bar for the friction experiments with dodecane. These results are less similar than the dry and water lubricated series. The friction coefficient increases slightly until 40 mm/s and then starts to decrease again in the 40 to 80 mm/s range. The 40 mm/s is also the sliding velocity at which the stick slip behaviour starts to develop. The friction coefficient for the stick-slip experiments is determined by taking the mean from the oscillating friction coefficient trajectory. An example of this can be found in Appendix C. This implies that stick-slip behaviour potentially reduces the effective friction coefficient during a sliding movement. There is a slight increase noticeable for the standard deviation of the curves as the sliding velocity increases. Also, the standard deviation of the 10 mm dodecane experiments is relatively low. This is due to the removal of outliers for those experiments in which one of the two wall-normal force transducers measured extreme values. This was likely to be caused by the stick-slip behaviour. The same separation between the two wall-normal transducers is also visible for the 8 mm case. The mean friction coeffcient lies just in between two clusters of measurements that are approximately one standard deviation away from the mean.

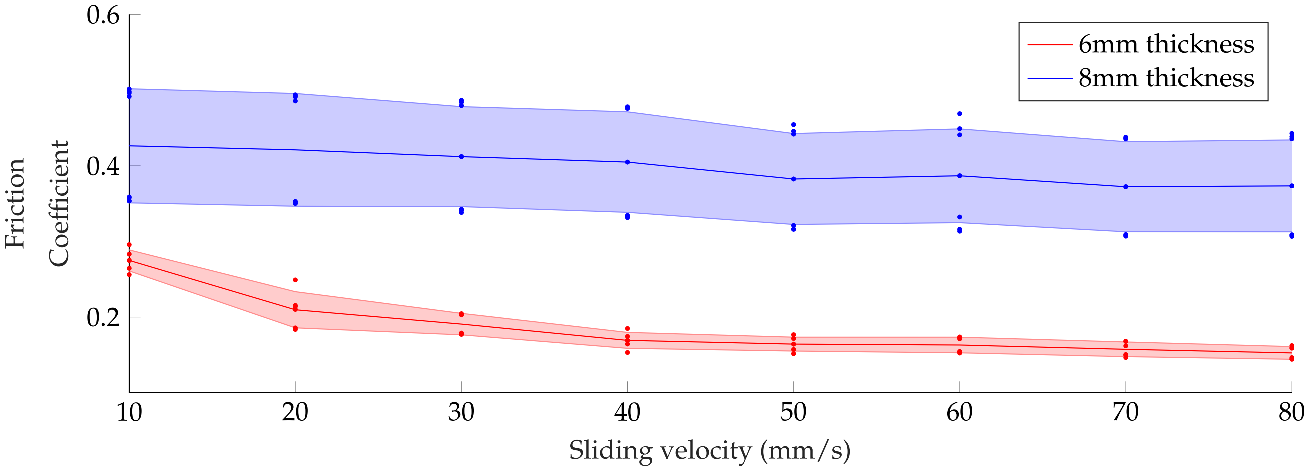

Figure 4.7: Error bar of the friction coefficients of castor oil as function of the sliding velocity for different thicknesses of the rubber contact.

Figure 4.7 shows the error bar representation of the castor oil experiments. This is the only curve that shows a slight but clear decrease of the friction coefficient as the sliding velocity increases. Note that the 10 mm experiment is not included because the wall-normal force limit of the strain gauges was exceeded and this resulted in inconsistent measurements. In the 8 mm experiment this causes the same two separated clusters of data points that are visible as in the dodecane analysis. The 6 mm experiments had a lower wall-normal force and therefore do not show the same effect.

4.1.4. Model validation

To validate the shape of the stribeck curve with the experiments, the friction coefficients of the four fluids were fitted to curves generated by the model. The curves were fitted by adjusting the surface roughness parameters to one setting that suits all. The involved parameters are the standard deviation of the asperity height σ_s, the curvature of the asperities β and the amount of asperities per square meter n. Then the boundary friction coefficient was fitted to suit the experimental data per fluid individually.

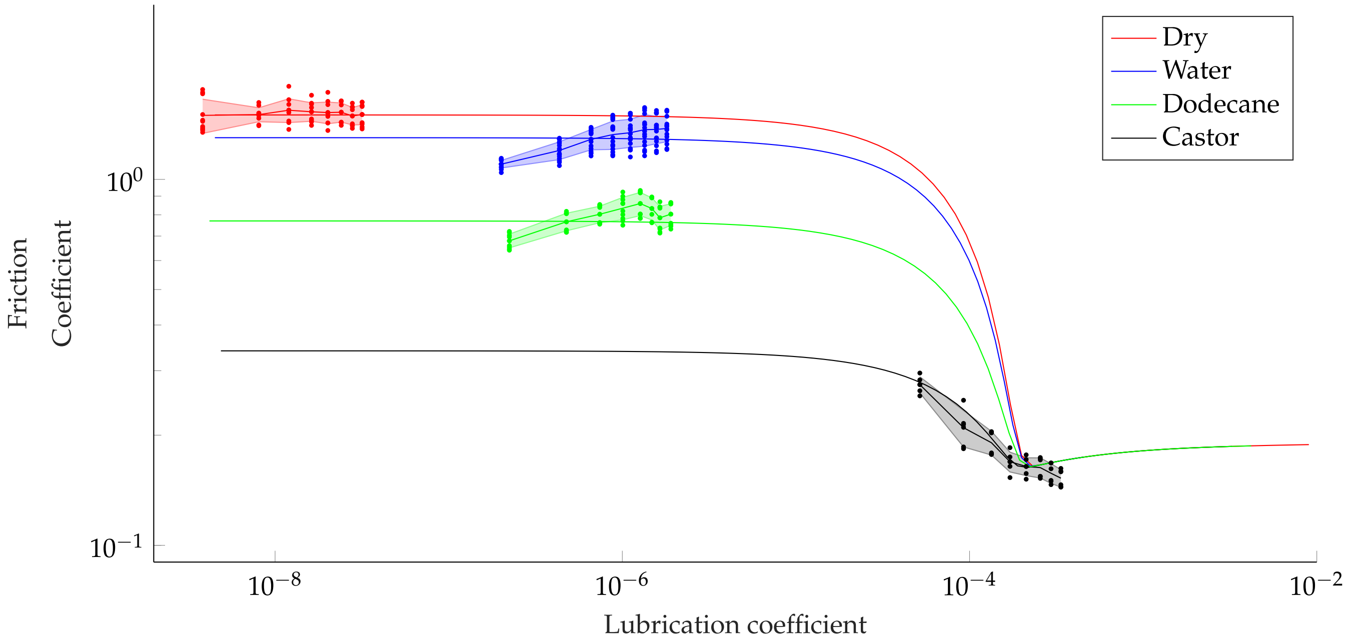

Figure 4.8: Stribeck curve fitted with the friction experiments for the investigated fluids with a rubber contact thickness of 6 mm.

Figure 4.8 shows the resulting four Stribeck curves that are fitted to the experimental data. A rubber contact thickness of 6 mm corresponds to the data points. It is clear that the dry, water and dodecane cases were conducted in the boundary lubrication regime and castor oil is in the mixed lubrication regime. A reasonable fit was found for the dry friction and castor oil experiments. The dry friction run has the lowest lubrication coefficient, which is due to the low viscosity of air. Its mean is almost constant, which is in accordance to the Stribeck curve. The Castor oil corresponds to a much larger lubrication coefficient and marks the transition from boundary lubrication to hydrodynamic lubrication. Both water and dodecane have similar lubrication coefficients and are mapped in the boundary lubrication regime, but are not independent of the lubrication coefficient. Note that their increase in friction coefficient is also very similar. This could imply an extra detail in the Stribeck curve that is not included in the used model. While more samples over a greater range would be beneficial to generate a better validation, the castor oil data prove that a sudden decrease in the friction coefficient is possible. This agrees with the theory of a transition regime after the boundary lubrication regime.

4.1.5. Link with pigging operations

In the oil industry much is unknown about the friction coefficient during a pig run. The wall-normal force cannot be registered during a pigging operation and the friction force can only be derived from measurements of other physical parameters like the pressure and the pigging velocity. This study investigates the friction coefficient of polyurethane rubber to metal contact and correlates it to relevant parameters that could potentially be adjusted in field operations. Figures 4.4 to 4.7 show these friction coefficients for fluids that have similar viscosities as those in pipelines. The specifications of the experimental set-up may not be fully sufficient to achieve complete scaling from field operations to experiments, but the figures do show relevant friction behaviour that occurs when a pig slows down. The results with Castor oil correspond with the mixed lubrication regime. This is the frictional behaviour that is linked to higher lubrication coefficients. The whole of these data points partly validate the Stribeck Curve in Figure 4.8.

For pigging operations the relation between the friction coefficient and the velocity, viscosity and load is important to understand. A pig that operates in pipelines with low viscosity fluids is relatively insensitive to changes in the pigging velocity. This does not hold for high viscosity products like wax and heavy oils. A pig could then potentially be operating in the mixed lubrication regime and any obstacle that slows down the pig increases the friction coefficient significantly. The lubrication regime would then shift from the mixed regime to the boundary regime. A combination of this phenomenon and long liquid slugs or solid slurries in front of the pig could potentially lead to a stalled pig. Once a pig is stalled in a pipeline with high viscosity oil, the friction coefficient becomes 10 times higher in comparison to the dynamic friction coefficient during normal pigging velocities.

4.2. Visual observations

Every experiment was at least recorded once to investigate the behaviour of the fluids during sliding motion. Despite the red dye, experiments with water and dodecane did not show any distinctive behaviour of the fluid flow. This was different for the castor oil experiment. Due to the high viscosity, flow patterns were traceable with the 120 fps recordings. Figures 4.9 till 4.14 show frames that were taken from the recordings of the castor oil experiments at a sliding velocity of 10 mm/s for the 6 mm thick rubber contact.

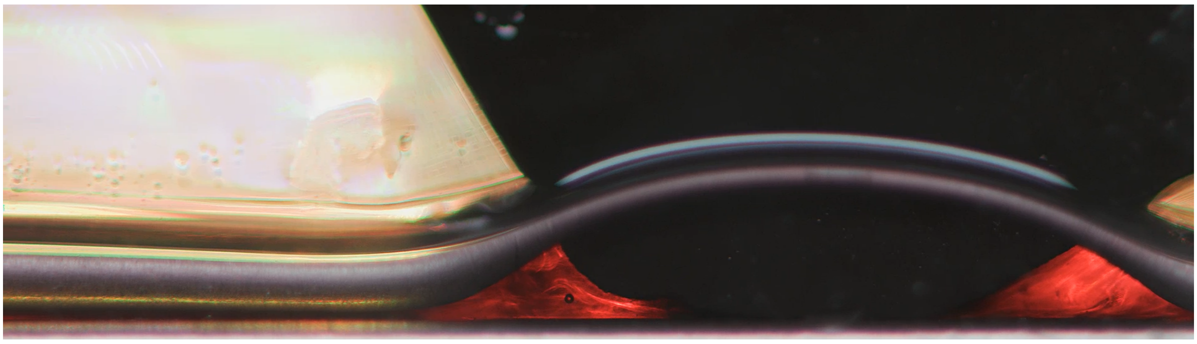

Figure 4.9: Rubber contact during the experimental run with castor oil at a sliding distance of 0 mm.

Figure 4.9 shows the rubber contact before the sliding motion. As shown in the figure, the fluid layer consists of a dark edge at the top, gray section in the middle and a red glowing section underneath. The dark edge and the gray section are both reflections caused by the contact angle of the fluid with the glass enclosure as a result of surface tension. The true fluid level can therefore be measured from just underneath the gray section to the metal plate. This is approximately 0.2 mm thick and is the minimum level that was required to generate consistent results. Increasing the thickness of the fluid layer in the glass enclosure led to an increase of the friction coefficient. An excess amount of fluid builds up in front of the rubber lip and flows between the sides of the rubber lip and the sides of the glass enclosure. This is adding an extra friction source due to fluid drag.

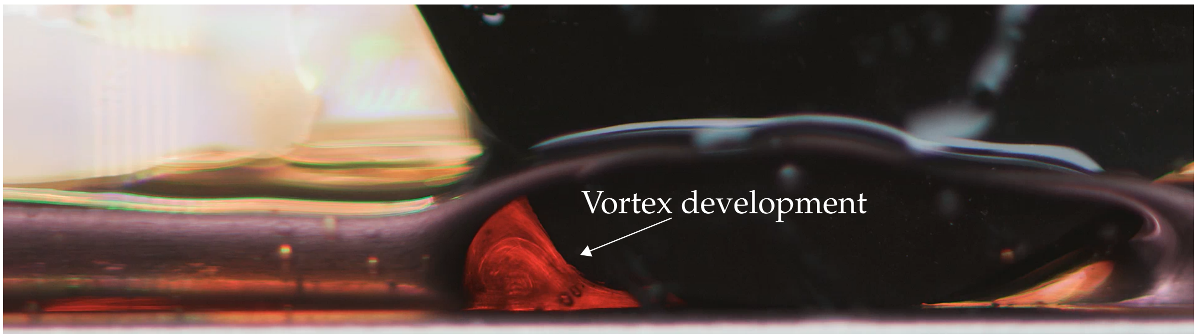

Figure 4.10: Rubber contact during the experimental run with castor oil at a sliding distance of 35 mm, showing the first vortex development just in front of the rubber.

Figure 4.10 shows a frame of the experimental run after a sliding distance of 35 mm was traveled. In front of the rubber contact a vortex starts to develop that rotates in counterclockwise direction.

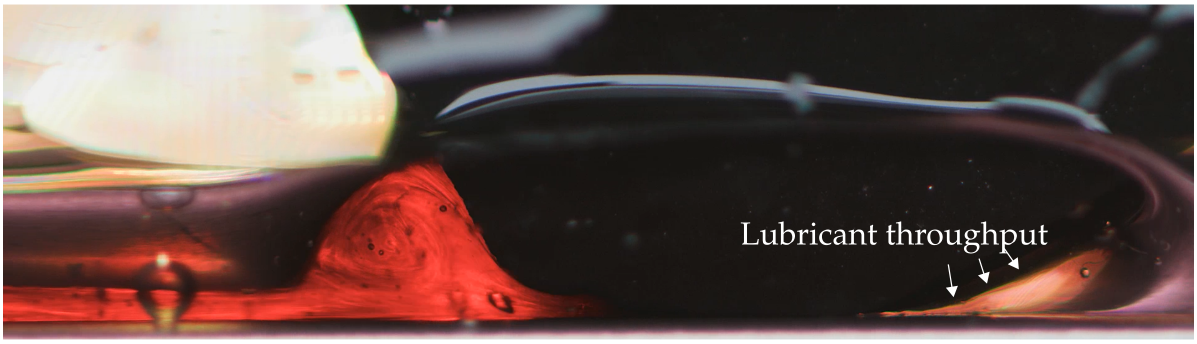

Figure 4.11: Rubber contact during the experimental run with castor oil at a sliding distance of 51 mm.

Figure 4.11 shows a frame that was taken after a sliding distance of 51 mm. The vortex in front of the rubber contact has become larger and after the rubber a small jet of lubricant is visible. This means that there is significant flow throughput underneath the rubber. This agrees with the theory that the castor oil experiments operate in the mixed lubrication regime. Both the fluid shear and solid friction determine the friction force on the rubber.

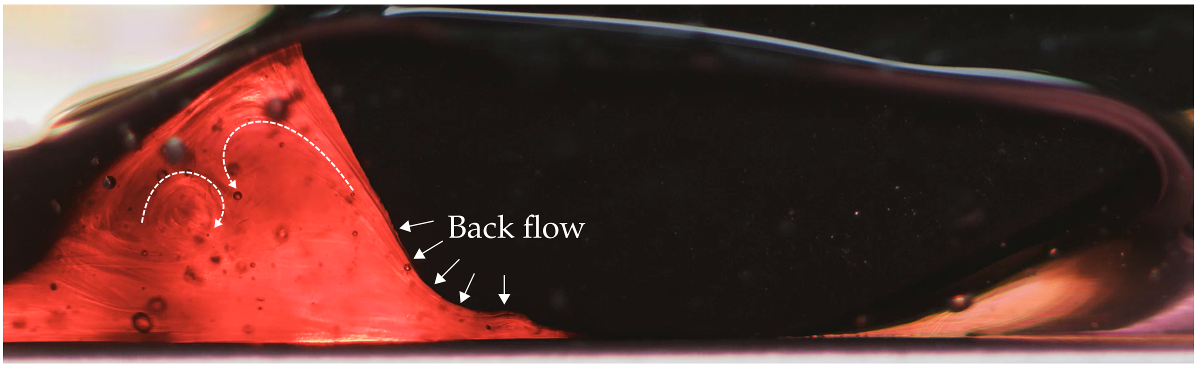

Figure 4.12: Rubber contact during the experimental run with castor oil at a sliding distance of 69 mm.

In Figure 4.12 the sliding distance has passed 59 mm and two counter-rotating vortices can be distinguished. This is the result of fluid hold-up in front of the rubber contact. Another new detail is back flow against the front of the rubber. Some flow passes the rubber, but another fraction ends up in front of the contact through this back flow. This was already slightly visible in Figure 4.11, where the first occurring vortex is the result of this back flow. The lubricant throughput has also become stronger due to the amount of fluid in front of the rubber contact. This means that experimental runs over larger sliding distances could result in lower friction coefficients due to more fluid hold-up. This is an interesting feature that also applies to pigging operations, where slugs are pushed through the pipeline by pigs. The fluid pressure in front of the rubber contact results into lower effective friction coefficients.

Figure 4.13: Rubber contact during the experimental run with castor oil at a sliding distance of 98 mm.

In figure 4.13 a sliding distance of 98 mm has been traveled and now one larger vortex resides in the fluid hold-up with multiple smaller vortices encapsulated by it. The lubricant throughput has again increased for an increase in sliding distance.

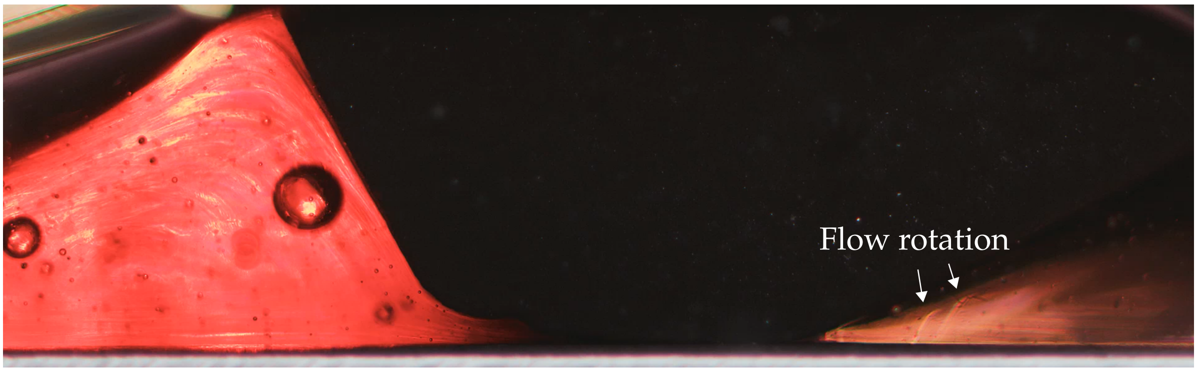

Figure 4.14: Rubber contact during the experimental run with castor oil after the sliding motion has stopped.

Figure 4.14 shows a frame right after the sliding motion has stopped and the fluids are settling to a resting state. The remaining fluid behind the rubber contact show streamlines that indicate rotation of the flow. This could be a wall effect that induces this pattern underneath the rubber contact, but otherwise this means that the often used 2D models can not completely represent the flow for this specific frictional behaviour.

5

Discussion

Pigging operations in pipelines pose a high risk as the pig can get stuck. Knowledge of the friction forces on the pigs could mitigate or fully prevent these problems, but current pig friction models are unable to successfully predict frictional behaviour under lubricated conditions. This remains the case as the present study has not led to fully accurate predictions of the experimental runs. Also, the conducted experiments are a representation of the rubber to metal contact that occurs during pigging operations, but they do not fully represent the axi-symmetric confinement of a pig in a pipeline. Identification of the global dependencies through which friction forces on pigs vary will facilitate the development of new models with improved prediction accuracy.

Experiments
In this project the forces that result from rubber to metal contact were measured under similar conditions as pipeline pigs experience friction. These findings were fitted to a Stribeck-curve based friction model to predict the further development of the friction coefficient for higher velocities. This identified a high risk region in the mixed lubrication regime of the Stribeck curve in which the velocity of the pig can be greatly reduced. The friction coefficient strongly decreases in the mixed lubrication regime as a result of an increase of the lubrication coefficient. The lubrication coefficient has a proportional dependence on the velocity and the viscosity, meaning that a decrease of both parameters in the mixed lubrication regime leads to an increase of the friction coefficient. This will subsequently decrease the pigging velocity even further, which can cause the pig to get stuck. This is consistent with the findings of Faraon [10], who observed the same decrease in friction force during experiments in the mixed lubrication regime. Graafland [11] and Graafland and et al. [14] measured slightly lower friction coefficients during their pig pull experiments. Important differences between the experiments include the type of contact and the surface material used during the experiments. Graafland used the field size discs in short polymer pipeline sections to perform pig pulls.

Models
The modelled Stribeck curve has shown to be helpful in determining the approximate development of the friction coefficient as function of the velocity, viscosity and load. Note that the model needs many input parameters of which a few are complex surface topology properties. These properties can only be fully determined by performing surface scans of the regarding material. As there was no facility to measure the surface topology, it was chosen to fit the surface parameters to the experimental results. Note that the model could not be made to fit any shape of experimental results. Only the transition locations can be influenced by the input parameters for the surface topology up to a certain limit. However, the model still seems to be useful for future studies to serve as a prediction tool that can be calibrated with samples of experimental results.

The FEM simulations have shown to be useful in determining the wall force for different oversizes during confinement of the sealing disc. Both linear and nonlinear simulations were performed and their differences were compared with the change of strain density. Simulations with the nonlinear model generally resulted in a larger wall force than the simulations with a linear model. The nonlinear simulations were also relatively unstable compared to the linear simulations due to the extra degrees of freedom. This caused abrupt stops of the confinement trajectory for the higher oversize simulations due to friction forces that did not numerically converge. Rigorous sealing discs guidance and damping were therefore added to investigate the steady state forces during full confinement. Extensive stability analyses fell outside the scope of this thesis, but the obtained results will facilitate future progress in nonlinear FEM simulations on frictional contacts.

6

Conclusions

Results from the investigated friction model and the nonlinear FEM simulations were presented in Chapter 2. The friction model describes the trend of the friction coefficient as function of the velocity, viscosity and wall-normal force. The FEM simulations investigated the effect of the sealing disc oversize on the wall-normal force and on the ramp-up of the friction force.

The results presented in the previous chapter gave insight in the frictional behaviour of pipeline pigs. The newly built experimental facility was able to measure the friction and wall-normal force on lubricated sliding contacts and did provide optical recordings of the experiments. The influence of velocity, wall-normal force and lubricant on the friction coefficient was investigated through a parameter study. The obtained results were then used to validate the discussed friction model and relate optically observed phenomena to the variation in parameters.

Conclusions from this thesis study:

- The operational parameters of lubricated friction on sliding surfaces can be divided into three lubrication regimes. A change of regime leads to a significant change in friction coefficient.
- Curve fits applied to stress-strain curves of polyurethane rubber used on pig sealing discs showed linear behaviour up to 20% strain. Peak stresses found in the results from linear and nonlinear simulations of a sealing disc confinement exceeded this 20% for oversizes of 3 and 4 percent.
- The experimental results for both the friction force and the wall-normal force showed a significantly different behaviour for the four tested fluids. For the same experimental conditions, dry friction ended up with the highest measured friction force and castor oil with the lowest. For the wall-normal force, castor oil gave the highest value and water the lowest. This inversely proportional pattern can be explained by extra tilt of the rubber contact caused by higher friction forces. This reduces both the wall-normal oriented stiffness of the rubber contact and the wall-normal force.
- Experiments conducted with castor oil showed a transition in the rate of change of the friction force when the slide velocity is increased. The friction force first increased for an increase in sliding velocity and suddenly decreased by a further increase in sliding velocity. This reduction in friction force was interpreted as a transition from the boundary lubrication regime to the mixed lubrication regime.
- The dodecane experiments also show an increase for the friction coefficient until a sliding velocity of 40 mm/s is reached. This is the velocity at which stick-slip behaviour starts to develop. The friction coefficients slightly decreases when increasing the velocity from this point.
- For all tested fluids, a decrease in the standard deviation of the experimental data for the forces was noticeable when the thickness of the rubber contact was increased.
- For the dry friction experiments an increase in the sliding velocity led to a logarithmic increase in the friction coefficient for a rubber contact thickness of 8 and 10 mm. The 6 mm experiments showed an approximately constant friction coefficient as function of the sliding velocity.
- The experiments with water also showed an increase of the friction coefficient by increasing the sliding velocity for all tested rubber contacts.
- The castor oil experiments were the only ones that showed a decrease in the friction coefficient when increasing the sliding velocity. This is due to the high viscosity of castor oil, which sets lower friction conditions for these experiments.
- A validation study was performed by fitting the friction model to the obtained experimental results. The data from the dry, water and dodecane experiments are mapped in the boundary lubrication regime of the generated Stribeck curve. Only the dry results have good agreement with the constant behaviour the friction coefficient in this regime. Both the water and dodecane experiments show a slight increase for the friction coefficient with increasing lubrication factor and are in mediocre agreement with the friction model. Results from the castor oil experiment are in the mixed lubrication regime of the Stribeck curve and are in reasonable agreement with the model.
- Depending on the production fluids, pigs can operate in different regimes of the Stribeck curve. This knowledge is critical since the friction coefficient can significantly increase when a pig is slowed down momentarily in the mixed or hydrodynamic lubrication regime. This will decrease its velocity even more and can lead to a stalled pig.
- Camera observations show the development of vortices in front of the rubber contact and the lubricant flow underneath the rubber for the castor oil experiments. This implies that the castor oil experiments operated in the mixed lubrication regime.

7

Recommendations

This thesis study has given insight in the frictional behaviour of pipeline pigs. This insight was used to formulate conclusions on the work that was done, but it also points out directions for further research. The recommendations for future experimental work are the following:

- Performing experiments at higher sliding velocities. This way the friction coefficient can be determined over multiple lubrication regimes for one configuration.
- Using emulsions as a lubricant with the sliding experiments and comparing multiple types of rubber.
- Using thicker leaf springs for future custom load cells. The sensitivity of the current set-up was too large and did exceed the 10 N force in any of the directions, which resulted in slipping strain gauges.
- Finding a suitable method to calibrate the model (that has a range of input parameters) with experimental results. The complexity of lubricated friction models lies in the dependence of many parameters which are hard to determine up front. Model calibration with Kriging or Markov Chain Monte Carlo could establish a prediction tool that is aligned with a specific set-up or pig configuration.
- Using cruise control pigs to generate real-time data from in field pigging operations.

Bibliography

[1] A guide to the use of the HBM K series foil strain gages and accesories. Manual, Hottinger Baldwin Messtchnik GmbH, Darmstadt, Germany, 2008.

[2] Measuring strain with strain gauges. Electronic article, National Instruments, 2016. URL `http://www.ni.com/white-paper/3642/en/`.

[3] How to evaluate camera sensitivity. Report, FLIR Integrated Imageing resources Inc., 2017.

[4] Color camera sensor review. Report, FLIR Integrated Imageing resources Inc., 2017. URL `https://eu.ptgrey.com/support/downloads/10786`.

[5] S. Awtar, J. Ustick, and S. Sen. An xyz parallel-kinematic flexure mechanism with geometrically decoupled degrees of freedom. *Journal of Mechanisms and Robotics*, 5(1), 2012. ISSN 1942-4302. doi: 10.1115/1.4007768.

[6] D. M. Brouwer, J. P. Meijaard, and J. B. Jonker. Large deflection stiffness analysis of parallel prismatic leaf-spring flexures. *Precision Engineering*, 37(3):505–521, 2013. ISSN 01416359. doi: 10.1016/j.precisioneng.2012.11.008.

[7] MicroscopyU by Nikon. Matching camera to microscope resolution, 2018. URL `https://www.microscopyu.com/tutorials/matching-camera-to-microscope-resolution`.

[8] J.L. Cordell. Conventional pigs - what to use and why. *Pipes and pipelines international*, 1992.

[9] A. Den Heijer. Frictional behavior of pigs in motion. Master's thesis, Delft University of Technology, 2016.

[10] I.C. Faraon. *Mixed lubricating line contacts*. Dissertation, University of Twente, 2005.

[11] C.M Graafland. *Frictional behaviour of pigs*. Thesis, Delft University of Technology, 2017.

[12] J. A. Greenwood and J. B. P. Williamson. Contact of nominally flat surfaces. *Proceedings of the Royal Society of London. Series A, Mathematical and Physical Sciences*, 295(1442):300–319, 1966. ISSN 0080-4630.

[13] B.J. Hamrock, S.R. Schmid, and B.O. Jacobson. *Fundamentals of fluid film lubrication*. Marcel Dekker, New York :, 2nd ed. edition, 2004. ISBN 0824751205 9780824751203 9780203021187 0203021185 9780824753719 0824753712.

[14] M. H.W. Hendrix, C. M. Graafland, and R. A.J. van Ostayen. Frictional forces for disc-type pigging of pipelines. *Journal of Petroleum Science and Engineering*, 171:905–918, 2018. ISSN 0920-4105. doi: 10.1016/j.petrol.2018.07.076.

[15] R.A.W.M. Henkes. Guidelines for the hydraulic design and operation of multiphase flow pipeline systems. Report, Shell Global Solutions International B.V., 2014.

[16] M. Z. Huq and J. P. Celis. Expressing wear rate in sliding contacts based on dissipated energy. *Wear*, 252(5):375–383, 2002. ISSN 0043-1648. doi: https://doi.org/10.1016/S0043-1648(01)00867-5.

[17] S Inoué and R. Oldenbourg. *Microscopes*, volume II. McGraw-Hill Education, 2009.

[18] K. L. Johnson. *Contact mechanics*. Cambridge University Press, Cambridge [Cambridgeshire] ;, 1985. ISBN 9781615832187 1615832181 9781139171731 1139171739.

[19] B. Lorenz. *Contact Mechanics and Friction of Elastic Solids on Hard and Rough Substrates*. Dissertation, Aachen University, 2012.

[20] F. Malan. Sensor size perspective and depth of field, 2017. URL `https://photographylife.com/sensor-size-perspective-and-depth-of-field`.

[21] J. Nimmons M.H. Chow. Pig pull tests. Report, Shell International Exploration and Production Inc., 2014.

[22] P. Moeleker, G. van Spronsen, R. A. W. M. Henkes, and G. Groote. Bypass pigging guidelines. Report, Shell Global Solutions International B.V., 2014.

[23] H. Moes. *Lubrication and beyond*.

[24] N. Money, D. Cockfield, S. Mayo, and G. Smith. Dynamic speed control in high velocity pipelines. *Pigging products and services association*, 2012.

[25] Aidan F. O'Donoghue. *On the Steady State Motion of Conventional Pipeline Pigs using Incompressible Drive Media*. Phd, Cranfield University, 1996.

[26] King of Hearts. Central Park New York May, 2015.

[27] Y. Olaniyan and D. Larry. Bypass pig modeling – a three phase gas condensate pipeline field case. Report, BHR Group, 2014.

[28] J. Quarini and S. Shire. A review of fluid-driven pipeline pigs and their applications. *Proceedings of the Institution of Mechanical Engineers, Part E: Journal of Process Mechanical Engineering*, 221(1): 1–10, 2007. ISSN 0954-4089 2041-3009. doi: 10.1243/0954408jpme108.

[29] J. Tiratsoo. *Pipeline Pigging and Integrity Technology*. CLARION TECHNICAL CONFERENCES LLC, 2013.

[30] Tribonet. Greenwoodś contact model, 2017. URL `http://www.tribonet.org/wiki/greenwoods-contact-model/`.

[31] Tribonet. Archard wear equation, 2017. URL `http://www.tribonet.org/wiki/archard-wear-equation/`.

[32] H. Zhang, C. Sanchez, S. Liu, S. Zhang, and H. Liang. Wear of a polyurethane rubber used in dry gas pipeline as inspection gauges. *Journal of Natural Gas Science and Engineering*, 41:40–48, 2017. ISSN 18755100. doi: 10.1016/j.jngse.2017.02.035.

[33] D. Zhu, J. Wang, and Q. Jane Wang. On the stribeck curves for lubricated counterformal contacts of rough surfaces. *Journal of Tribology*, 137(2), 2014. ISSN 0742-4787. doi: 10.1115/1.4028881.

[34] X. Zhu, S. Zhang, X. Li, D. Wang, and D. Yu. Numerical simulation of contact force on bi-directional pig in gas pipeline: At the early stage of pigging. *Journal of Natural Gas Science and Engineering*, 23:127–138, 2015. ISSN 18755100. doi: 10.1016/j.jngse.2015.01.034.

[35] Xiaoxiao Zhu, Deguo Wang, Hoi Yeung, Shimin Zhang, and Shuhai Liu. Comparison of linear and nonlinear simulations of bidirectional pig contact forces in gas pipelines. *Journal of Natural Gas Science and Engineering*, 27:151 – 157, 2015. ISSN 1875-5100. doi: https://doi.org/10.1016/j.jngse.2015.08.048. URL `http://www.sciencedirect.com/science/article/pii/S187551001530113X`.

A

Modelled rubber lip

The 2D rectangular model implementation in COMSOL describes the deformation of a rectangular rubber lip that slides along a smooth surface. This COMSOL simulation was performed to calculate suitable thicknesses to use in the lab experiments. Figure A.1 shows the deformation and Von Mises stress for 10 N wall force and 10 N Friction force. Figure A.2 shows the deformation of the rubber lip during a sliding movement across a rigid surface. The aim of this simulation is to approximate the angle of the chamfer on the rubber lip for the lab experiments.

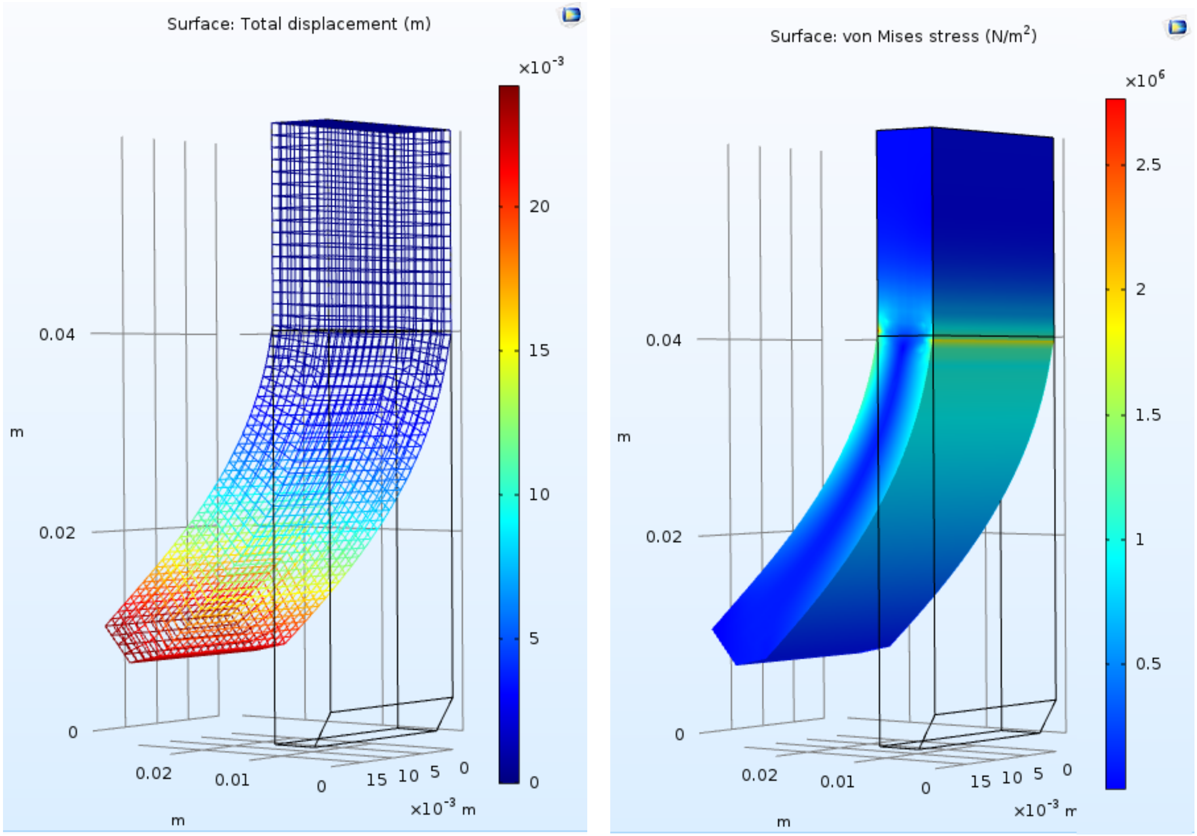

(a) Mesh and deformation plot.

(b) Von Mises stress plot.

Figure A.1: Deformation of a clamped rubber lip with a wall and friction force imposed on it.

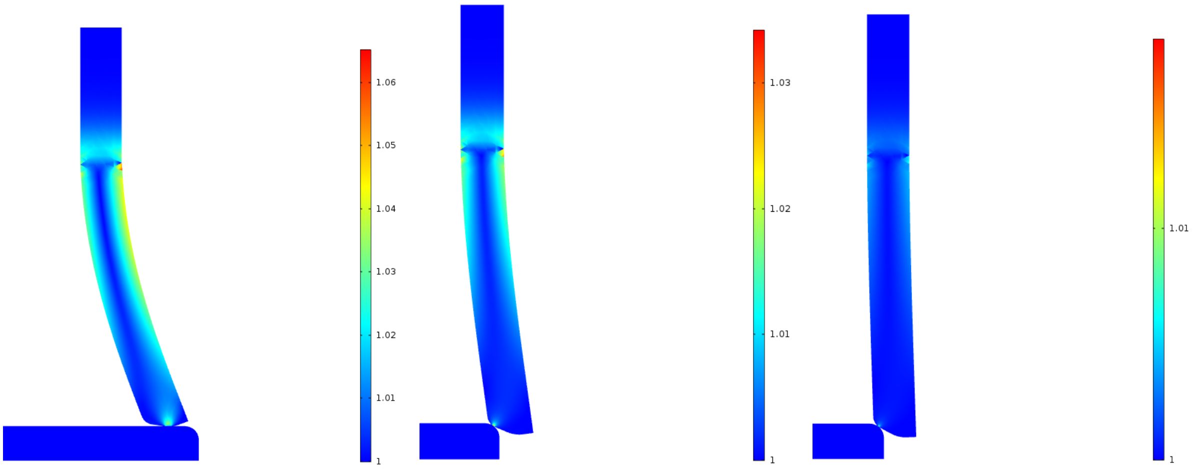

(a) 16 mm sliding.

(b) 4 mm sliding.

(c) 1mm sliding.

Figure A.2: 2D Deformation of a clamped rubber lip sliding across a steel surface.

B

Components in the experimental set-up

B.1. Force measurement

Force transducers are common devices that fulfill the task of force measurements in many applications. Variations in the force on a transducer are registered by the connected amplifier as changes in electrical resistance of the transducer. A transducer is essentially a two-component device consisting of an elastic element and a chain of strain gauges. Strains are introduced in the elastic element by the applied forces; the strain gauges translate the physical strain to electrical resistance. These two components will be discussed in detail to help the design of the force measurement system.

B.1.1. Strain gauges

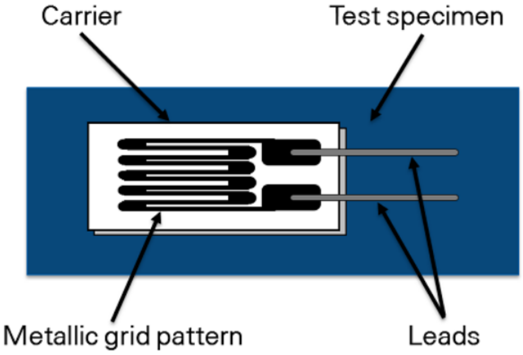

Figure B.1: The elongation of conductive wires in a strain gauge lead to an increase in the electrical resistance.

Strain gauges are essentially conductive wires that form a zigzag pattern on the measurement grid (see Figure B.1). When the grid elongates or shortens as a result of tensile or compressive stresses, the resistance of the strain gauge changes. The relation of this shift in resistance and the difference in strain is defined by the gauge factor:

$$GF = \frac{\Delta R/R}{\Delta L/L} = \frac{\Delta R/R}{\varepsilon} \tag{B.1}$$

In practice, strain gauges rarely involve quantities larger than a few millistrain. Therefore care must be taken to place the gauges on the parts of the elastic element that deform the most. To accurately measure the strains, very small changes in resistance have to be registered. Suppose that an elastic body undergoes 500 microstrain ($\mu\varepsilon$). A strain gauge with a gauge factor of 2 will show a change in resistance of only $2 \cdot (500 \cdot 1e-6) = 0.1\%$. For a 120 Ω gauge this is a change of only 0.12 Ω. To enhance the sensitivity of the system a Wheatstone bridge circuit is applied in the transducers. A general Wheatstone bridge, shown in Figure B.2, is a circuit that involves four resistive arms with an excitation voltage V_{ex}.

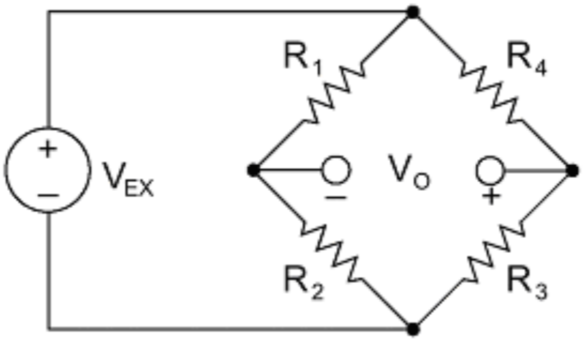

Figure B.2: The general Wheatstone bridge increases the sensitivity of the difference in resistance on any of the four arms [2].

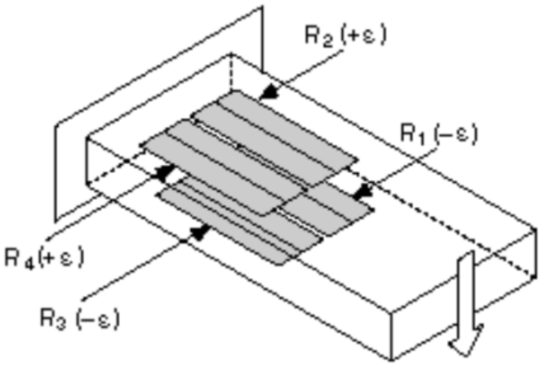

Figure B.3: In a full Wheatstone bridge configurations strains are measured by unbalancing the bridge with opposing pairs.

The output of a Wheatstone bridge is measured between the middle nodes of the circuit and follows from:

$$V_0 = \left(\frac{R_3}{R_3 + R_4} - \frac{R_2}{R_1 + R_2} \right) V_{\text{ex}} \tag{B.2}$$

As shown in this equation the bridge is balanced when the output voltage is zero by means of:

$$\frac{R_1}{R_2} = \frac{R_4}{R_3} \tag{B.3}$$

Any change in resistance in one of the arms will lead to a non-zero output voltage. The voltage meter that registers the small changes in output voltage can handle much smaller measurement ranges due to increased resolution, which will lead to a higher accuracy.

There are three possibilities to implement strain gauges in Wheatstone bridges[2]:

- Quarter bridge: only one of the resistive arms is replaced by an active strain gauge. The other arms in the circuit have fixed resistances.
- Half bridge: two active strain gauges that register opposing strains double the sensitivity of the bridge in comparison with quarter bridges.
- Full bridge: four active strain gauges that register opposing strains lead to high bending strain sensitivity. An example configuration of this bridge is illustrated in Figure B.3.

The full bridge configuration compensates for lead wire resistance and material temperature effects, since the strain pairs undergo the same temperature related strains in the material and keep the bridge balanced. For this reason the full bridge configuration is advised for use in a force measurement system.

B.1.2. Elastic element

The elastic element of a transducer is often shaped as a combination of beams. Typical designs of these elements are shown in figure B.4. The aim, when designing the elastic element, is to keep the geometry as simple as possible. Deformation of the material must remain purely elastic, as the name already states, to prevent strains from becoming permanent. Important properties of the element material include [1]:

- Linearity: the relation between imposed load and strain are ideally perfectly linear.
- Low hysteresis: when stresses decrease, the stress-strain curve should follow the same path as when stresses increase.
- Low creep: after various load cycles the material should behave exactly the same.

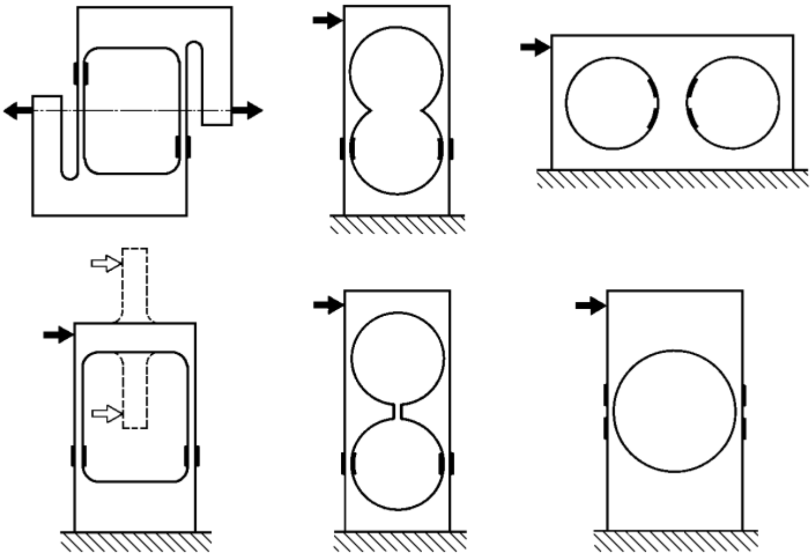

Figure B.4: Several designs of elastic elements for producing force transducers [1].

- High elasticity: Elastic materials can take higher amounts of strain and still revert back to their unstressed original state.

- Low temperature coefficient of Young's modulus: the influence of temperature on the elastic modulus should be minimal.

Spring steel is a very common choice for transducers, since it adopts all of the above mentioned properties. To investigate the relation between the geometry of the transducer and the applied loads, a simple cantilever beam is considered. The shear force that is imposed on the beam leads to a static strain that is related to the moment at any specific location. The relation between the force and the introduced strain is:

$$\varepsilon = \frac{M\frac{1}{2}t}{EI} = \frac{6FL}{Ebt^2} \tag{B.4}$$

When the imposed force F is low, the stiffness of the element can be decreased by increasing the length L of the beam, reducing the width b or the thickness t and - as a last resort - lowering the elastic modulus by choosing another material. The length of the beam is generally restricted by the desired size of the transducer. The width of the beam can be reduced, but this can lead to an extra torsional degree of freedom when the force on the tip of the beam is not proportionally divided over the width. Reduction of the thickness will lead to a quadratic increase in strain. Spring steel is the conventional material choice for transducers and it possesses the most favourable properties for this application. Another material that is commonly used in manufactured transducers is aluminium. The elastic modulus of aluminium is approximately one third of that of spring steel. The fact that it has an higher temperature coefficient of Young's modulus makes it a less popular option than spring steel. Nonetheless, aluminium is suited to decrease the elastic modulus to make the transducer sensitive to smaller forces.

In reality the forces are never perfectly centred and there is always some offset from the desired point of application. The geometry of the transducer should cancel out any parasitic stresses in these situations by remaining rigid in any other degree of freedom (DOF) than the direction that it is designed for. Many studies have been done in the restriction of DOFs in micro- and nano-positioning control systems. Some of these systems use leaf springs and wire components in so-called flexures to assure fully frictionless motion. The same components can be used in the design of an elastic element for the transducer.

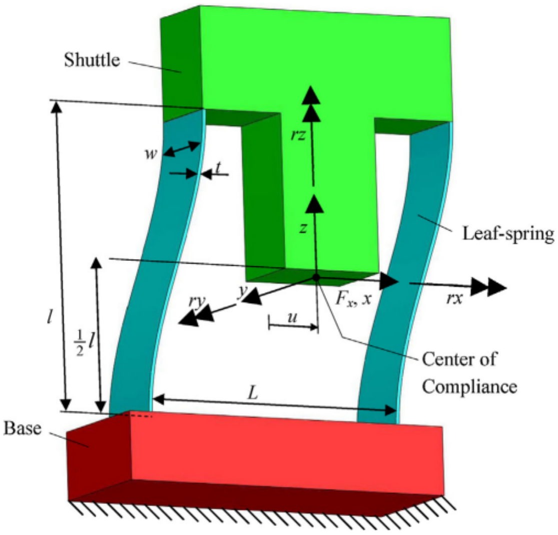

Figure B.5: Parallel leaf spring flexure in a deflected state [6].

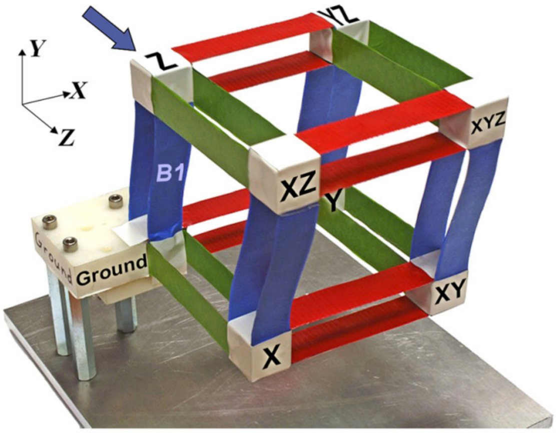

Figure B.6: Flexure construction that decouples movement in the x,y and z direction [5].

Figure B.5 shows a leaf spring construction that restricts the DOFs to a fluent translating motion. A small parasitic translation will be visible when the deformation in the x-axis is large, but for transducer designs deflections of a few millimetres are sufficient. Brouwer *et al.*[6] extensively studied this flexure element and presented analytical equations for the stiffness in three dimensions. The results of these equations were validated with an FEA and showed good agreement. These equations confirm the relatively low translational stiffness of the parallel leaf spring flexure in the x-direction and high stiffness in 5 other DOFs. Any applied strain gauges on these leaf springs would purely register the strains that correspond to forces that act in the x-direction. Other forces and moments that could affect the strain measurement on any arbitrary geometry are now ineffective because of the translational and torsional stiffness. This means that the measurement of force in a specified direction can be fully decoupled from other forces. Applying this to the lubrication experiment would require an extension of the flexure element since two forces are studied: wall and friction force. Awtar *et al.*[5] designed a flexure construction that decouples forces into an x,y and z-direction by connecting twelve parallel leaf springs with each other. Shown in Figure B.6 is the resulting mechanism on which a force acts in the z-direction. The DOFs of each joint are depicted by the label that is written on them. There is only one joint that can move in three translational directions. For the lubrication experiment two DOFs suffice and this design can be reduced to a construction of four parallel leaf spring flexures.

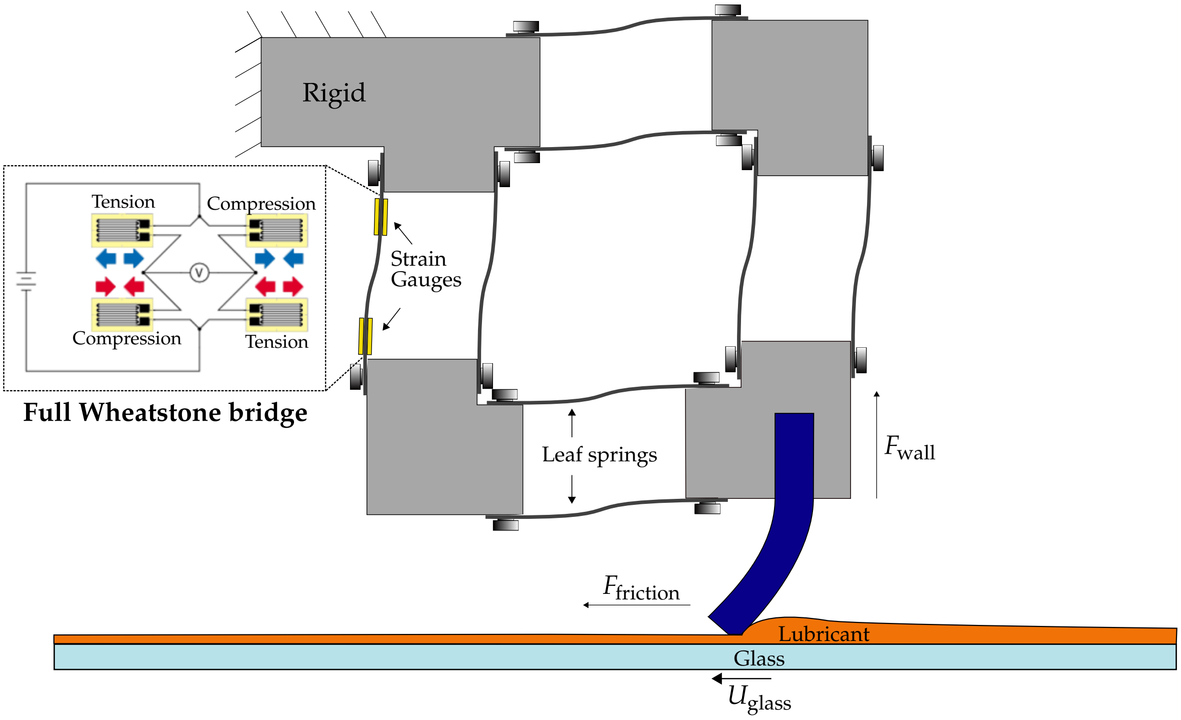

Figure B.7: The transducer designed to measure the wall and friction force of the lubricated rubber sample.

Subsequently, the strain gauges can be attached to the leaf springs in a full Wheatstone bridge configuration: two on both sides of the leaf spring. As the moments and strains are highest at the junctions, these are the locations where the gauges should be attached. Note that some offset will be held from the junction since nonlinear material behaviour is common there.

Wall forces that act on the designed transducer in Figure B.7 will now induce a strain in all four leaf springs that are deformed by the force. This strain is measured by the strain gauges and converted to a force if the transducer is successfully loop-tested. This loop test is done by using scales to determine the force that corresponds to a certain strain. The desired measurement range of the force can now be determined by using Equation B.4 and the designed transducer will give fully decoupled forces that act on the XY joint.

B.2. Optical system

To capture an image of the thin film layer between the rubber sample and the glass (see Figure B.7), care should be taken in selecting the appropriate components of the camera system. To summarize, the requirements are:

- High magnification to frame only the lubrication layer between the rubber sample and the glass plate.
- High resolution to accurately measure the thickness of the layer. The pixels in the image will serve as a ruler.
- High frame rate to capture enough frames when performing experiments with high sliding velocities.
- Sufficient working distance of the microscope lens to prevent moving parts from bumping the lens.
- Stable mount, to dampen out possible vibrations during the experiments.

The first three requirements are usually a trade-off, because the required data transfer rate rises with an increase of one of them.

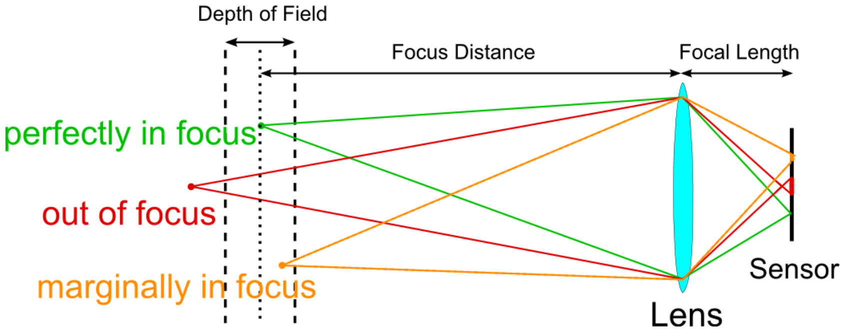

Figure B.8: Optical pathways of a camera system [20].

Figure B.8 shows a simple camera system consisting of a sensor and a lens. While this figure illustrates a system with only one lens, it could also be an objective consisting of multiple lenses. The focus distance is the one specific distance at which the lens focuses on an image. Whenever a point is farther away from the lens than the focus distance, the light rays do not intersect precisely at the sensor plane anymore, but somewhere after or in front of the sensor. This produces a blurred circle on the sensor instead of sharp details. The depth of field of the sensor determines the spatial deviation from the focus distance at which the image on the sensor is still acceptable. In normal photography this depth could be easily a quarter of a meter, but in microscopy the depth of field often ranges from 0.1 to 100 microns. The primary objective and the sensor are of particular importance in a microscope system and the important features of these components will be explained in the next subsections.

B.2.1. The sensor

A sensor is a device that receives a signal and responds to it with an electric signal. The sensors that are used in optic imaging consist of a grid of photoelectric cells. These cells are called pixels and emit an electric signal proportional to the amount of light that it receives. The sensitivity to light of a camera system is therefore largely defined by the quality of the sensor. Figure B.9 depicts the aspects of sensor performance in a concept drawing of a pixel. In this illustration photons are converted to grey scale quantities, but the same concept applies for colour sensors. The following properties all have an impact on the sensor sensitivity:

- Pixel size
- Quantum efficiency (QE)
- Saturation capacity
- Temporal dark noise
- Dynamic range

The amount of light received by a pixel on an image depends on the light intensity, exposure time and pixel size. The latter has a non-linear effect on the light collection ability of the pixel, since that quantity needs to be squared to acquire the effective light receiving area. The fraction of the photons that is effectively converted to electrons during digitalisation of the light is called the quantum efficiency (QE) [3]. The sensor in Figure B.9 has a QE of 50%, because 3 of the 6 photons are converted to electrons. The QE typically ranges from 30% for low-end sensors to 80% for more advanced sensors [4]. A higher QE means that there is less light required to resolve an image on the sensor. After conversion of the photons, the electrons are stored in the well of the pixel. The maximum amount of electrons that can be stored in the well is called the saturation capacity. When the light collection is completed by the pixel, the signal is measured. The output signal of a pixel as a function of the light density is given by:

$$\text{signal} = \text{light density} \cdot (\text{pixel size})^2 \cdot \text{quantum efficiency}. \tag{B.5}$$

Any errors in this measurement are denoted as temporal dark noise. All of the previously explained properties directly influence the dynamic range of a sensor. While the other features in the list are not

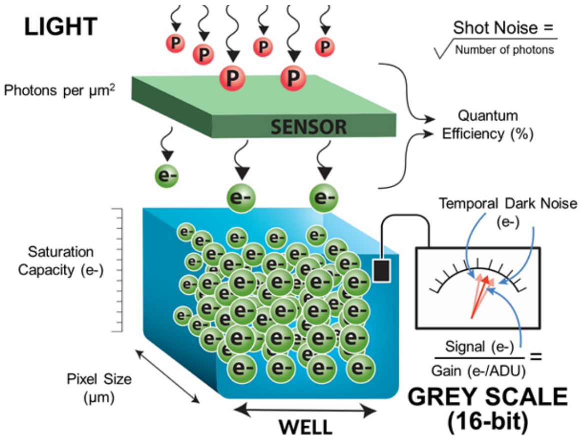

Figure B.9: A pixel depicted as a well with several important properties that define its sensitivity [3].

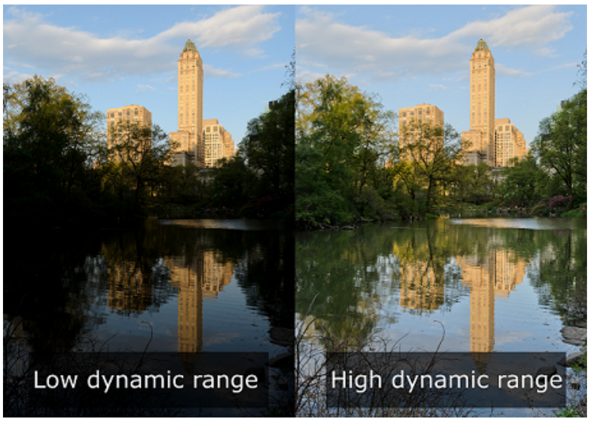

Figure B.10: Comparison between an image shot with sensors that have a relatively low and high dynamic range [26]

always mentioned in the camera specifications, the dynamic range often is. This property considers the ratio of the signal versus the noise and equals the capacity of the sensor to differentiate between light intensities. Figure B.10 shows the difference between an image taken with a sensor that possesses a high dynamic range and one with a low dynamic range. It is clear that the right image contains much smaller steps in the contrast variation (light to dark) than the left image, which reveals more details. A sensor that will be used for experimental work should be able to capture as many details as possible in the images and thus should possess a high dynamic range.

An image is discretized by a grid of pixels in the sensor, where the amount is typically denoted by megapixels. A 36 megapixel camera can resolve more details in an image than a 12 megapixel camera, but the downside is that the pixels will be smaller for the same sensor size. As explained, smaller pixels lead to a decrease in signal and therefore dynamic range. This outlines the trade-off in selecting the number of megapixels for an application: too many will restrict the dynamic range due to the decreasing pixel size and too few reduces the amount of details that can be resolved.

The camera that was selected for the experimental set-up has a 36 megapixel full frame sensor. This camera was selected mainly for its versatility and high quality imaging capabilities.

B.2.2. Objectives

Microscope objectives have three main criteria that are of importance during the selection:

- Magnification factor
- Working distance
- Numerical aperture

The magnification factor equals the ratio between the dimensions of the sensor and those of the image. The literature states that the lubrication layer between the sealing disc of a pig and the pipeline wall range approximately between 1 and 50 microns [9, 25]. Describing 1 micron with 2 pixels could already give a good description of the film thickness in an image. The working distance is the distance between the absolute front edge of the objective and the plane where the image is sharp. Longer working distances give more flexibility to observe phenomena through the glass and fluids, but lead to lower numerical apertures (NA). The numerical aperture of a lens is given by:

$$\mathrm{NA} = I_r \cdot \sin(\alpha). \tag{B.6}$$

Here I_r is the refractive index of the medium the light passes through and α is the maximum half-angle of the cone of light that can enter or exit the lens. Figure B.11 illustrates how the numerical aperture of a lens influences its image resolving capabilities. It is a measure for the angle at which light rays are captured in the main objective and it relates to an important feature of the objective: optical resolution.

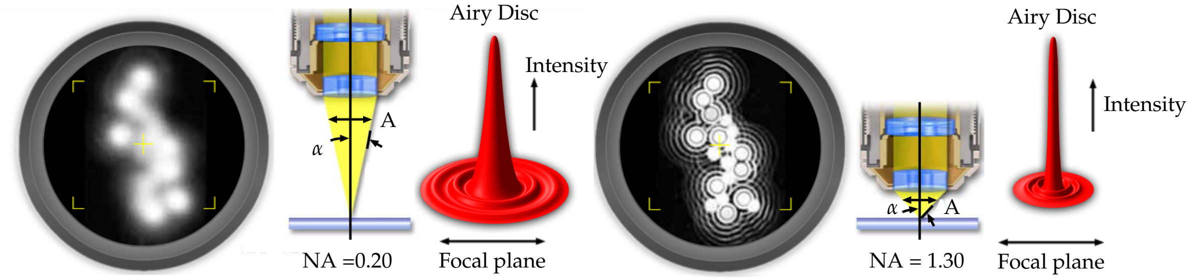

Figure B.11: A lens with a low numerical aperture could lead to an unresolved image due to wide Airy discs, while a lens with a high numerical aperture can resolve more details due to thin Airy discs [7].

The term resolution in the context of cameras often refers to the resolution of the sensor, but lenses and objectives also have an optical resolution. To optimize the information content in an image both resolutions should be closely matched in the selection of an objective. One of the limiting factors of the optical resolution is the wave length of visible light, used to produce an image [7]. The limits of spatial resolution are dictated by the diffraction of light through the optical system. Given a perfect objective lens and an infinitely small point of light residing in the focus plane, the dot formed on the lens is not infinitely small anymore, but a diffracted image with a finite spread[17]. The image that is produced is shown in figure B.11 and called an Airy diffraction disc. The radius from the peak in the centre and the first minimum determine the resolved details in an image, which is predicted by:

$$r = 0.61 \frac{\lambda}{\mathrm{NA}} \tag{B.7}$$

Here λ is the wave length of the light that shines through the objective and NA is the numerical aperture of the objective. This same distance is also called the optical Rayleigh resolution. Rayleigh stated this is the separation distance at which two point sources are still considered to produce a resolved image through a microscope [7]. When the distance between the point sources becomes smaller than this radius, the image is observed as a cluster of vague dots that are clumped together (see figure B.11). As shown by Equation B.7, the numerical aperture is the controllable parameter that can make the difference between a resolved sharp image and a blurry frame. The key element in selecting the right objective is the matching of the image pixel size with the optical resolution. The image pixel size is the physical pixel size multiplied by the magnification factor. For example, when the selected sensor has pixels with a physical size of 5x5 micronos squared and the magnification factor is 20, the image pixel size will be 250 nm. Considering that the image will be observed with visible light, the used wave length is averaged by 550 nm. A numerical aperture of 0.8 will then define the optical resolution as 419 nm, which is a factor 1.67 larger than the digital resolution and some details in the image will not be optically resolved. The system is diffraction limited in this case and the effective number of pixels depicted by the camera is actually lower.

The objective selected for the experimental set-up has a magnification of 20, a working distance of 20.5 mm and a numerical aperture of 0.35. This produces an image of 0.79 by 1.5 mm^2 on the sensor selected in subsection B.2.1. The numerical aperture restricts the optical resolution to a lower value than the digital resolution. This is a result of the relatively small pixel size on the sensor and the long working distance, which are needed to prevent collisions with the moving parts of the set-up.

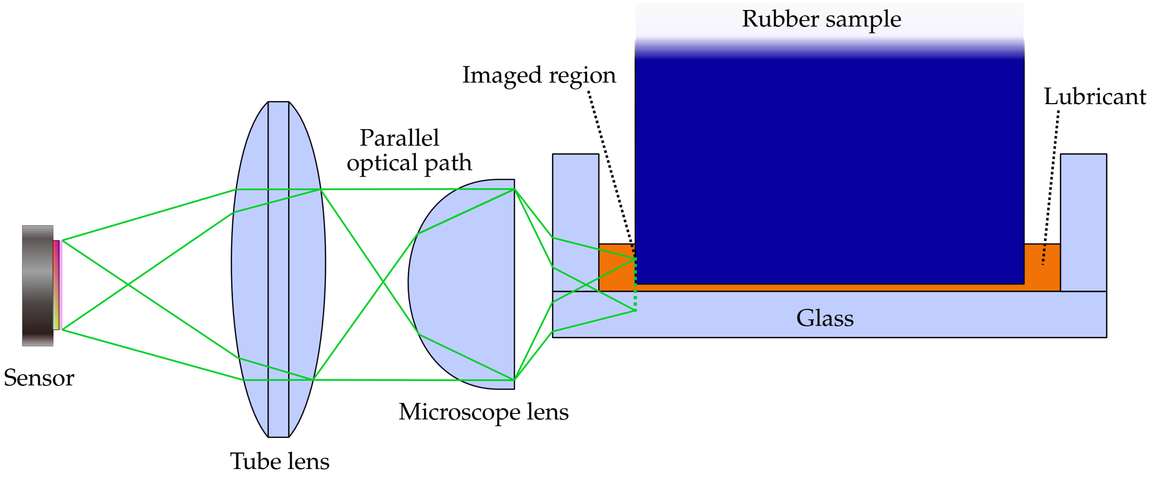
Rubber sample
Imaged region
Lubricant
Parallel optical path
Glass
Sensor
Microscope lens
Tube lens

Figure B.12: The optical set-up will use an infinity corrected microscope system to frame the lubrication layer between the rubber sample and the glass plate.

The final optical set-up that will be used in the lab is illustrated in Figure B.12. A so-called tube lens was added between the main microscope lens and the sensor. The focal length of the tube lens can be adjusted to ensure full coverage of the image on the sensor. This is called an infinity corrected system, which has the advantage that extra lens components can be added in the parallel optical path between the microscope lens and the tube lens without altering the alignment.

C

Additional results from the pig Tribometer

C.1. Friction force

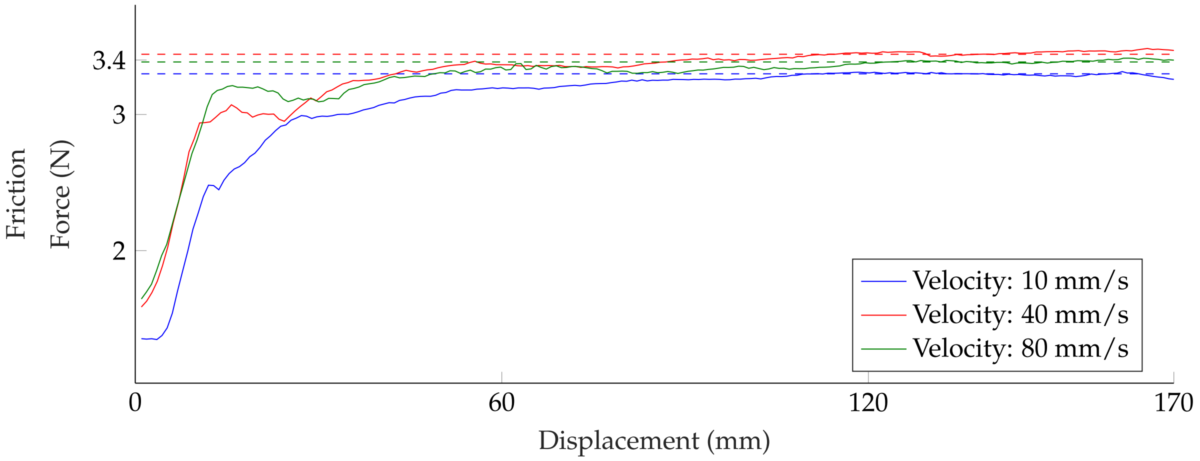

Figure C.1: Castor oil.

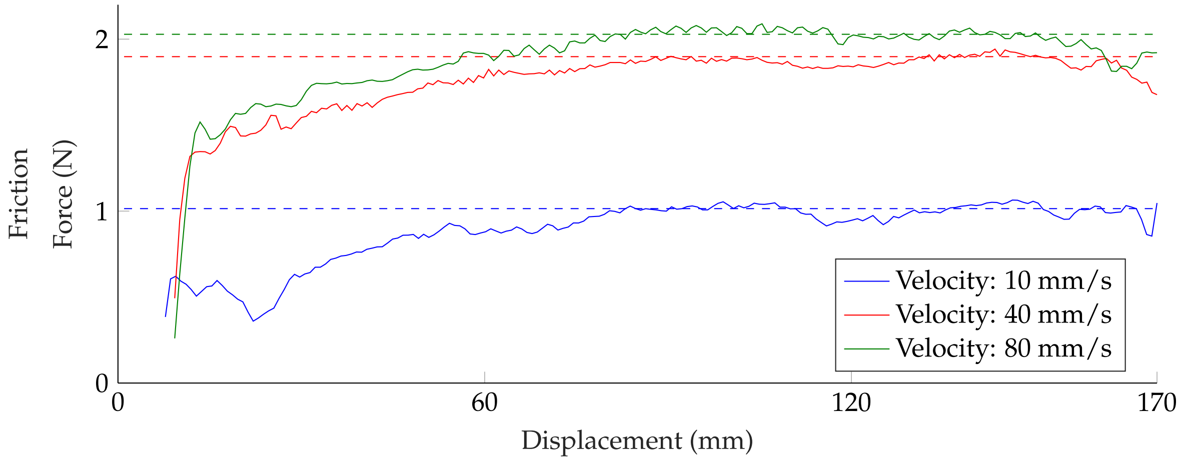

Figure C.2: Castor oil.

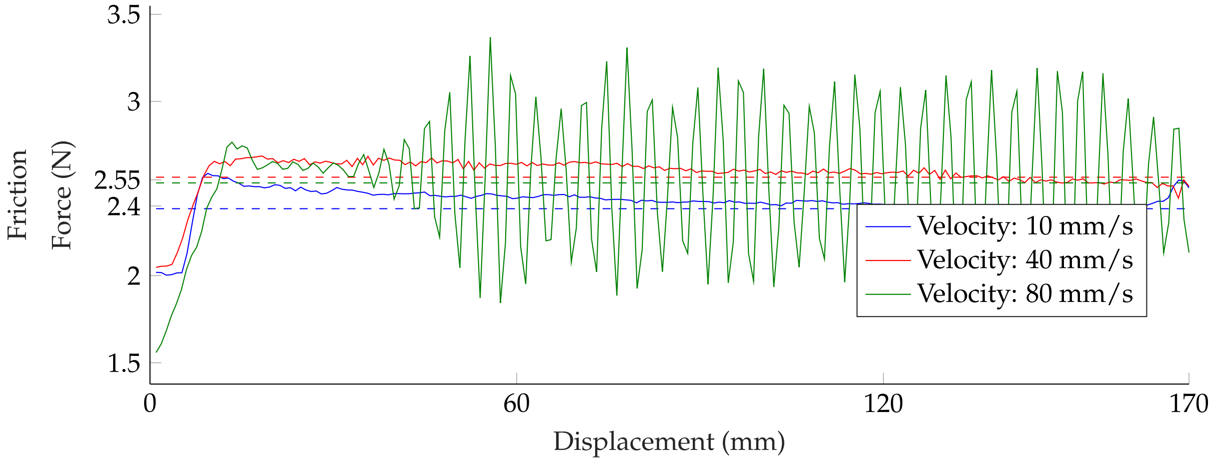

Figure C.3: Castor oil.

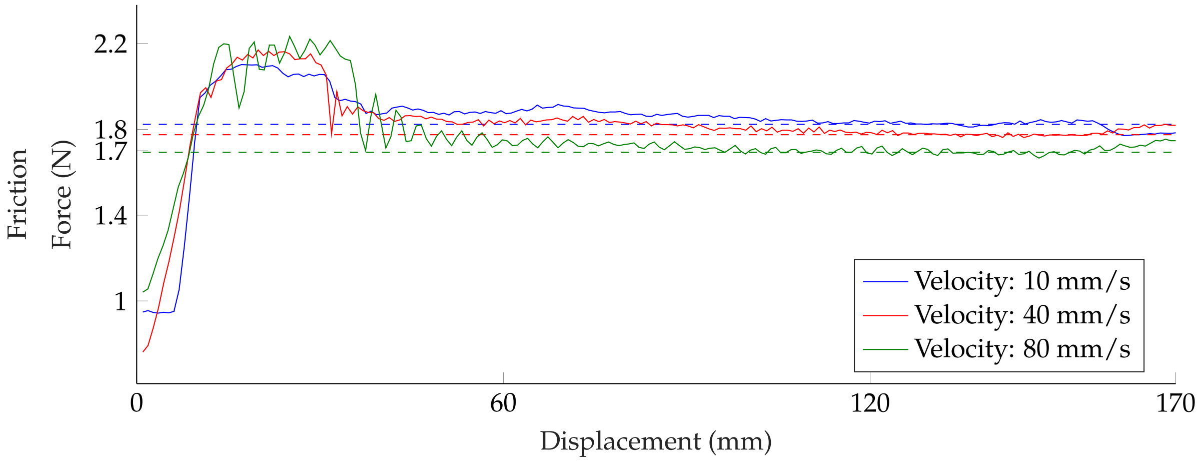

Figure C.4: Castor oil.

C.2. Wall force

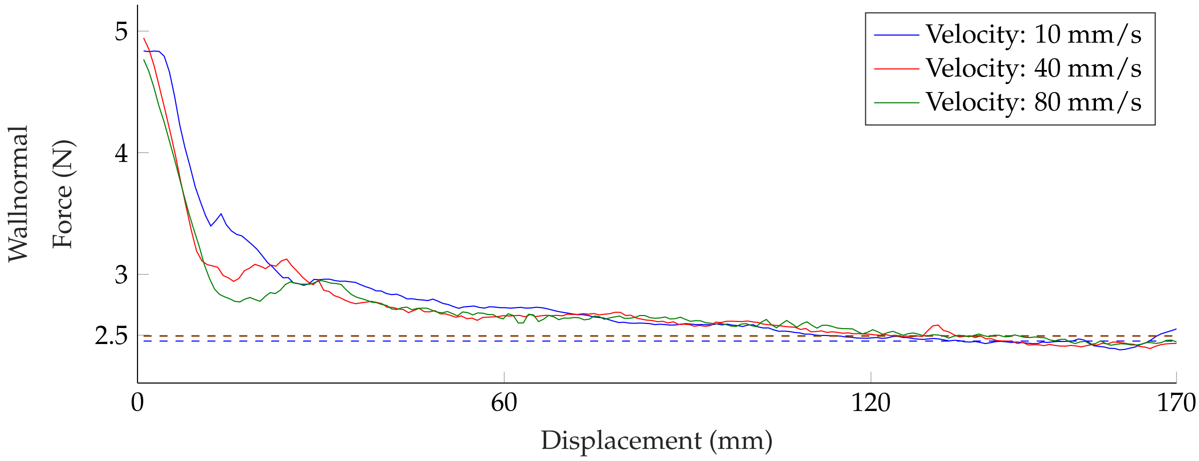

Figure C.5: Castor oil.

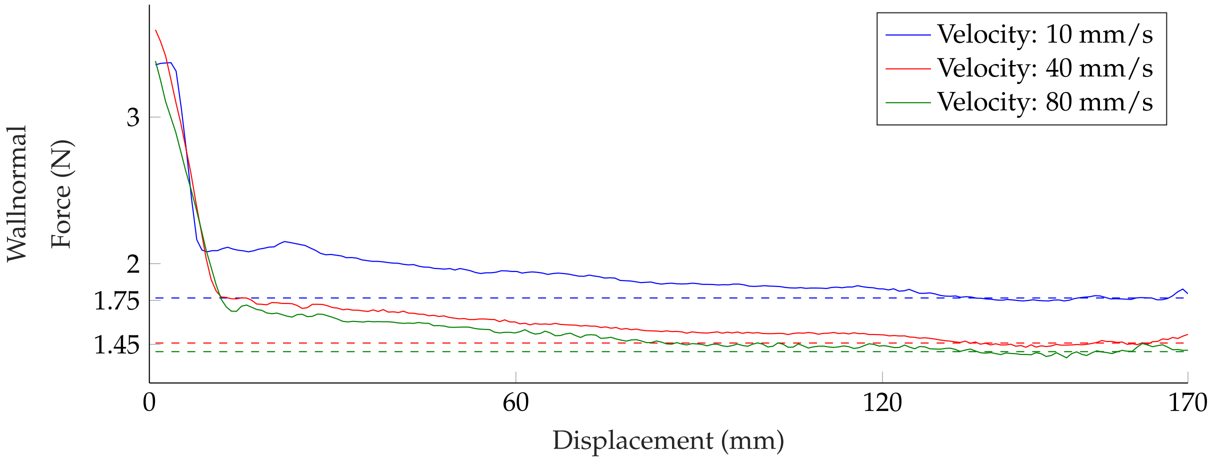

Figure C.6: Castor oil.

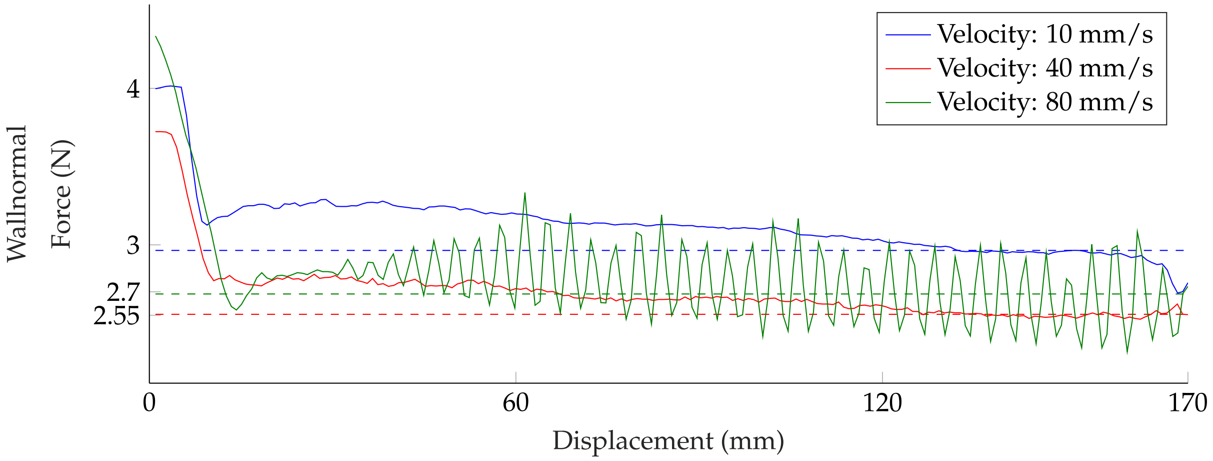

Figure C.7: Castor oil.

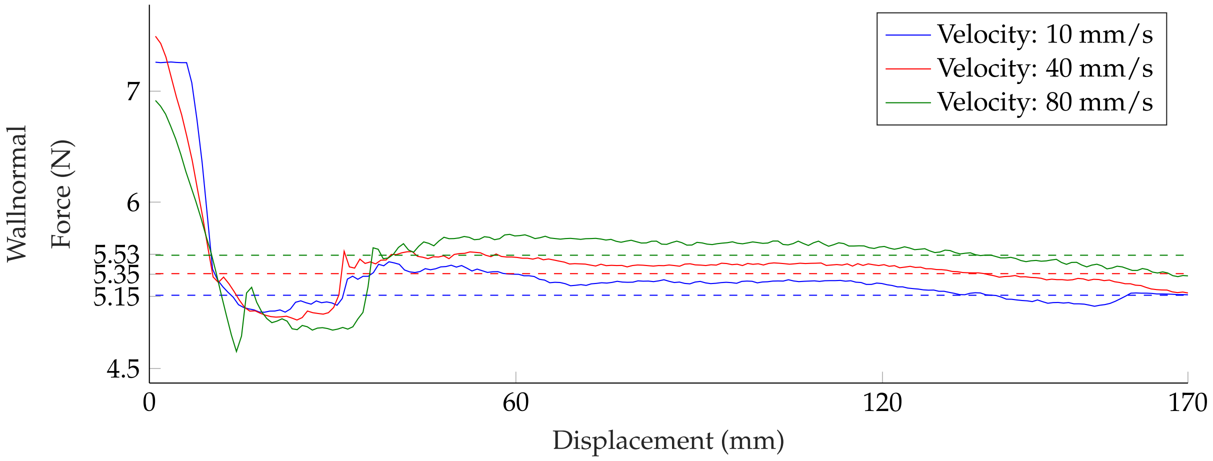

Figure C.8: Castor oil.

C.3. Friction coefficient

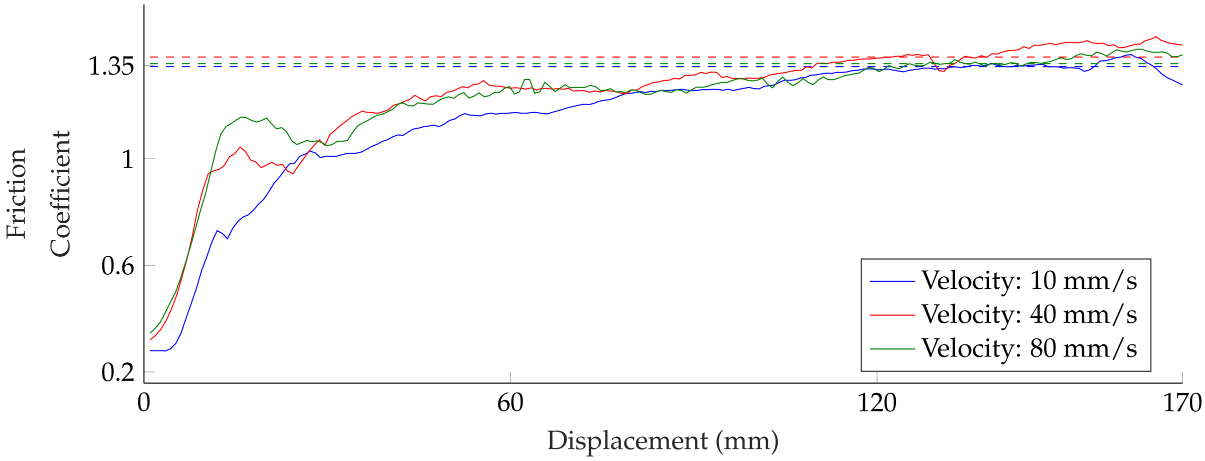

Figure C.9: Comparison of the friction coefficient trajectory as function of sliding distance for dry friction with a 6mm thick rubber lip.

Figure C.9 shows a comparison of the trajectories of the friction coefficient for different sliding velocities of dry friction. This is a benchmark for testing the precision of the experimental facility, because dry friction should be independent of the sliding velocity. These trajectories confirm this since they all end up at a similar friction coefficient.

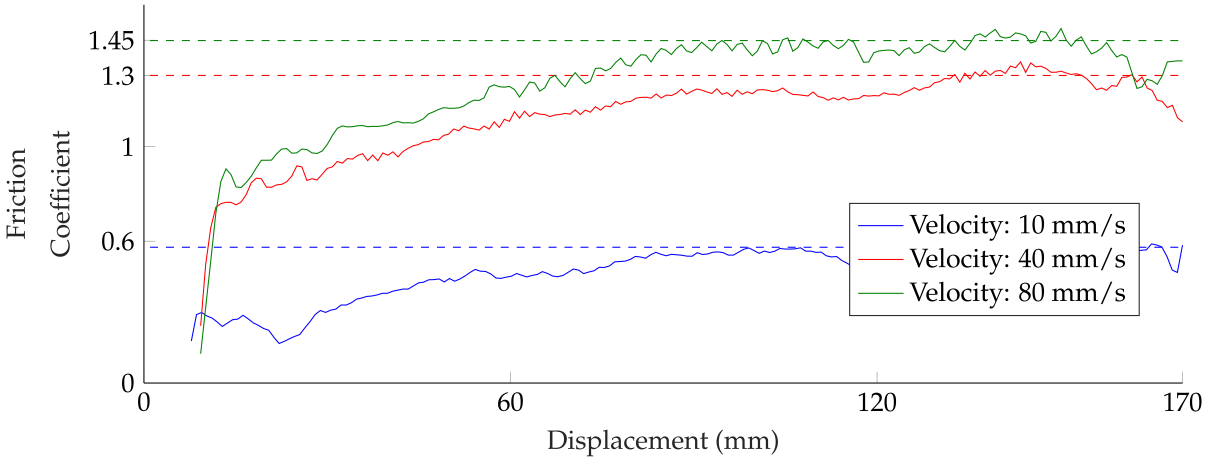

Figure C.10: Castor oil.

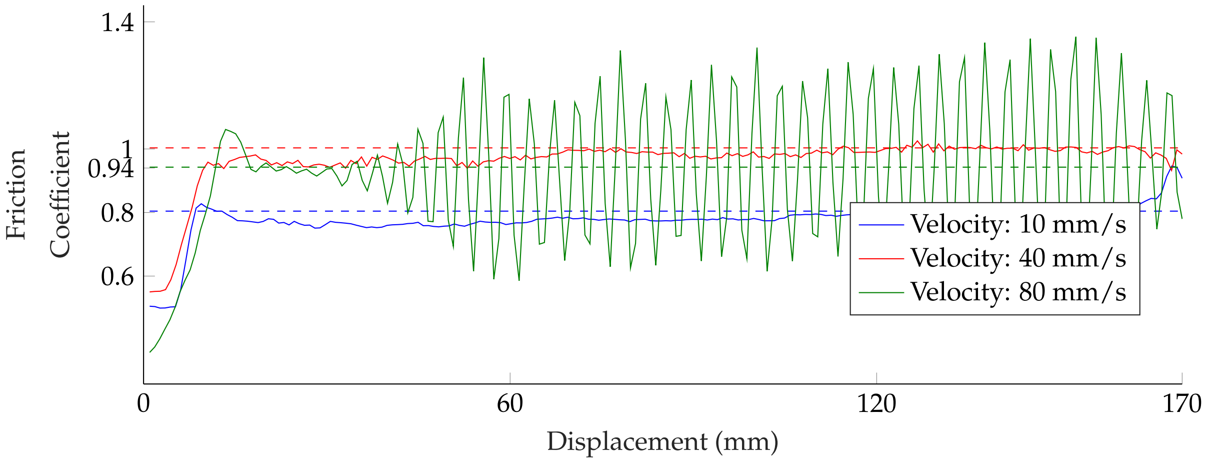

Figure C.11: Castor oil.